Department of Physics and Astronomy

Heidelberg University

Master Thesis in Physics
submitted by

Matthias Heinrich

born in Leipzig (Germany)

2026

Electron Paramagnetic Resonance and Magnetisation Studies on $3d$-, $3d$-$4f$- and Bi-based Metal-Organic Molecular Complexes

This Master thesis has been carried out by Matthias Heinrich
at the
Kirchhoff Insitute for Physics
under the supervision of

Prof. Dr. Rüdiger Klingeler

Electron Paramagnetic Resonance and Magnetisation Studies on 3*d*-, 3*d*-4*f*- and Bi-based Metal-Organic Molecular Complexes

This thesis presents a systematic investigation of the magnetic properties of several metal–organic molecular complexes by means of high-frequency/high-field electron paramagnetic resonance spectroscopy and magnetisation measurements. The members of a series of $Co^{II}Co^{III}_4$ complexes show single-ion magnetic behaviour due to the central paramagnetic Co^{II} ion in a distorted tetrahedral coordination environment. Studies on one representative complex reveal a magnetic easy-plane anisotropy of $D = 580(150)$ GHz. The experimental results suggest that deviations of the local ligand field from the ideal tetragonal symmetry, achieved through varying the organic ligands, result in enhanced magnetic anisotropy. In $Cu^{II}_5Ln^{III}$ (Ln = Y, Gd, Dy) 15-MC-5 metallacrowns, strong antiferromagnetic exchange coupling $J_{\text{Cu-Cu}} = -148(10)$ K between the nearest-neighbour Cu^{II} magnetic moments within the pentagonal ring structure and weak ferromagnetic Cu-Ln interaction $J_{\text{Cu-Ln}}$ is determined. The observed chemical trend $J_{\text{Cu-Gd}} > J_{\text{Cu-Dy}}$ indicates that $3d \rightarrow 5d$ charge-transfer is the dominant $3d$-$4f$ exchange process. For an all-metal-σ-aromatic Bi_4 ring, the purely diamagnetic response is investigated, showing no evidence for diamagnetic exaltation.

Elektronenspinresonanz- und Magnetisierungsmessungen an 3*d*-, 3*d*-4*f*- und Bi-basierten metallorganischen Molekülkomplexen

Diese vorliegende Arbeit präsentiert eine systematische Untersuchung der magnetischen Eigenschaften verschiedener metallorganischer Molekülkomplexe mittels hochfrequenter Hochfeld-Elektronenspinresonanz-Spektroskopie sowie Magnetisierungsmessungen. Die Vertreter einer Reihe von $Co^{II}Co^{III}_4$-Komplexen zeigen ein magnetisches Einzelionen Verhalten, das auf das zentrale paramagnetische Co^{II}-Ion in einer verzerrten tetraedrischen Koordinationsumgebung zurückzuführen ist. Untersuchungen an einem repräsentativen Komplex zeigen eine magnetisch planare Anisotropie von $D = 580(150)$ GHz. Die experimentellen Ergebnisse deuten darauf hin, dass Abweichungen des lokalen Ligandenfeldes von der idealen tetragonalen Symmetrie, die durch Variation der organischen Liganden erreicht werden, zu einer verstärkten magnetischen Anisotropie führen. In $Cu^{II}_5Ln^{III}$ (Ln = Y, Gd, Dy) 15-MC-5 Metallacrowns zeigt sich eine starke antiferromagnetische Austauschwechselwirkung $J_{\text{Cu-Cu}} = -148(10)$ K zwischen den magnetischen Momenten benachbarter Cu^{II}-Ionen innerhalb der pentagonalen Ringstruktur sowie eine schwache ferromagnetische Cu–Ln Kopplung $J_{\text{Cu-Ln}}$. Der beobachtete chemische Trend $J_{\text{Cu-Gd}} > J_{\text{Cu-Dy}}$ deutet darauf hin, dass der $3d$-$4f$ Ladungstransfer den dominierenden $3d$–$4f$ Austauschmechanismus darstellt. Für einen rein metallischen σ-aromatischen Bi_4-Ring konnte aus dem diamagnetischen Verhalten keine Evidenz für eine diamagnetische Verstärkung festgestellt werden.

Contents

1 Introduction **1**

2 Theoretical Background **3**
2.1 The Free Ion . . . 3
2.2 Ion in a Magnetic Field . . . 3
2.3 Spin-Orbit Coupling . . . 4
2.4 The Crystal Field . . . 6
2.5 Spin-Spin Interaction . . . 9
2.6 Electron Paramagnetic Resonance . . . 9
2.7 Magnetic Relaxation . . . 11
2.7.1 AC Susceptibility . . . 11
2.7.2 Magnetic Relaxation Processes . . . 12

3 Experimental Methods **15**
3.1 Magnetometry . . . 15
3.1.1 Experimental Setup (MPMS3) . . . 15
3.1.2 Sample Preparation . . . 16
3.1.3 Background Correction . . . 17
3.1.4 Sample Shape Effects . . . 19
3.1.5 Influence of Sample Holders on AC Susceptibility . . . 19
3.1.6 Remanent Magnetic Field . . . 21
3.2 High-frequency/High-field Electron Paramagnetic Resonance Spectroscopy . . . 23
3.2.1 Experimental Setup . . . 23
3.2.2 Sample Preparation . . . 24
3.2.3 Data Processing . . . 25
3.2.4 Setup Dependent Impurity Resonance . . . 25

4 $Co^{II}Co^{III}_4$ complexes **29**
4.1 Analysis of complex **(1)** . . . 29
4.1.1 Molecular Structure . . . 29
4.1.2 Static Magnetisation and Susceptibility . . . 30
4.1.3 HF-EPR Studies . . . 32
4.1.4 Dynamic Susceptibility . . . 35
4.2 Analysis of complexes **(2)** - **(5)** . . . 38
4.2.1 Static Magnetisation and Susceptibility . . . 39
4.2.2 Dynamic Susceptibility . . . 42
4.3 Comparison between **(1)** - **(5)** and Discussion . . . 44

5 $Cu^{II}_5Ln^{III}$ Metallacrowns **45**
5.1 Molecular Structure . . . 45
5.2 Magnetisation Studies . . . 45

5.3 HF-EPR Studies 49
5.4 Discussion 56

6 All-Metal-Aromaticity: Bi_4 Ring **57**
6.1 Molecular Structure 57
6.2 Magnetisation Studies 58
6.3 Comparison and Conclusion 60

7 Summary and Conclusion **63**

Appendix **65**

Bibliography **77**

1 Introduction

Magnetism plays a fundamental role in our everyday life. Magnetic materials are used in electric motors, data storage devices, sensors, and spin-based electronics. In many of these applications, the bulk properties of the magnetic materials are relevant [1]. However, further miniaturisation requires a shift toward systems in which magnetic functionality can be controlled at the molecular scale. In this context, molecular magnetism has evolved into a highly interdisciplinary field, spanning coordination chemistry, spectroscopy, and solid-state physics, with focus on the development and investigation of discrete magnetic units with tunable properties [2].

A central aspect in molecular magnetism is magnetic anisotropy, which determines the preferred orientation of magnetic moments. Molecular spin systems with pronounced anisotropy can exhibit slow magnetic relaxation due to an effective energy barrier, first observed in the Mn_{12}ac cluster by R. Sessoli and D. Gatteschi [3], which marked the beginning of the class of materials known as single-molecule magnets (SMMs). It has been found that a high effective energy barrier requires a ground state with a large spin and strong magnetic anisotropy [4]. The ability of a single molecule to retain its magnetisation over a long timescale in the absence of an external magnetic field makes it useful for high-density data storage and quantum technologies [5]. SMMs also find applications in medicine, for example as contrast agents in magnetic resonance imaging (MRI) [6, 7].

A dominant factor influencing the magnetic single-ion anisotropy is the electrostatic crystal field [8]. To study how different distortions of the coordination environment of an magnetic ion affect the magnetic single-ion anisotropy and the slow magnetic relaxation, a series of five $Co^{II}Co^{III}_4$ complexes was investigated. These complexes contain different para-substituted benzoic acid ligands, which induce varying degrees of structural distortion in the tetrahedral coordination environment of the central paramagnetic Co^{II} ion.

In the recent decades, a lot of work has been done to improve and understand the magnetic behaviour of SMMs. Early studies focused on increasing the effective energy barrier for magnetisation reversal by increasing the total spin of coordination clusters. This was achieved by including multiple $3d$ transition metal ions that coupled ferromagnetically [9, 10]. However, since the total anisotropy decreases as the number of metal centers increases [11, 12], attention has shifted to $4f$-based complexes, which exhibit magnetic single-ion anisotropy due to strong spin–orbit coupling of the $4f$-orbitals and pronounced crystal field effects [13, 14]. In $4f$-based complexes, quantum tunnelling of the magnetisation (QTM) through the energy barrier leads to fast magnetic relaxation [15, 16], and the weak magnetic exchange interaction between the $4f$ ions limit the benefit of multi magnetic centers arrangements. This motivated the development of combined $3d$–$4f$ systems, which suppress QTM by combining the strong magnetic exchange interactions of $3d$-metal centers with the pronounced spin-orbit coupling and intrinsic magnetic single-ion

anisotropy of $4f$-ions [13]. In this context, three $Cu_5^{II}Ln^{III}$ 15-MC-5 (Ln = Y, Gd, Dy) metallacrown complexes were studied to analyse how the choice of the lanthanide ion affects the magnetic exchange interactions and total anisotropy.

In this thesis, high-frequency/high-field electron paramagnetic resonance spectroscopy (HF-EPR) as well as static and dynamic magnetisation measurements were performed to study the magnetic properties of various metal–organic molecular complexes. First, a brief overview of the theoretical background and experimental details of the used measurement methods is provided. This is followed by the investigation of the series of five $Co^{II}Co_4^{III}$ complexes and the studies on three $Cu_5^{II}Ln^{III}$ 15-MC-5 metallacrowns. An additional project addresses the postulated property of aromatic molecules to exhibit enhanced diamagnetic susceptibility due to field-induced ring currents. In this context, an all-metal-σ-aromatic Bi_4 ring was investigated to evaluate the presence of diamagnetic exaltation. The thesis concludes with a summary and a final conclusion of the main findings.

2 Theoretical Background

This chapter provides an introduction to the physical properties of ions in solid-state materials, including their magnetic behaviour and the origin of magnetic anisotropy. Furthermore, the fundamentals of electron paramagnetic resonance spectroscopy and magnetic relaxation are discussed. The description of the theoretical background is based on Refs. [2, 8, 17–19], which contain more detailed descriptions. Unless stated otherwise, the following information has been taken from there.

2.1 The Free Ion

Let us first consider a free ion with N electrons. In the Hartree-Fock approximation the single-particle wavefunction of each electron is of the form

$$\psi_i(\boldsymbol{r}_i)_{n,l,m_l,s,m_s} = R_{nl}(r_i)Y_l^{m_l}(\phi_i,\theta_i)\chi(m_s) \tag{2.1}$$

with the radial part $R_{nl}(r_i)$, an angular part described by the spherical harmonics $Y_l^{m_l}(\phi_i,\theta_i)$, and a spin function $\chi(m_s)$. A state of an electron in the ion can therefore be characterised by a set of quantum numbers, with $n = 1, 2, ...$ denoting the principal quantum number, l $(0 \leq l \leq n-1)$ the orbital quantum number and m_l $(-l \leq m_l \leq l)$ the magnetic quantum number. The spin is characterised by the spin quantum number $s = 1/2$ with $m_s = \pm 1/2$.

To determine the complete electronic configuration of the ion, the single-particle states are filled with electrons, starting from the lowest energy levels, while respecting the Pauli exclusion principle. Degenerate states are populated according to Hund's first two rules: The total spin $S = \sum_i^N s_i$ is maximised first, followed by the maximisation the total orbital angular momentum $L = \sum_i^N l_i$.

2.2 Ion in a Magnetic Field

When the ion is subjected to an external magnetic field $\boldsymbol{B}$, the degeneracy of the states with respect to m_l and m_s is lifted. This phenomenon is known as the Zeeman effect. Assuming a homogeneous magnetic field, one obtains the Hamiltonian

$$\hat{\mathcal{H}} = \hat{\mathcal{H}}_{\text{free}} + \mu_{\text{B}}\boldsymbol{B}\left(\hat{\boldsymbol{L}} + g_s\hat{\boldsymbol{S}}\right) + \frac{e^2}{8m_e}\sum_i^N(\boldsymbol{B}\times\hat{\boldsymbol{r}}_i)^2, \tag{2.2}$$

where $\hat{\mathcal{H}}_{\text{free}}$ denotes the Hamiltonian for a free ion. μ_{B} is the Bohr magneton, $g_s \approx 2$ is the electron g-factor, e is the elementary charge, m_e is the electron mass and $\hat{\boldsymbol{r}}_i$ the position operator of the i^{th} electron, respectively. The second term is known as the paramagnetic or Zeeman term, and it only involves electrons in partially filled shells. The third term represents the ion's diamagnetic response. Although all electrons

contribute to diamagnetism, this contribution is typically much smaller than that of the paramagnetic term.

2.3 Spin-Orbit Coupling

Even in the absence of an external magnetic field, the spin experiences an internal magnetic field. In the reference frame of the electron, the nucleus orbits the electron, generating a magnetic field $\boldsymbol{B}_l$ that interacts with the spin magnetic moment $\boldsymbol{\mu_s}$. The resulting interaction Hamiltonian can be written as

$$\hat{\mathcal{H}}_{\mathrm{SOC}} = -\hat{\boldsymbol{\mu}}_s \cdot \hat{\boldsymbol{B}}_l = \lambda \hat{\boldsymbol{s}} \cdot \hat{\boldsymbol{l}}, \tag{2.3}$$

where λ is the spin-orbit coupling parameter. Since $\hat{\mathcal{H}}_{\mathrm{SOC}}$ does not commute with $\hat{l}_z$ and $\hat{s}_z$, a direct consequence of spin-orbit coupling is that the projections of the orbital and spin angular momenta onto the z-axis are not conserved separately. Therefore m_l and m_s are no longer good quantum numbers. Instead, only the total angular momentum $\hat{\boldsymbol{j}} = \hat{\boldsymbol{l}} + \hat{\boldsymbol{s}}$ and its z-component $\hat{j}_z$ remain conserved. With the corresponding quantum numbers j and m_j, we again obtain a set of good quantum numbers for the system.

In multi-electron systems, the coupling of individual angular momenta depends on the relative strengths of the spin-orbit interaction and the Coulomb interaction between electrons. Two distinct coupling schemes are commonly distinguished, each representing a limiting case.

For heavy elements with high atomic number Z, the Coulomb interaction between electrons is weak compared to the spin-orbit interaction of each electron. In this case, the total angular momentum is given by the jj-coupling scheme. Here, the orbital and spin angular momenta of each electron, $\hat{\boldsymbol{l}}_i$ and $\hat{\boldsymbol{s}}_i$, are first coupled to form the individual total angular momentum $\hat{\boldsymbol{j}}_i = \hat{\boldsymbol{l}}_i + \hat{\boldsymbol{s}}_i$. The total angular momentum of the ion is then obtained by summing over all electrons

$$\hat{\boldsymbol{J}} = \sum_i^N \hat{\boldsymbol{j}}_i. \tag{2.4}$$

For light ions with small atomic numbers Z, the electronic Coulomb interaction dominates over the spin-orbit interaction. In this case, the total angular momentum is described by the LS-coupling scheme. First, the individual orbital angular momenta $\hat{\boldsymbol{l}}_i$ and spins $\hat{\boldsymbol{s}}_i$ are coupled to form the total orbital angular momentum $\hat{\boldsymbol{L}} = \sum_i^N \hat{\boldsymbol{l}}_i$ and the total spin $\hat{\boldsymbol{S}} = \sum_i^N \hat{\boldsymbol{s}}_i$. The total angular momentum of the ion is then given by

$$\hat{\boldsymbol{J}} = \hat{\boldsymbol{L}} + \hat{\boldsymbol{S}}. \tag{2.5}$$

The ground state of the total angular momentum in the LS-coupling scheme can be

determined using Hund's third rule. According to this rule, for shells that are less than half-filled, the total angular momentum is given by $J = |L - S|$, whereas for subshells that are more than half-filled, $J = |L + S|$.

If the spin-orbit interaction is strong compared to the Zeeman effect, the Zeeman interaction can be treated as a first-order perturbation. In this case, it can be reformulated in the basis of the total angular momentum, as

$$\hat{\mathcal{H}}_{\mathrm{Z}} = \mu_{\mathrm{B}} g_J \boldsymbol{B} \cdot \hat{\boldsymbol{J}} \tag{2.6}$$

with the Landé g-factor

$$g_J = 1 + \frac{J(J+1) - L(L+1) + S(S+1)}{2J(J+1)}. \tag{2.7}$$

Brillouin function

Based on the Zeeman Ham.(2.6), the magnetisation of a paramagnetic system in an external magnetic field can be described by

$$M = n g_J \mu_{\mathrm{B}} \langle m_J \rangle = M_{\mathrm{S}} B_J(x), \tag{2.8}$$

where n is the density of magnetic moments and $\langle m_J \rangle$ the expectation value of the magnetic quantum number. The saturation magnetisation M_{S} is defined as

$$M_{\mathrm{S}} = n g_J \mu_{\mathrm{B}} J, \tag{2.9}$$

and the Brillouin function $B_J(x)$ is expressed as

$$B_J(x) = \frac{2J+1}{2J} \coth\left(\frac{2J+1}{2J} x\right) - \frac{1}{2J} \coth\left(\frac{1}{2J} x\right) \tag{2.10}$$

$$\text{with} \qquad x = \frac{g_J \mu_{\mathrm{B}} J B}{k_{\mathrm{B}} T}.$$

This function is shown in fig. 2.1(a) for different values of J.

Curie Law

The (static) magnetic susceptibility χ is defined as

$$\chi = \frac{M}{H} \approx \frac{\mu_0 M}{B}, \tag{2.11}$$

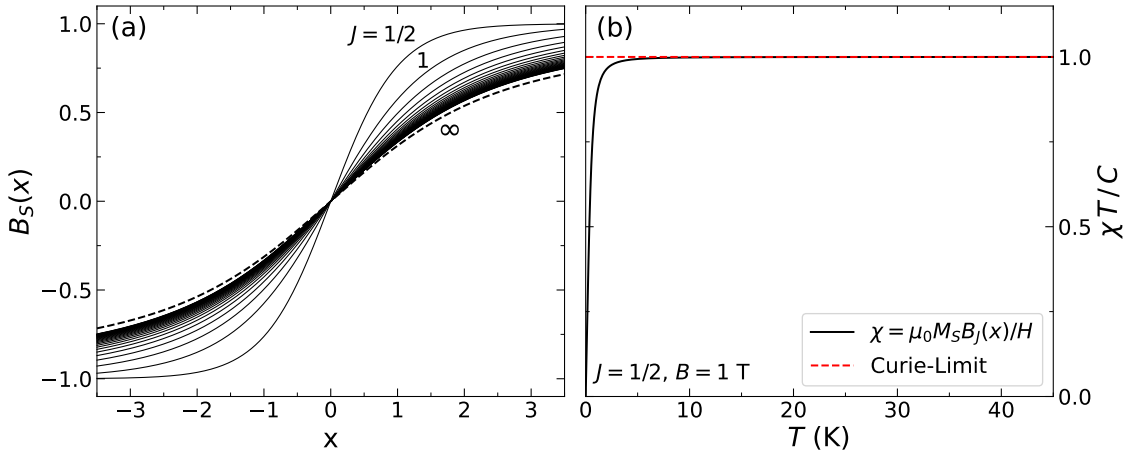


Figure 2.1: (a) Brillouin function $B_S(x)$ for different values of J. (b) Temperature dependence of χT calculated from eq. (2.8) for $J = 1/2$ and $B = 1$ T, in units of C. The dashed line indicates the Curie limit, as described by eq. (2.12).

with H being the magnetic field strength ($B = \mu_0(H + M)$) and μ_0 the vacuum permeability. For high temperatures and low fields $k_\mathrm{B}T \gg \mu_\mathrm{B}B$, which is the approximation in eq. (2.9), the magnetic susceptibility can be described by the Curie law

$$\chi = \frac{C}{T} \qquad \text{with} \qquad C = \frac{n\mu_0 g_J^2 \mu_\mathrm{B}^2 J(J+1)}{3k_\mathrm{B}}. \tag{2.12}$$

Fig. 2.1(b) shows χT as a function of temperature for a $J = 1/2$ system at an applied magnetic field of 1 T. The dashed line represents the Curie limit. As can be seen, χT approaches the constant value C in the high-temperature regime.

2.4 The Crystal Field

In a solid, an ion is surrounded by neighbouring atoms or ligands and therefore experiences an additional electrostatic interaction with the electrons of its local environment, known as the crystal-field interaction $\hat{\mathcal{H}}_\mathrm{CF}$. The strength of this interaction depends strongly on the involved orbitals.

The crystal field Hamiltonian is expressed in various ways in the literature. The most commonly used representation is the Stevens formalism [20]:

$$\hat{\mathcal{H}}_\mathrm{CF} = \sum_{N=0}^{2S} \sum_{k=-N}^{N} B_N^k \hat{O}_N^k \left(\hat{\boldsymbol{J}}\right), \tag{2.13}$$

where B_N^k are the real-valued Stevens parameters and $\hat{O}_N^k$ the Steven operators. Eq. (2.13) lifts the degeneracy of the m_J levels in zero external magnetic field; this is therefore referred to as zero-field splitting (ZFS). A more detailed description of the

Stevens formalism and the crystal field can be found in Ref. [8]. It is often sufficient to consider only the quadratic terms in $\hat{\boldsymbol{J}}$. This reduces the crystal field Hamiltonian to

$$\hat{\mathcal{H}}_{\mathrm{CF}} = \hat{\boldsymbol{J}} \overleftrightarrow{D} \hat{\boldsymbol{J}}. \tag{2.14}$$

Here, $\overleftrightarrow{D}$ is a real, symmetric tensor. In the eigenframe of $\overleftrightarrow{D}$, eq. (2.14) takes the form

$$\hat{\mathcal{H}}_{\mathrm{CF}} = D_{xx}\hat{J}_x{}^2 + D_{yy}\hat{J}_y{}^2 + D_{zz}\hat{J}_z{}^2, \tag{2.15}$$

where the z axis is chosen as the principal axis, i.e., $|D_{zz}| \geq |D_{xx}|, |D_{yy}|$. By Subtracting the constant value $(1/2)(D_{xx} + D_{yy})J(J+1)$, the physical properties are not changed and one obtains

$$\hat{\mathcal{H}}_{\mathrm{CF}} = D\hat{J}_z^2 + E(\hat{J}_x^2 - \hat{J}_y^2) \tag{2.16}$$

with

$$D = D_{zz} - \frac{D_{xx} + D_{yy}}{2} \qquad \text{and} \qquad E = \frac{D_{xx} - D_{yy}}{2}. \tag{2.17}$$

Subtracting $DJ(J+1)/3$ from eq. (2.16) yields

$$\hat{\mathcal{H}}_{\mathrm{CF}} = D\left(\hat{J}_z^2 - \frac{J(J+1)}{3}\right) + E\left(\frac{\hat{J}_+^2 + \hat{J}_-^2}{2}\right). \tag{2.18}$$

The advantage of eq. (2.18) is that it fulfils $\mathrm{tr}\left(\hat{\mathcal{H}}_{\mathrm{CF}}\right) = 0$. It is common to limit the ratio E/D to

$$-1/3 \leq E/D \leq +1/3, \tag{2.19}$$

because for $|E/D| \geq 1/3$, it is physically equivalent to relabelling the coordinate axes. If D is negative, the levels with the largest $|m_J|$ have the lowest energy, corresponding to an easy-axis magnetic anisotropy. If D is positive, the levels with the smallest $|m_J|$ are energetically favoured, corresponding to an easy-plane magnetic anisotropy. A non-zero E introduces transverse anisotropy, which leads to a preferential alignment of the magnetic moments along either the x or y direction. The last term of eq. (2.18) then lifts the remaining degeneracy between states with the same $|m_J|$ by mixing the m_J states.

The electrons in $4f$ orbitals are located close to the nucleus and are effectively shielded by the filled $5s$ and $5p$ orbitals. Consequently, the spin-orbit coupling is much stronger than the crystal-field interaction, $\hat{\mathcal{H}}_{\mathrm{SOC}} \gg \hat{\mathcal{H}}_{\mathrm{CF}}$. As discussed above, the crystal field therefore lifts the degeneracy of the m_J levels.

In contrast, the situation for $3d$ ions is completely different. The $3d$ orbitals of the metal ion have a relatively large spatial extent and, therefore, exhibit a significant overlap with the ligand orbitals. Therefore the crystal-field interaction is much stronger than the spin-orbit coupling, $\hat{\mathcal{H}}_{\mathrm{CF}} \gg \hat{\mathcal{H}}_{\mathrm{SOC}}$. The strong crystal field gives rise to an energy splitting of the originally degenerated $3d$ atomic states. The resulting splitting of the $3d$ orbitals depends sensitively on the symmetry of the local coordination environment. Fig. 2.2 illustrates the crystal-field splitting for tetrahedral and octahedral crystal fields [21]. These two coordination geometries occur repeatedly throughout this thesis.

If the magnetic ground state of $3d$ ions is calculated using Hund's rules and compared with experimental observations, it turns out that a total angular momentum with $J \approx S$, and, thus, an effective orbital angular momentum of $L \approx 0$, provides a much better description of the experimental results. This effect is commonly referred to as *orbital quenching*. Orbital quenching arises as a direct consequence of the fact that, for $3d$ ions, the crystal-field interaction is significantly stronger than the spin-orbit coupling and, therefore, Hund's rule no longer apply. In reality, however, the orbital angular momentum is often only partially quenched. Then, spin-orbit coupling cannot be entirely neglected and can be accounted for using second-order perturbation theory, which gives rise to an effective Zeeman term:

$$\hat{\mathcal{H}}_{\mathrm{Z}} = \mu_{\mathrm{B}} \boldsymbol{B} \overleftrightarrow{g} \hat{\boldsymbol{S}}, \tag{2.20}$$

where $\overleftrightarrow{g}$ is a tensor, reflecting the magnetic anisotropy of the system.

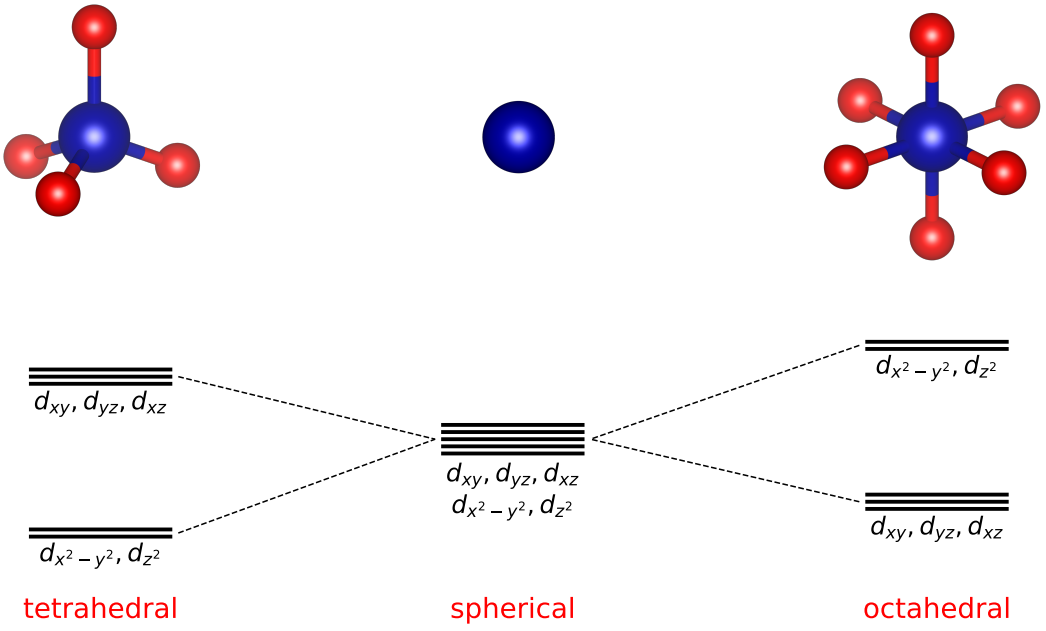


Figure 2.2: Crystal-field splitting of the 3d orbitals in tetrahedral and octahedral crystal fields environments relative to the free-ion. Blue and red spheres represent the magnetic ion and the ligands, respectively.

2.5 Spin-Spin Interaction

So far, we have considered a paramagnetic ion either in isolation or in a crystal field. Magnetic interactions between magnetic ions are commonly referred to as spin-spin interactions and can arise from different mechanisms. The magnetic *dipole-dipole interaction* is probably the most intuitive spin-spin interaction, as it can be understood in terms of the classical magnetic field produced by one ion acting on the magnetic moment of another. This interaction is relatively weak, with a coupling energy on the order of 1 K, and is typically smaller than other magnetic interactions.

In most magnetic systems, the dominant interaction mechanism is the *exchange interaction*. This is a quantum-mechanical phenomenon arising from the Pauli exclusion principle and Coulomb repulsion. *Direct exchange*, which depends on the overlap of the orbitals of two magnetic ions, is typically weak, since the interatomic distances are usually larger than the spatial extent of the orbitals [21]. Instead, the dominant mechanism is often the so-called *superexchange interaction*, in which the coupling between magnetic ions is mediated by non-magnetic ions. The sign and magnitude of the exchange interaction depend on several factors, in particular, the specific lattice structure of the material, the presence of multiple exchange pathways, and the specific orbital structure of the ions involved. The Goodenough–Kanamori–Anderson rules provide a qualitative approach to estimate the sign and strength of the exchange interaction in $3d$ transition-metal systems [21].

In the presence of spin-orbit coupling, the exchange coupling can be anisotropic. Therefore, the exchange Hamiltonian can be written as

$$\hat{\mathcal{H}}_{\text{ex}} = \hat{\boldsymbol{S}}_1 \overleftrightarrow{J} \hat{\boldsymbol{S}}_2, \tag{2.21}$$

with an anisotropic interaction tensor $\overleftrightarrow{J}$. Decomposing $\overleftrightarrow{J}$ into an isotropic and an anisotropic part, eq. (2.21) can be rewritten as

$$\hat{\mathcal{H}}_{\text{ex}} = -J \hat{\boldsymbol{S}}_1 \hat{\boldsymbol{S}}_2 + \hat{\boldsymbol{S}}_1 \overleftrightarrow{A} \hat{\boldsymbol{S}}_2 + \boldsymbol{d} \left(\hat{\boldsymbol{S}}_1 \times \hat{\boldsymbol{S}}_2 \right). \tag{2.22}$$

The first term corresponds to the isotropic Heisenberg interaction, the second term to the symmetric anisotropic contribution, and the third term to the antisymmetric anisotropic component of the magnetic interaction. In most cases, the isotropic term is the dominant contribution. A positive exchange parameter ($J > 0$) leads to a parallel (ferromagnetic) spin configuration, whereas a negative value ($J < 0$) results in an antiparallel (antiferromagnetic) alignment.

2.6 Electron Paramagnetic Resonance

Electron Paramagnetic Resonance (EPR) is a spectroscopic technique that uses microwave absorption to probe transitions between spin states. It, therefore, provides access to important information about the magnetic properties of a system and the

underlying spin Hamiltonian. A spin system is placed in an external magnetic field and irradiated with microwave radiation of frequency ω. The spin system can then absorb a microwave photon and undergo a transition from an occupied initial state to an empty final state. When the microwave energy matches the energy difference between these states, resonant absorption occurs:

$$\Delta E = E_\mathrm{f} - E_\mathrm{i} = \hbar\omega. \tag{2.23}$$

To illustrate the principle of EPR, fig. 2.3(a) shows the energy level diagram together with the corresponding transition energies in fig. 2.3(b) of a spin system with $S = 1$ and $D < 0$, $E = 0$. The magnetic field is aligned with the easy-axis of the system. Due to the anisotropy, the $|m_S\rangle = |0\rangle$ state is energetically separated from the degenerate $|m_S\rangle = |\pm 1\rangle$ states at zero magnetic field. The red arrows indicate exemplary the symmetry allowed transitions with $\Delta m_S = \pm 1$, which appear as minima in the transmission spectra at the corresponding magnetic field values.

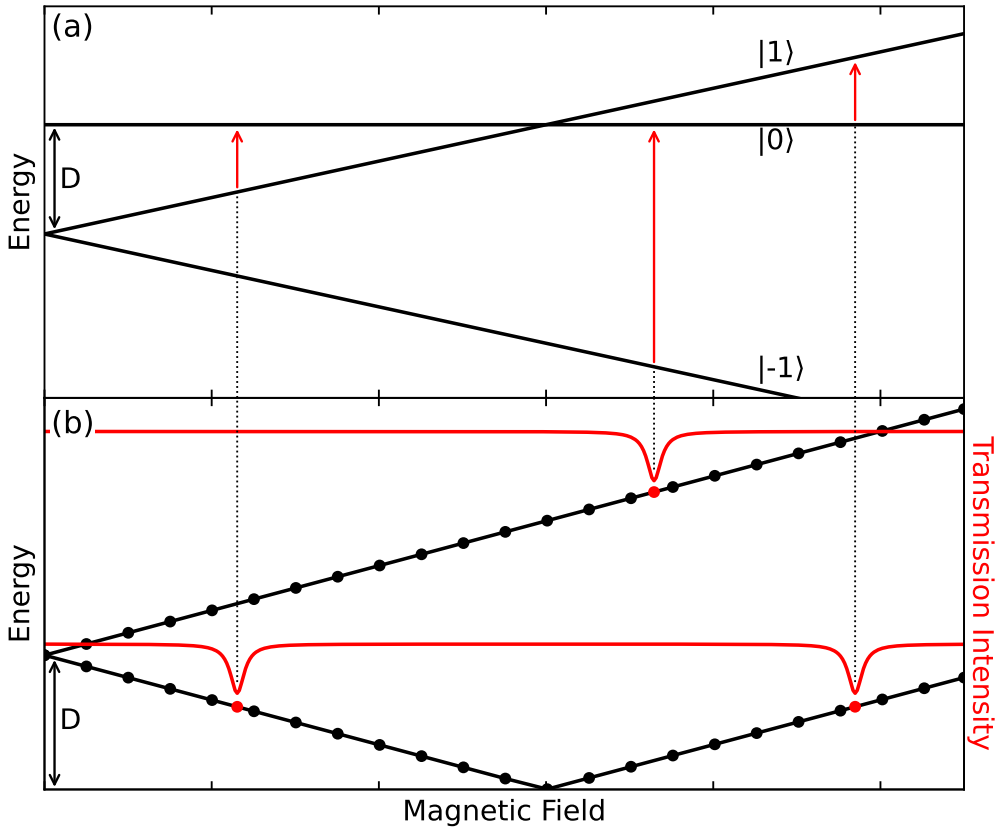


Figure 2.3: (a) Energy level diagram for an spin system with $S = 1$ and $D < 0$, $E = 0$. The magnetic field is aligned with the easy-axis of the system. Red arrows indicate allowed transitions. (b) Transition energies for $\Delta m_S = \pm 1$ and the corresponding transmission spectra.

2.7 Magnetic Relaxation

The establishment of thermodynamic equilibrium in a spin system requires a certain amount of time. Therefore, the macroscopic magnetisation cannot respond immediately to changes in the external magnetic field and lags slightly behind. Such effects can be probed by AC magnetic susceptibility measurements, in which a small oscillating magnetic field is applied to the sample. This subchapter is based on [2, 22]. Unless stated otherwise, the following information has been taken from there.

2.7.1 AC Susceptibility

In AC magnetic susceptibility measurements the sample is exposed to a time-dependent external magnetic field

$$B(t) = B_{\mathrm{dc}} + B_{\mathrm{ac}} \cos(\omega t), \tag{2.24}$$

where B_{dc} denotes the static (time-independent) component of the magnetic field, and B_{ac} is the amplitude of the oscillating magnetic field. Depending on the characteristic relaxation time τ of the spin system relative to the angular frequency ω of the applied AC field, three distinct regimes can be identified:

$\omega \ll 1/\tau$: The response time of the system is much faster than the frequency of the external magnetic field. Consequently, the spin system follows the applied AC field, and the corresponding magnetic response is described by the isothermal susceptibility χ_T.

$\omega \gg 1/\tau$: When the oscillating magnetic field varies much faster than the characteristic response time of the system, the spin system can no longer follow the field. As a result, it does not reach thermal equilibrium, and the magnetic response is described by the adiabatic susceptibility χ_S.

$\omega \approx 1/\tau$: When the characteristic timescale of the magnetic relaxation becomes comparable to the frequency of the oscillating magnetic field, the magnetisation lags behind the applied AC field, and the response is characterised by an in-phase (real) and an out-of-phase (imaginary) component of the susceptibility, denoted by χ' and χ'', respectively.

For a system of weakly interacting magnetic moments, the complex AC susceptibility can be written as

$$\chi(\omega) = \chi'(\omega) + i\chi''(\omega) = \chi_{\mathrm{S}} + \frac{\chi_{\mathrm{T}} - \chi_{\mathrm{S}}}{1 + i\omega\tau}, \tag{2.25}$$

which is also known as the Debye model [23]. The in-phase and out-of-phase components of the susceptibility are given by:

$$\chi'(\omega) = \chi_S + \frac{(\chi_T - \chi_S)}{1 + \omega^2\tau^2} \qquad \text{and} \qquad \chi''(\omega) = \frac{(\chi_T - \chi_S)}{1 + \omega^2\tau^2}\omega\tau. \tag{2.26}$$

Fig. 2.4 shows the frequency dependence of the in-phase and out-of-phase components of the AC magnetic susceptibility. The out-of-phase component, χ'', exhibits a maximum at $\omega\tau = 1$ and approaches zero in the limits $\omega \to 0$ and $\omega \to \infty$. In contrast, the in-phase component, χ', decreases from the isothermal susceptibility χ_T at low frequencies to the adiabatic susceptibility χ_S at high frequencies.

In real systems, structural disorder or local variations lead to a distribution of the magnetic relaxation times. This effect is commonly described using a generalised Debye model that introduces a phenomenological parameter α and is expressed as

$$\chi(\omega) = \chi_S + \frac{\chi_T - \chi_S}{1 + (i\omega\tau)^{1-\alpha}}, \tag{2.27}$$

where $0 \leq \alpha \leq 1$. The "generalised double-Debye function", which consists of the sum of two generalised Debye functions, is employed to account for two independent relaxation processes.

2.7.2 Magnetic Relaxation Processes

The magnetic relaxation time τ characterises the rate at which the macroscopic magnetisation of the system returns to thermal equilibrium after excitation. In general, τ is governed by multiple relaxation mechanisms, each contributing with a different temperature dependence to the overall relaxation rate. Several processes may

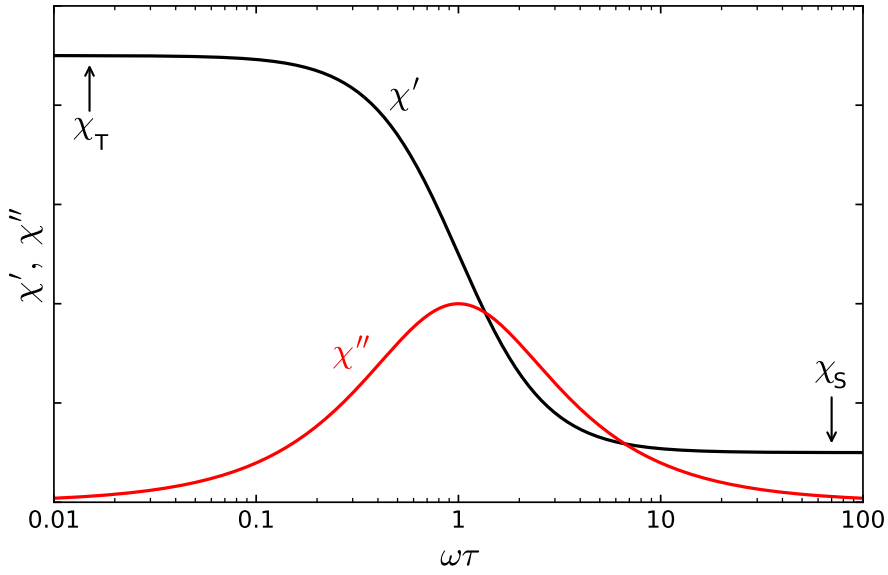


Figure 2.4: Frequency dependence of the in-phase (black line) and out-of-phase (red line) components of the AC susceptibility. The maximum of χ'' occurs at $\omega\tau = 1$.

act simultaneously, and their relative importance depends on the specific properties of the system under investigation. In the following, the four most relevant relaxation mechanisms are introduced:

Direct Relaxation: A transition between two energy levels can occur via the absorption or emission of a single phonon (one-phonon process). This mechanism is typically weak at low temperatures, due to the low density of states of low-energy phonons. The corresponding relaxation rate scales linearly with temperature, reflecting the fact that the number of thermally available phonons increases proportional to T. The relaxation rate is therefore given by

$$\tau_{\text{direct}}^{-1} = AT, \tag{2.28}$$

where A is a temperature-independent parameter.

Orbach Relaxation: This relaxation mechanism involves two phonons. In a first step, a phonon is absorbed by the spin system, to make a transition to an excited state. After that, a second phonon with a different energy is emitted, allowing the system to relax into the final state. In this process, the system effectively overcomes an energy barrier U_{eff}, and the corresponding relaxation rate can, therefore, be described by

$$\tau_{\text{Orbach}}^{-1} = \tau_0^{-1} e^{-U_{\text{eff}}/k_{\text{B}}T}, \tag{2.29}$$

with τ_0^{-1} being the high-temperature relaxation rate.

Raman Relaxation: Similar to the Orbach mechanism, the Raman process is a two-phonon process. However, the intermediate state is virtual rather than a real excited state. The relaxation rate can, therefore, be effectively described by

$$\tau_{\text{Raman}}^{-1} = \tau_{\text{R}}^{-1} \frac{e^{-W/k_{\text{B}}T}}{(e^{-W/k_{\text{B}}T} - 1)^2}, \tag{2.30}$$

where τ_{R}^{-1} is the high-temperature relaxation rate and W is of the order of the optical phonon modes at the Γ-point[24].

Quantum Tunnelling of the Magnetisation (QTM): The spin system transitions between magnetic states by tunnelling through a potential energy barrier. This process can occur due to a mixing of spin states, for instance, induced by a transverse anisotropy. Since no phonons are involved, the corresponding relaxation rate τ_{QTM}^{-1} is temperature-independent. QTM can be effectively suppressed by applying a static external field.

To obtain the total relaxation rate, the rate of the different mechanisms add up reciprocal:

$$\tau^{-1} = \tau_{\text{direct}}^{-1} + \tau_{\text{Orbach}}^{-1} + \tau_{\text{Raman}}^{-1} + \tau_{\text{QTM}}^{-1}. \tag{2.31}$$

Due to their different temperature dependencies, QTM dominates in the low-temperature limit ($T \to 0$). At higher temperatures, the Orbach process becomes the dominant relaxation mechanism. Consequently, the effective energy barrier U_{eff} can be extracted from the magnetic relaxation behaviour in the high-temperature regime.

3 Experimental Methods

This chapter gives an overview about the experimental techniques of magnetometry and high-frequency/high-field electron paramagnetic resonance spectroscopy (HF-EPR). The corresponding experimental setups, sample preparations, and data processing methods are described in detail. In addition, relevant measurement-related and instrumental aspects that may influence the experiments are discussed.

3.1 Magnetometry

3.1.1 Experimental Setup (MPMS3)

For static and dynamic magnetisation measurements, a Magnetic Properties Measurement System (MPMS3, *Quantum Design*) was used. Detailed information of its functionality can be found in the corresponding user manual [25]. Unless stated otherwise, the following information has been taken from there. The MPMS3 provides magnetic fields of up to 7 T and a temperature range from 1.8 K to 400 K, with the sample chamber being cooled by liquid helium evaporation within a cryostat. Using the optional iQuantum ^{3}He-option, the temperature range can be extended down to 0.4 K [26].

For direct current (DC) magnetisation measurements, the sample is slowly moved through pick-up coils. The magnetic moment of the sample induces a voltage, which is detected using a superconducting quantum interference device (SQUID). This results in a voltage-position curve, as can be seen in fig. 3.1. The black dots represents the measured data to which a dipole response function can be fit (red line). From this fit, the magnetic moment of the sample is obtained.

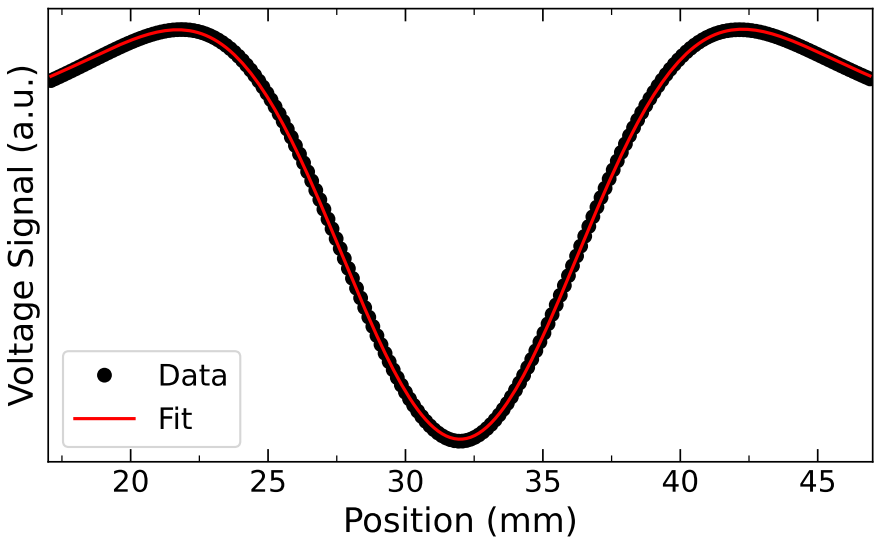


Figure 3.1: Measured voltage-position curve (black dots) and fit dipole response function (red line) of a paramagnetic sample in the MPMS.

For alternating current (AC) susceptibility measurements, an additional oscillating magnetic field is applied. In the MPMS, frequencies between 1 Hz and 1000 Hz are accessible [27]. All AC susceptibility measurements in this work were performed using the three-point method, in which the time-dependent magnetic moment is measured at three different positions within the coil setup.

3.1.2 Sample Preparation

Unless stated otherwise, all measurements were performed on polycrystalline powder samples. The VSM powder sample holders (QDC-4096-388, *Quantum Design*) were used to mount the samples and can be seen in fig. 3.2(a). Each holder consists of two parts: the powder is placed into the open end of one part, and the other part serves as a stamp, which is inserted into the first part to seal the sample, thereby forming a capsule (see fig. 3.2(b)).

To prevent the alignment of samples with strong magnetic anisotropy in the external magnetic field, Eicosane ($C_{20}H_{42}$) was added to the sample capsule during the preparation. When heated slightly ($\approx 50°C$), the Eicosane melts and, upon cooling to room temperature, it fixes the crystallites in random orientations. For samples with low anisotropy, compressing the powder with the stamp is sufficient to avoid alignment. This also avoids overlaying of the magnetic signal from the sample with the diamagnetic contribution of the Eicosane, which can be relevant for measurements

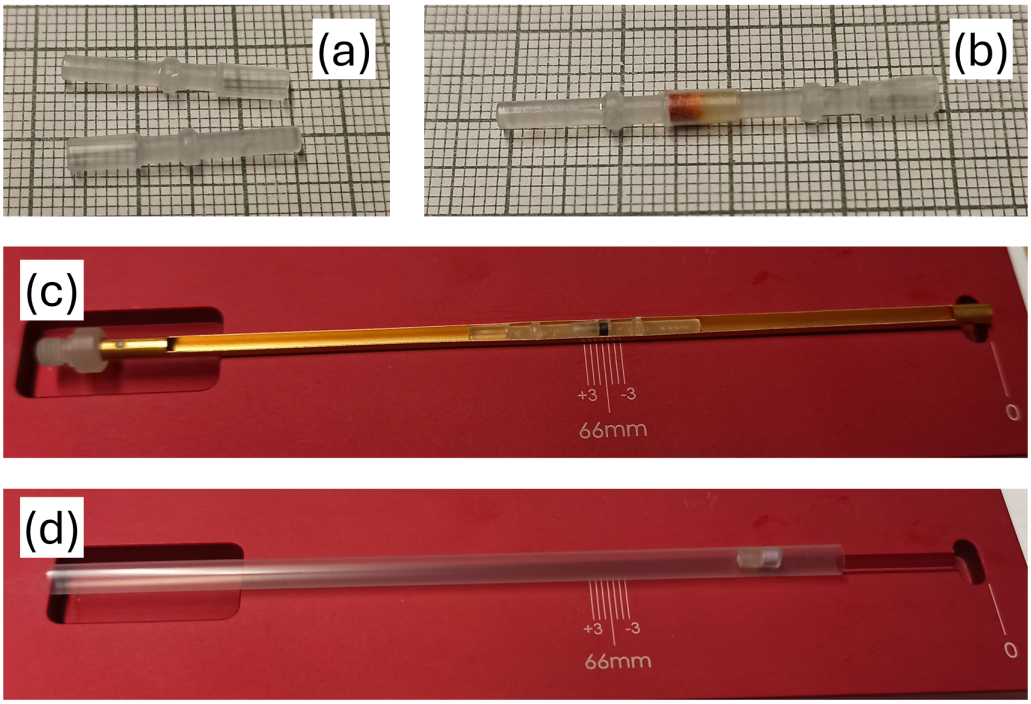


Figure 3.2: (a) Empty powder sample holders; (b) filled and sealed sample capsule; (c) sample capsule in brass holder; (d) cut sample capsule glued into a straw with grease. The figure is taken from [28].

of small magnetic moments (see chapter 6). The prepared capsule was then clicked into a brass holder or a glued into a straw using grease (see fig. 3.2(c) and (d)), which was mounted onto a sample rod and inserted into the MPMS. Unless stated otherwise, all measurements were performed in a brass holder.

3.1.3 Background Correction

To account for the contribution of the capsule and the brass holder to the signal of the measured magnetic moment, the same measurements that were performed with the sample also need to be performed without the sample, using an empty capsule. The empty capsule should, therefore, be fixed in the brass holder in the exact same position as during the measurement with the sample. This position can be determined with a caliper to an accuracy of ± 0.1 mm.

Since each individual capsule exhibits a slightly different magnetic signal, it would be optimal to measure the exact same capsule each time before filling it with the sample. However, measuring the same capsule beforehand is impractical, because the powder's compression, the resulting volume, and the final capsule dimensions are not known before the sample is prepared. Consequently, the empty capsule would have to be measured after the sample measurement, which requires removing the sample and cleaning the capsule. However, since this procedure destroys the sample and is not always easily possible, it was performed only for the measurements discussed in chapter 6.

To determine whether the signal of a different capsule can be used for background subtraction, the variation in the signal between individual capsules was tested. Fig. 3.3 shows the voltage-position curves of three different capsules at four different temperatures at $B = 1$ T. All capsules were mounted at the same position in the brass holder. Note that these curves do not exhibit a dipole-like behaviour, as the capsule has a large spatial extent compared to the pick-up volume of the detection coils in the MPMS. At 300 K (fig. 3.3(d)), the three capsules exhibit very similar signals. A maximum at approximately 47 mm occurs at nearly the same position for all capsules, while a maximum at approximately 23.5 mm shows a slightly larger deviation. Interestingly, the position of the intermediate minimum varies significantly more, with a difference of approximately 1.5 mm between capsule 2 and capsule 3. At lower temperatures, down to 11.4 K, the scans remain almost the same. The signals of capsule 1 and capsule 2 overlap well over a wide position range and start to deviate more noticeably only above approximately 41 mm. In contrast, capsule 3 shows significantly larger differences, compared to capsule 1 and capsule 2, most prominently in the amplitude of the maximum ($\approx$ 23.5 mm) and the minimum. A significant difference between the individual capsule scans is observed at 1.8 K, with each voltage-position curve exhibiting a completely different behaviour. The minimum for capsule 1 and capsule 2 is shifted to a lower position, whereas for capsule 3 it is now much broader. The signal of capsule 1 shows a maximum at

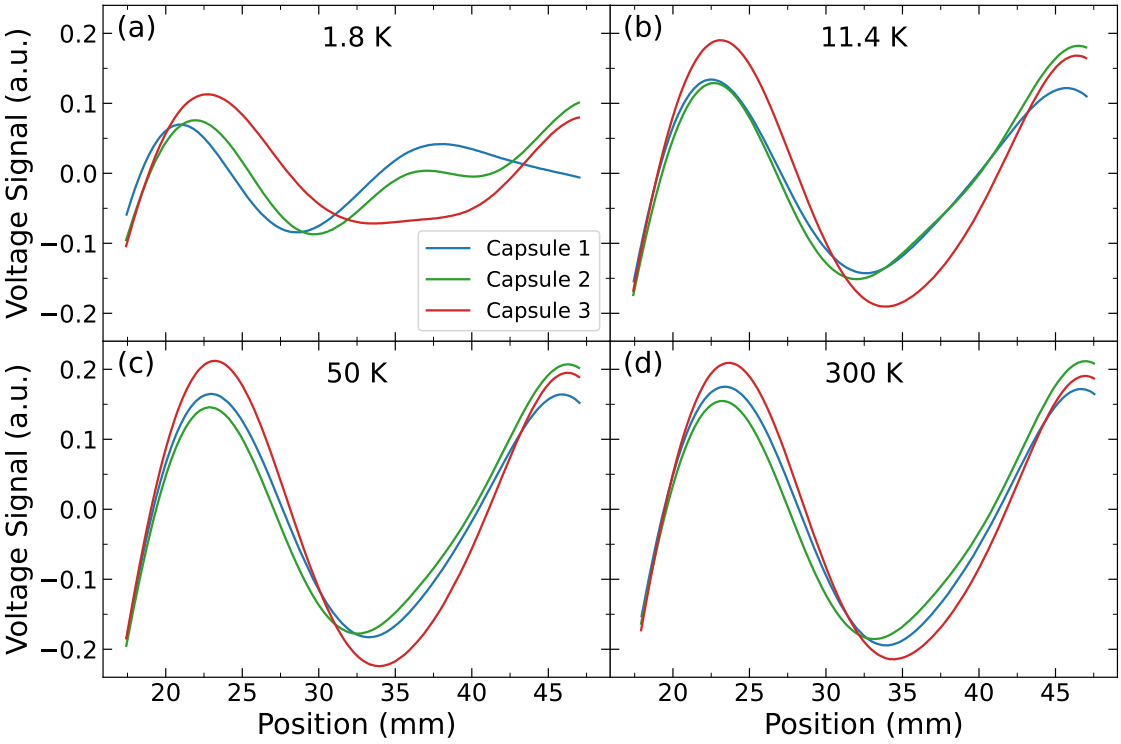


Figure 3.3: Voltage-position curves of three different capsules at four different temperatures at $B = 1$ T.

approximately 38 mm, while the scan of capsule 2 displays both a maximum and a second local minimum in this position range. The signals of capsule 2 and capsule 3 continue to increase toward higher positions in contrast to that of capsule 1.

In conclusion, the voltage–position curves of different capsules exhibit similar behaviour over a wide temperature range. Significant deviations between the signals of different capsules occur only at temperatures below 11.4 K. However, in this low-temperature regime, the magnetic moments of the investigated samples is typically much stronger than that of the capsule, making the capsule contribution negligible. In principle, if the sample cannot simply be washed out of the capsule, it should, therefore, be possible to use the signal of a different capsule for background subtraction. In practice, however, this approach does not always yield reliable results, even at higher temperatures (see Appendix).

Furthermore, the voltage–position curves of the capsules are almost temperature independent down to 11.4 K. Consequently, at higher temperatures, where the signal of the investigated samples is typically smaller, the capsule contribution can be treated as temperature-independent to first order. Throughout this thesis, the treatment of the capsule background is described individually in each chapter. If the background signal was subtracted from the sample signal, this was done using the SQUIDLab software [29].

The origin of the differences observed in the voltage-position curves of the individual capsules, particularly at low temperatures, could not be clearly identified. A closer

inspection of the two parts of the capsule (see fig. 3.2(a)) reveals noticeable gas inclusions, which may contribute to the non-reproducible magnetic response. For samples with a small magnetic moment, the contribution of the capsule significantly complicates the background correction, especially at low temperatures. To address this issue, a 3D-printed sample holder is currently being developed by Thomas Kerschenbauer in the working group, with promising preliminary results.

3.1.4 Sample Shape Effects

The MPMS was calibrated using a palladium calibration cylinder (height = 3.80 mm, diameter = 2.80 mm, and radial offset = 0 mm). Any deviations in the shape or position of the measured sample from this standard will affect the measured magnetisation. Therefore, *Quantum Design* provides a software tool (MPMS 3 Sample Geometry Simulator) that calculates a correction factor based on the geometry and position of the sample, by which the measured magnetisation must be divided to obtain the true value. The greater the deviation of the sample shape and position from that of the palladium calibration cylinder, the larger the correction factor. For powder samples in capsules measured in the brass holder, the relative deviation is typically small, ranging between 1–3%, depending on the sample volume height. Since the correction software was not available to the working group from the beginning of this thesis, not all measurements were be corrected using this factor.

3.1.5 Influence of Sample Holders on AC Susceptibility

In the context of dynamic magnetisation measurements (AC susceptibility), the choice of the sample holder represents a potential source of error. In particular, for conductive materials such as brass, eddy currents can be induced by the applied varying magnetic field. These currents generate a counter field, which can lead to a partial shielding of the external magnetic field and, thus, affect the measured dynamic susceptibility of the sample. In contrast, measurements performed using a straw sample holder are expected to be free of such effects.

In this thesis, AC magnetic susceptibility measurements of the investigated samples using brass and straw sample holders revealed significant differences in the measured signals, with the straw measurements exhibiting untypical behaviour. Since comparable effects were not observed for other samples within the working group [30], the origin of this discrepancy remained unclear.

To investigate whether the observed differences can be attributed to shielding effects caused by eddy currents in the brass sample holder, measurements were performed on a reference sample of Gadolinium Gallium Garnet (GGG) from *Quantum Design*. This reference sample is characterised by a purely in-phase AC susceptibility in the relevant temperature and frequency range [31]. The measurements of GGG were performed for three different sample holders: brass, straw and a quartz tube. The

quartz tube sample holder is specifically designed for AC reference measurements and is free of potential shielding effects.

Assuming that eddy currents in the brass sample holder reduce the effective magnetic field, a corresponding reduction in the absolute value of the measured complex susceptibility would be expected. In particular, such an effect should, therefore, be visible in the in-phase component of the susceptibility $\chi'(\omega)$.

Fig. 3.4 shows the frequency dependence of the in-phase component of the AC susceptibility of GGG mounted in the three different sample holders at $T = 300$ K. As can be seen, the measurements obtained with the different sample holders show very similar behaviour over the investigated frequency range. The data recorded using the straw are systematically higher by approximately 2% compared to those obtained with the quartz tube and the brass sample holder. This deviation can be attributed to the mounting of the GGG sample in the straw, which introduces a radial offset of $r = 1.1(5)$ mm. The associated uncertainty is relatively large, as the straw cannot be perfectly aligned with the sample rod. Consequently, significant errors arise, which were estimated using the sample shape correction program. In contrast, for measurements performed with the quartz tube and the brass sample holder, the sample is positioned without a radial offset, and this source of error can, therefore, be neglected.

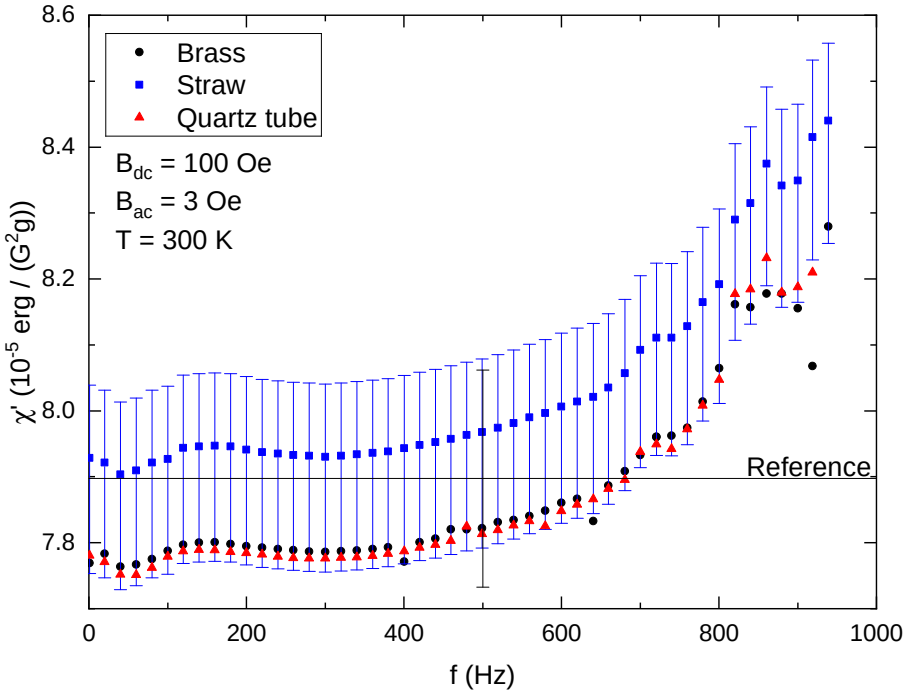


Figure 3.4: Frequency dependence of the in-phase component of the AC magnetic susceptibility of the GGG reference sample mounted in brass (black), straw (blue) and quartz (red) sample holders, measured by applying an AC magnetic field of 3 Oe and a static magnetic field of 100 Oe. The data was collected at $T = 300$ K.

Except for a small minimum at approximately 50 Hz, the expected frequency-independent behaviour is observed up to about 400 Hz. Above this frequency, $\chi'(\omega)$ increases with increasing frequency. For frequencies greater than 800 Hz, the measured values obtained with different sample holders begin to deviate significantly from each other. At such high frequencies, the measurement uncertainty also increases, which is attributed to the reduced sensitivity of the measurement system [30]. Considering the uncertainty arising from the radial offset in the straw measurements, the data are consistent with each other.

In conclusion, AC measurements can be performed in the brass sample holder without significant shielding effects. Therefore, the large differences observed in the AC measurements between the straw and the brass sample holder cannot be explained by shielding and must have another origin, which, however, could not be clearly identified. All AC measurements presented in this work were, therefore, performed using the brass sample holder.

3.1.6 Remanent Magnetic Field

The remanent magnetic field of the superconducting magnet is a potential source of uncertainty and can have a significant impact on measurements, particularly at small applied magnetic fields. The magnet of the MPMS can be driven to a specific magnetic field setpoint at a given rate using three different approach modes:

Linear: The magnetic field is ramped directly to the setpoint, maintaining the specified rate as closely as possible. A small field overshoot may occur.

No Overshoot: To avoid the possible overshoot in the linear approach mode, the ramp rate is reduced over the final 20% of the field change, allowing the magnetic field to approach the setpoint more gradually.

Oscillate: The setpoint is initially overshot by approximately 70% of the total field change at the specified rate, after which the magnetic field approaches the setpoint through damped oscillations.

To determine the influence of the different approach modes on the remanent field, a series of measurements was performed. For each measurement, the magnetic field was reduced to 0 T from various initial fields using the three approaches modes and their combinations. Subsequently, an $M(B)$ measurement was performed up to 30 Oe in steps of 10 Oe, and the magnetic field at which the magnetisation is extrapolated to zero was determined. The negative of this value corresponds to the remanent field. For example, if the $M(B)$ curve intersects the B-axis (corresponding to $M = 0$) at 5 Oe, this implies a remanent field of -5 Oe. To ensure reproducibility, the measurements were repeated multiple times on different days and using different samples. The measurement uncertainty is primarily determined by variations between measurements performed on different days. For all measurements, the magnetic field was ramped at a rate of 250 Oe/s.

Tab. 3.1 shows the remanent field after reducing the magnetic field from an initial field to 0 T using the "Oscillate" mode. Independent of the initial field, the absolute value of the remanent field is very small, ranging from 0.9(2) to 2.1(2) Oe, and does not vary significantly for measurements in the range of 0.1-1 T. Interestingly, after reducing the field from 7 T to 0 T, the remanent field exhibits an opposite sign. This may be related to whether the final approach to zero field occurs from a positive or a negative magnetic field.

The advantage of the "Oscillate" mode over to the other two modes in achieving a true zero field can be seen in tab 3.2. Both the "Linear" and the "No Overshoot" modes exhibit a remanent field that is approximately one order of magnitude larger than that obtained using the "Oscillate" mode.

When reducing the magnetic field to 0 T, it is therefore advantageous to use the "Oscillate" mode in order to minimise the remanent field. However, this approach requires significantly more time due to the overshoots. Consequently, a final series of measurements was performed to investigate the remanent field when the magnetic field is first reduced from 7 T to an intermediate field using the "Linear" mode and subsequently brought to 0 T using the "Oscillate" mode, thereby reducing the overall measurement time. The measured remanent fields can be seen in tab 3.3. While the remanent field is still relatively large for intermediate fields of 0.1 T and 0.2 T (over 15 Oe), it is already reduced to a value comparable to that obtained for 7 T for 1 T.

In order to reduce the magnetic field from 7 T to 0 T with minimal remanent field in a reasonably short time, it is, therefore, recommended to first ramp linearly to 1 T and then use the "Oscillate" mode from 1 T to 0 T.

Initial Field (T)	0.1	0.2	0.5	1.0	7.0
Remanent Field (Oe)	-1.6(4)	-2.1(2)	-1.3(2)	-0.9(2)	+1.8(2)

Table 3.1: Remanent field after reducing the magnetic field from different initial fields to zero using the "Oscillate" mode.

Approach Mode	Linear	No Overshoot	Oscillate
Remanent Field (Oe)	-28.4(2)	-30.9(4)	+1.8(2)

Table 3.2: Remanent field after reducing the magnetic field from an initial field of 7 T to zero using different approach modes.

Intermediate Field (T)	0.1	0.2	0.5	1.0	7.0
Remanent Field (Oe)	-23.1(7)	-15.2(6)	-3.0(2)	-1.2(1)	+1.8(2)

Table 3.3: Remanent field after first reducing the magnetic field from 7 T to an intermediate field using the "Linear" mode, and subsequently brought it to 0 T using the "Oscillate" mode.

3.2 High-frequency/High-field Electron Paramagnetic Resonance Spectroscopy

This subchapter is based on Refs. [28] and [32], which contain more detailed descriptions about the measurements system. Unless stated otherwise, the following information has been taken from there.

3.2.1 Experimental Setup

The HF-EPR setup is shown schematically in Fig. 3.5. The Millimeter Vector Network Analyzer (MVNA) by *AB Millimetre* serves as both the microwave source and detector. It generates two microwave signals with frequencies f_1 and f_2 in the range of 8 to 18 GHz. These frequencies are stabilised using an EIP 575B Source Locking Frequency Counter provided by *Phase Matrix*. One microwave signal is transmitted through coaxial cables into a harmonic generator (HG). In the HG, f_1 is multiplied by the harmonic number N, which depends on the particular HG used. In this work, harmonic numbers $N = 4$, 12, 18, 24, 36 and 54 were used, corresponding to a frequency range of approximately 30 GHz to 1 THz. The resulting

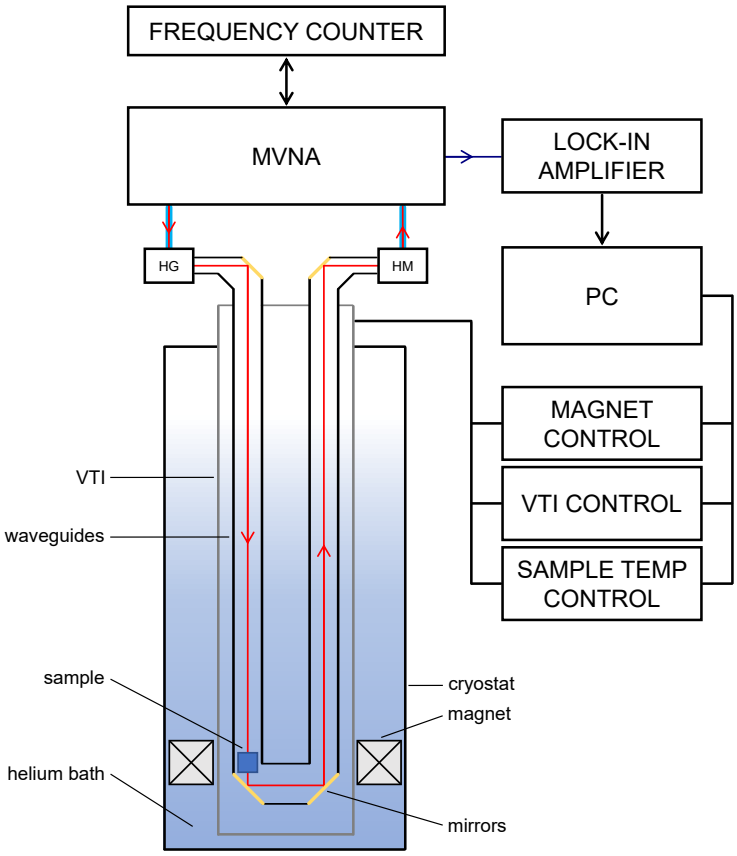


Figure 3.5: Schematic diagram of the HF-EPR setup. Further experimental details are provided in the text. The red arrows indicate the microwave path. The figure is adapted from [33].

microwave is guided via oversized circular waveguides to the sample, reflected by two gold mirrors, and directed into the harmonic mixer (HM), where it is mixed with f_2. Depending on the harmonic number, both the HG and the HM consist of Schottky diodes, attenuators, amplifiers, and filters, all produced by *AB Millimetre*. The received signal is filtered by an internal low-pass filter and, to improve the sensitivity, modulated with a frequency $f_{\mathrm{mod}} = 10.488$ kHz. The output is detected by a SR830 DSP Lock-In Amplifier (*Stanford Research Systems*), allowing both the amplitude and phase of the signal to be measured and read out by a home-written LabVIEW-based program on a PC.

All measurements are performed in a magneto-cryostat from *Oxford Instruments*, based on liquid helium evaporation. The superconducting magnet can generate fields from 0 to 16 T, and measurements can be performed in a temperature range of 1.8–300 K.

3.2.2 Sample Preparation

Polycrystalline powder samples were prepared in a brass ring (see fig. 3.6(a)), which was sealed on both sides with double-sided Kapton tape to prevent the sample from sticking (see fig. 3.6(b)). For loose powder measurements, the powder was filled into the brass ring without further preparation. In an external magnetic field, the crystallites align along their magnetic easy anisotropy axis, which becomes parallel to the field. As a result, only a single crystal orientation is measured, yielding pseud-single-crystal spectra. To preserve this alignment after the initial reorientation, the magnetic field was reduced only down to a maximum of 0.1 T during subsequent measurements.

For fixed powder measurements, Eicosane was added to the powder inside the brass ring. When heated slightly ($\approx 50°$C), the Eicosane melts and after cooling to room temperature, it fixes the crystallites in random orientations. This prevents the sample from aligning in the magnetic field, resulting in measurements that reflect an average of all possible crystal orientations.

After preparation, the sample ring is placed together with two empty brass rings into the sample base (see fig. 3.6(a)). The base is then fixed onto the mirror part (see

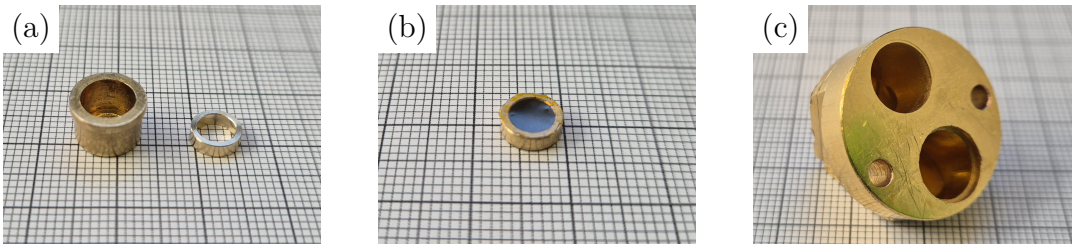


Figure 3.6: Pictures of the main components used for HF-EPR sample preparation. (a) Sample base (left) and empty brass ring (right); (b) filled brass ring sealed with Kapton tape; (c) mirror part.

fig. 3.6(c)) using Kapton tape and is afterwards mounted onto the waveguides. The waveguides including the sample are inserted into a sample rod, which is evacuated and flushed with helium three times, before being filled with helium to a pressure of 250 mbar to ensure good thermal contact. Finally, the sample rod is inserted into the cryostat.

3.2.3 Data Processing

The finite penetration depth of the microwaves can lead to an mixing of the absorption amplitude $A(B)$ and phase $D(B)$ [34]. This affects the shape of the measured resonance feature such that the resonance position is not equivalent to the maximum in $A(B)$. By recording both the amplitude $A_{\mathrm{meas}}(B)$ and the phase $D_{\mathrm{meas}}(B)$ simultaneously, the true amplitude signal can be reconstructed according to

$$A(B) = \frac{1}{\sqrt{1+\epsilon^2}} \left(A_{\mathrm{meas}}(B) - \epsilon \cdot D_{\mathrm{meas}}(B) \right), \tag{3.1}$$

where $|\epsilon| \leq 1$ is a phenomenological parameter that describes the mixing of one signal component into the other [35]. The effect of phase mixing is illustrated in fig. 3.7.

In (a), the true phase and absorption around a resonance feature are shown. (b) displays the measured absorption after phase mixing according to eq. (3.1). The measured absorption is no longer symmetric, and the position of the maximum in $A_{\mathrm{meas}}(B)$ no longer matches that of the actual absorption signal.

In the here presented data analysis, phase mixing was treated as follows: The true absorption spectrum was calculated according to eq. (3.1), and the value of ϵ was varied until $A(B)$ exhibited a constant baseline and the resonance features, in the case of sharp features without shoulders, assumed a Lorentzian-like line shape.

Thermal fluctuations as well as variations in the transmitted microwave power can affect the measured data. To account for this, the spectra are background-corrected. Unless stated otherwise a second-order polynomial is fit to each spectrum (after phase mixing corrections), excluding the frequency range where the observed resonance feature appears, and the resulting background is subtracted from the spectrum. For each microwave frequency, the magnetic field was swept up and down during the measurement to ensure reproducibility. In the subsequent analysis, both sweeps were taken into account. Simulations of the experimental data were performed using the EasySpin software package [36].

3.2.4 Setup Dependent Impurity Resonance

During the analysis of the HF-EPR spectra in this work, an additional resonance feature was observed in some samples within a narrow frequency interval around 67 GHz that was not present at other frequencies (see Appendix). Since such an

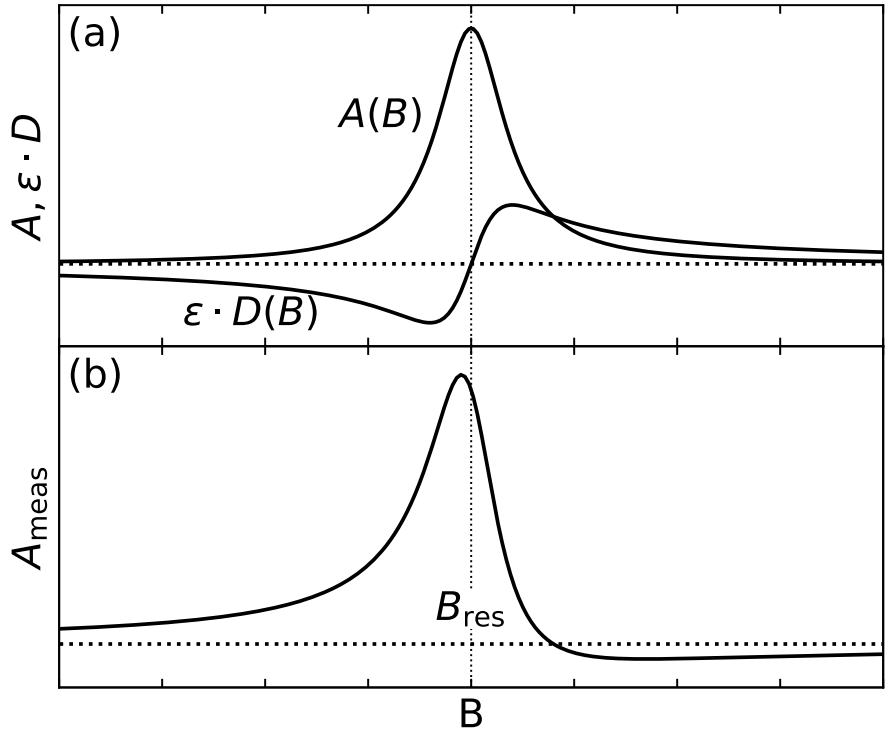


Figure 3.7: The effect of phase mixing on a Lorentzian-shaped resonance feature. (a) True phase and absorption. (b) Measured absorption due to phase mixing, showing the resulting asymmetry and the shift of the maximum relative to the true absorption signal. The dotted horizontal lines represent the zero lines.

effect appeared in two different samples at the same frequency, it suggests that the observed signals do not originate from the sample itself but rather from instrumental or setup-related effects.

To investigate this possibility, additional measurements were performed without an inserted sample. A series of HF-EPR measurements was carried out over a narrow frequency interval for three different configurations: (i) an empty brass ring sealed with Kapton tape, (ii) an empty brass ring without Kapton tape, and (iii) a configuration without the brass ring and sample base (mirror part only).

Fig. 3.8(a) shows the HF-EPR transmission spectra at $T = 2$ K of an empty brass ring sealed with Kapton tape. For frequencies between 66.82 and 67.98 GHz, a minimum in the transmission at approximately 2.4 T can be observed. Below and above this narrow frequency interval (at 66.50 GHz and 68.99 GHz), the feature is no longer visible. The position of the resonance feature corresponds to a g-factor of $g \approx 2$. Overall, the spectral weight of this feature is relatively small, as indicated by the high signal-to-noise ratio.

Fig. 3.8(b) shows the transmission spectra at $T = 2$ K for an empty brass ring without Kapton tape. Here, a feature also appears only for frequencies above 66.50 GHz at the same field position. However, in this case the signal does not exhibit a

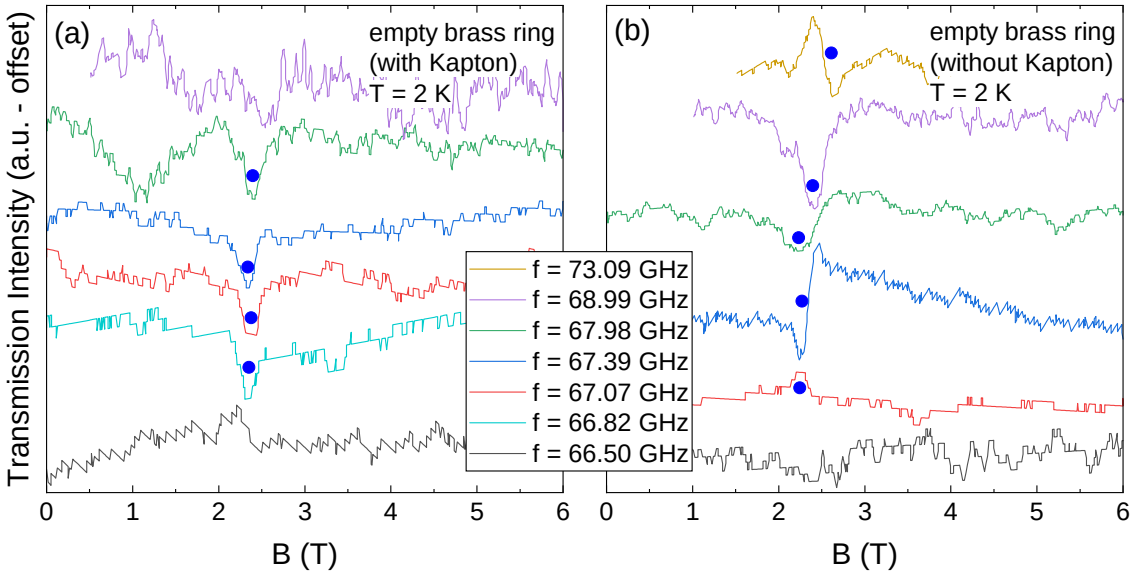


Figure 3.8: HF-EPR spectra at $T = 2$ K of (a) an empty brass ring sealed with Kapton tape for frequencies from 66.50 GHz to 68.99 GHz and (b) an empty brass ring without Kapton tape for frequencies from 66.50 GHz to 73.09 GHz. The blue dots indicate the observed resonance feature. All spectra are not phase-mixing-corrected, but corrected by a linear background and shifted along the ordinate.

symmetric minimum. Instead, it is more asymmetric or even shows a peak-like Maximum rather than a clear transmission minimum. The blue markers in fig. 3.8(b), therefore, do not represent the exact position of the feature, as it could often not be determined precisely, but are included as a guide to the eye. Transmission spectra of a configuration without the brass ring and sample base (mirror mount only) show no resonance features within the investigated frequency range. The comparison of the different configurations indicates that the observed resonance feature is related to the presence of the brass rings in the experimental setup.

The exact physical mechanism responsible for this resonance feature remains unclear. However, a simple order-of-magnitude estimate provides a possible explanation for its occurrence at this particular frequency: Converting the microwave frequency to the corresponding wavelength (67 GHz $\triangleq$ 4.47 mm) yields values that are on the same order as the characteristic dimensions of the brass ring (height = 2 mm). In particular, approximately half the wavelength is comparable to the height of the ring. This suggests that geometric resonance conditions associated with the ring structure could potentially contribute to the observed transmission features.

The signal of the background feature observed in the measurements is weak compared to the additional features appearing in the same frequency range when a sample is present. However, it cannot be excluded that the observed additional features is still related to the same setup-induced effect as identified in the empty configuration. Inserting a sample modifies the electromagnetic environment of the measurement

setup through its dielectric and magnetic properties. This can influence the microwave field and interference conditions. As a result, an initially weak instrumental feature may become amplified or exhibit a modified line shape when a sample is inserted. Therefore, the larger feature observed in the sample measurements may still originate from the same setup-related mechanism associated with the brass ring, even though its appearance differs from that seen in the empty measurement. Since the origin of the signal cannot be clearly determined, spectra recorded within this narrow frequency interval are interpreted with caution.

4 $Co^{II}Co^{III}_4$ complexes

Cobalt-containing molecular systems have developed into a major research field in physics and chemistry since the discovery of the first Co^{II} single-molecule magnet (SMM) in 2002 by Yang *et al.* [37, 38]. This is largely due to the fact that Co, among the 3*d* elements, exhibit relatively strong spin-orbit coupling which can give rise to large magnetic anisotropy. Consequently, the electronic and magnetic properties can be tuned by modifying the crystal field environment. The dominant contribution to the magnetic single-ion properties of molecular systems usually arises from the crystal field within the first coordination sphere, i.e., the ligands directly coordinated to the central metal ion. In this context, it has been shown that the anisotropy parameter D increases across a series of tetrahedral coordinated Co^{II} complexes containing different donor ions (O, S, Se) [39]. Since then, only few studies have focused on single-ion magnets based on 3*d* metal ions exclusively coordinated by oxygen ligands in a tetrahedral environment [40], and corresponding EPR studies of such systems are scare in the literature.

This chapter focuses on the analysis of the magnetic properties of a series of five $Co^{II}Co^{III}_4$ complexes. The complexes differ by variations in the para-substituted benzoic acid ligands, while the $Co^{II}Co^{III}_4$ core remains identical across the series [41]. Static magnetisation and dynamic susceptibility measurements were performed for all complexes. HF-EPR studies were carried out only for complex **(1)**. Therefore, the chapter begins with a detailed analysis of the measurements on **(1)**. The complexes are then compared with each another structurally and based on the magnetisation measurements, and the results are discussed in the context of the existing literature.

4.1 Analysis of complex (1)

4.1.1 Molecular Structure

The series of Co complexes was synthesised by Amit Gharu (Department of Chemical Sciences, IISER Mohali, India) and structurally characterised via single crystal X-ray diffraction, which was performed at IISER Mohali [41]. The magnetic investigation was performed on polycrystalline powder samples. Fig. 4.1(a) shows the molecular structure of $[Co^{II}Co^{III}_4(TEA)_4(N_3)_4(Bz)_2]$ **(1)**, which was investigated in this work.

The metal–organic complex consists of five distinct Co ions coordinated by organic ligands. The central Co^{II} ion is coordinated by four oxygen ions, forming a distorted tetrahedral environment, as shown in fig. 4.1(b). The four Co^{III} ions are each in a distorted octahedral coordination environment, consisting of two nitrogen and four oxygen ions. Fig. 4.1(c) shows the crystal packing of complex **(1)**. The crystallographic unit cell contains two molecular orientations, which are related by inversion symmetry.

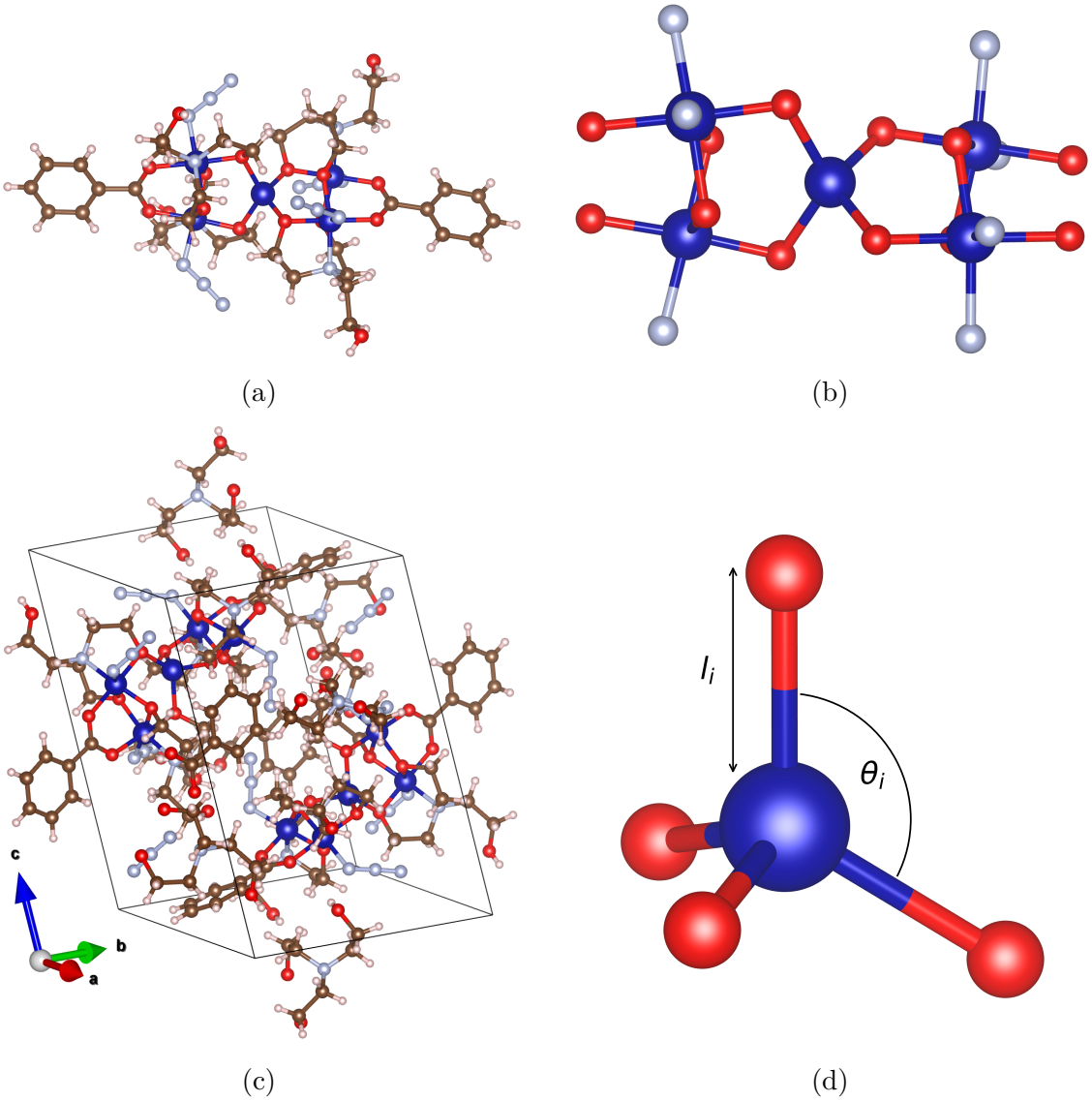


Figure 4.1: (a) Molecular structure, (b) first coordination sphere of the Co ions and (c) crystal packing of **(1)**. Colours: Co (blue), O (red), N (light blue), C (brown), H (rosa). Black lines indicate the unit cell. (d) First Coordination sphere of the central Co^{II} ion, showing the bond lengths l_i and bond angles θ_i. Data from [41]. Images were generated by VESTA [42].

4.1.2 Static Magnetisation and Susceptibility

For **(1)**, static magnetisation and susceptibility measurements were performed. The sample ($m = 8.93(4)$ mg, $M = 1292.67$ g/mol) was prepared in a capsule, fixed using Eicosane and mounted onto the brass sample holder (see section 3.1.2).

Fig. 4.2(a) shows the magnetic field dependence of the DC magnetisation of **(1)** at three different temperatures. At 1.8 K, the magnetisation increases steeply at low magnetic fields. With increasing field strength, the slope of the magnetisation decreases, and no saturation value is reached up to 7 T, which can be explained by

the magnetic anisotropy of the system. Comparing the measurements at 1.8 K, 3 K, and 5 K, the initial increase in magnetisation at low fields is more pronounced at lower temperatures. At higher magnetic fields, however, the curve recorded at 3.0 K approaches that measured at 1.8 K. A complete magnetisation loop at 1.8 K does not exhibit any hysteresis effects (see inset of fig. 4.2(a)).

Fig. 4.2(b) shows the temperature dependence of the DC magnetic susceptibility $\chi = M/B$ of **(1)**, plotted as χT and measured at two different magnetic fields. At low temperatures the χT-product exhibits a pronounced increase with increasing temperature. Above approximately 50 K, a linear behaviour is observed. At high temperatures the difference in the χT values obtained at the two applied magnetic fields is most likely attributable to the remanent field of the magnet (see section 3.1.6).

A Curie-like fit,

$$\chi = C/T + \chi_0, \tag{4.1}$$

was applied to the high-temperature data in the range 150 K $\leq T \leq$ 300 K (see tab 4.1), where C denotes the Curie constant and χ_0 a temperature-independent contribution.

From the crystal structure, it is concluded that the central Co^{II} ion in a distorted tetrahedral environment has a spin of $S = 3/2$. However, it remains unclear whether the Co^{III} ions in the distorted octahedral environment are in a high-spin ($S = 2$)

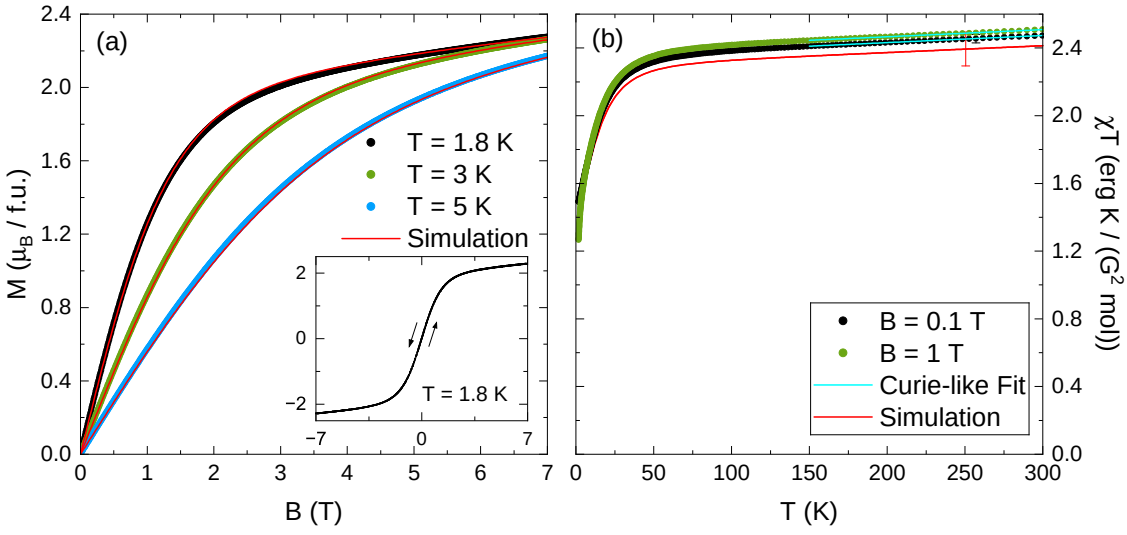


Figure 4.2: (a) Magnetic field dependence of the DC magnetisation of **(1)** measured at three different temperatures. Inset: complete magnetisation loop at $T = 1.8$ K. (b) Temperature dependence of the DC magnetic susceptibility $\chi = M/B$ of **(1)** plotted as χT measured at two different magnetic fields. Cyan solid lines represents a Curie-like Fit to the high-temperature data, as described in the text. Red solid lines represents simulations to the data, as discussed later in the text.

(1)	C (erg K/(G^{2}mol))	χ_0 (erg/(G^{2}mol))
$B = 0.1$ T	2.35(2)	$4.19(4) \cdot 10^{-4}$
$B = 1$ T	2.38(2)	$4.20(4) \cdot 10^{-4}$

Table 4.1: Parameters of the Curie-like fit $\chi T = C + \chi_0 T$ to **(1)** at high temperatures.

or low-spin ($S = 0$) state. Assuming a low-spin configuration for the Co^{III} ions, these would be diamagnetic, and the magnetic properties of the complex would be essentially determined by the central Co^{II} ion. Using

$$C = \frac{N_A \mu_B^2 g^2 S(S+1)}{3k_B}, \tag{4.2}$$

an isotropic g-factor of $g = 2.25(2)$ is derived for $S = 3/2$. This value is higher than the spin-only value, reflecting the influence of spin–orbit coupling and indicating imperfect quenching of the orbital moment. Notably, two closely related complexes reported in [43], featuring an analogous $Co^{II}Co^{III}_4$ core structure, were also found to exhibit low-spin Co^{III} ions, further supporting this assignment. Including a Weiss temperature Θ to the fit to account for possible intermolecular interactions yields $\Theta \simeq 0$ K, indicating negligible magnetic coupling between the molecules. Consequently, the Curie law provides an adequate description of the paramagnetic response at high temperatures.

The temperature-independent susceptibility term χ_0 accounts for several contributions, including the background of the capsule in the brass sample holder, the diamagnetism of the ions, the Van Vleck paramagnetism of the cobalt ions, and the diamagnetic contribution of the Eicosane.

4.1.3 HF-EPR Studies

HF-EPR spectra of complex **(1)** were measured on a randomly oriented, fixed powder sample prepared as described in section 3.2.2. This allows for the determination of the individual components of the g-tensor. Fig. 4.3 shows the transmission spectra at $T = 2$ K for different frequencies up to $f = 320.4$ GHz. A broad resonance feature is observed at all frequencies. A transmission minimum is visible, along with a broad shoulder at higher magnetic fields. This feature becomes broader with increasing frequency. A second, weak resonance feature (blue dot) is visible for frequencies from 197.7 GHz to 320.4 GHz. At lower frequencies, it is likely obscured by the broad main resonance feature. Its frequency-field dependence implies a g-factor of approximately $g \approx 2$ with a zero-field splitting (ZFS) of 7.5 GHz. The overall line shape of the main resonance feature indicates easy-plane anisotropy ($D > 0$), while the width of the powder spectrum reflects the anisotropy of the g-tensor. Due to the broad resonance feature, a phase-mixing-correction of the spectra was not possible, and the spectra were only background-corrected as described in section 3.2.3.

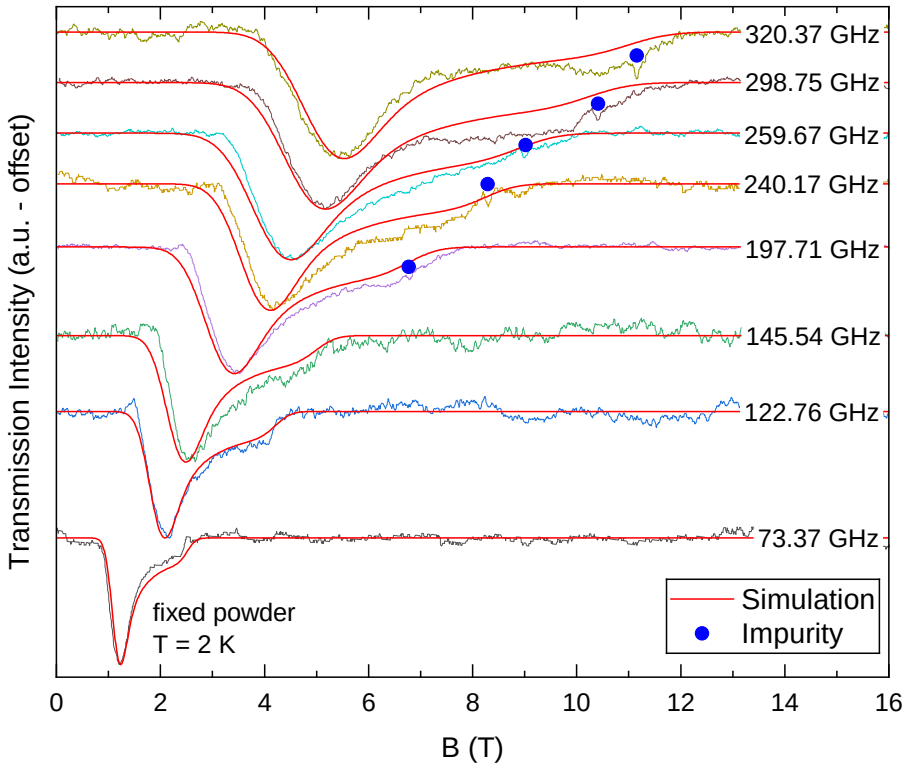


Figure 4.3: HF-EPR spectra of a fixed powder sample of **(1)** measured at 2 K and varying frequencies from 73.4 to 320.4 GHz. Red curves show simulations of the spectra as described in the text. All spectra are background-corrected, normalised to the absolute of the lowest value and shifted along the ordinate. The spectra could not be phase-mixing-corrected.

Fig. 4.4 shows the transmission spectra at $f = 298.75$ GHz for temperatures ranging from 2 to 40 K. The pronounced main resonance feature decrease in intensity with increasing temperature, indicating that it originates from a transition involving the ground state. The second, weak resonance feature is visible at all temperatures and shows only a slight decrease in intensity.

All HF-EPR spectra, as well as the DC magnetisation and magnetic susceptibility, are simulated according to the Spin-Hamiltonian

$$\hat{\mathcal{H}} = D\left(\hat{S}_z^2 - \frac{S(S+1)}{3}\right) + \mu_B \boldsymbol{B} \overleftrightarrow{g} \hat{\boldsymbol{S}} \qquad \text{with} \qquad \overleftrightarrow{g} = \begin{pmatrix} g_\perp & 0 & 0 \\ 0 & g_\perp & 0 \\ 0 & 0 & g_\parallel \end{pmatrix}. \tag{4.3}$$

For the simulations of the magnetisation measurements, an additional temperature-independent contribution χ_0 was included. Tab. 4.2 shows the best set of parameters for the combined simulations using $S = 3/2$. The simulations are displayed as solid red lines in figs. 4.2 to 4.4. Since only an isotropic g-factor can be extracted from the magnetisation data, the anisotropy of the g-tensor was determined by the HF-EPR measurements. In the HF-EPR spectra, the position of the transmission minimum is

primarily given by $g_\perp$, whereas the position of the broad shoulder is governed by $g_\parallel$. For $D \geq 300$ GHz, the HF-EPR spectra are relatively insensitive to the precise value of D. Fig. 4.5 shows simulations for different values of D at 122.76 GHz and 2 K. Only minor differences are observed between simulations using $D = 300$ GHz and, for example, $D = 840$ GHz. We adopted $D = 580$ GHz because this value provides the best agreement with the magnetisation measurements.

The rather large uncertainty in D arises from the range of simulations that provide equally good agreement with the experimental magnetisation data within the uncertainty of the g-factor. Including a transverse anisotropy parameter E did not considerably improve the simulations and was hence neglected to avoid overparameterisation. The simulations of the DC magnetisation data and the HF-EPR

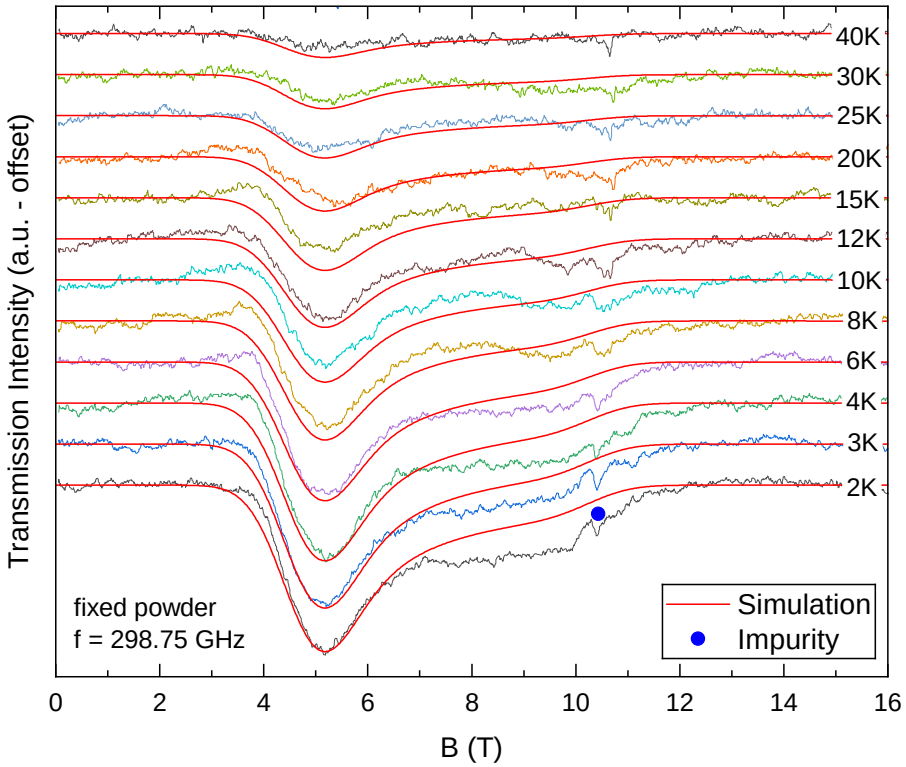


Figure 4.4: HF-EPR spectra of a fixed powder sample of **(1)** measured at 298.75 GHz for temperatures from 2 to 40 K. Red curves show simulations of the spectra as described in the text. All spectra are background-corrected and shifted along the ordinate. The spectra could not be phase-mixing-corrected.

$g_\perp$	$g_\parallel$	D (GHz)	χ_0 (erg/(G^{2}mol))
2.27(5)	2.07(5)	580(150)	$4.2{\cdot}10^{-4}$

Table 4.2: Axial anisotropy parameter D and directional g-factors obtained from simulating the HF-EPR spectra and magnetisation measurements of **(1)** using the Hamiltonian 4.3. χ_0 was included in the simulations of the magnetisation data.

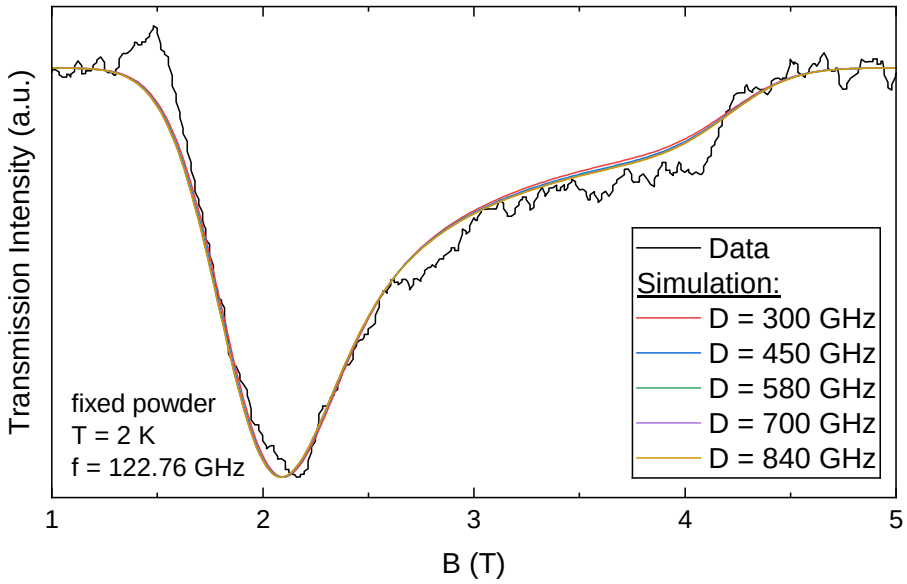


Figure 4.5: HF-EPR spectra of a fixed powder sample of **(1)** measured at 122.76 GHz and 2 K (black curve). Coloured curves show simulations for different values of D as described in the text. Experimental data is background-corrected; no phase-mixing-correction was possible.

spectra show good agreement with the experimental results. The simulated χT-product reproduces the experimental data well for temperatures $T \leq 20$ K. At higher temperatures, the simulation slightly underestimates the measured values. The isotropic g-factor expected from the g-tensor yields $g^{\text{iso}} = 2.20(5)$. Considering the uncertainties in the simulation parameters, the results are still consistent with the experimental data.

Ab-initio CASSCF calculations, performed for complex **(1)** by Amit Gharu, predict easy-plan anisotropy with $D^{\text{CASSCF}} = 840$ GHz, which is slightly larger than the value $D^{\text{Sim}} = 580(150)$ GHz obtained from the best simulation. Such deviations are not uncommon for *ab-initio* calculations.

4.1.4 Dynamic Susceptibility

The magnetic response of complex **(1)** to an oscillating external magnetic field was analysed in two different static fields. No slow magnetic relaxation is observed at $B_{\text{dc}} = 0$ T. In contrast, at $B_{\text{dc}} = 0.1$ T, slow magnetic relaxation is clearly visible. The frequency dependence of the out-of-phase component of the AC susceptibility is shown in fig. 4.6(a) for various temperatures. Two peaks of significantly different intensity can be observed for low temperatures. The maximum in χ'' corresponds to the dominant relaxation pathway, while a much weaker secondary, slower relaxation can be detected at lower frequencies. This secondary pathway is most clearly visible in the Cole-Cole plot (see fig. 4.6(c)), where a second feature appears at lower values of χ'' in addition to the pronounced semicircle. The main peak, which is observable

at low temperatures and high frequencies shifts to higher frequencies with increasing temperature and is fully visible up to 2.29 K.

The out-of-phase component, χ'', was fit using a generalised double-Debye function (each described by eq. (2.27)) for temperatures up to 2.29 K. At higher temperatures, a generalised single Debye function (see eq. (2.27)) was fit, as the double-Debye fit no longer adequately accounts for the weak, slower relaxation. The larger deviation of the fit from the experimental data at higher temperatures arises because the fitting procedure cannot reliably determine the position of the maximum when the relaxation times exceed the measurable frequency range.

The relaxation times associated with the main peak of χ'', obtained from the fits at different temperatures are presented in an Arrhenius plot in fig. 4.7. The

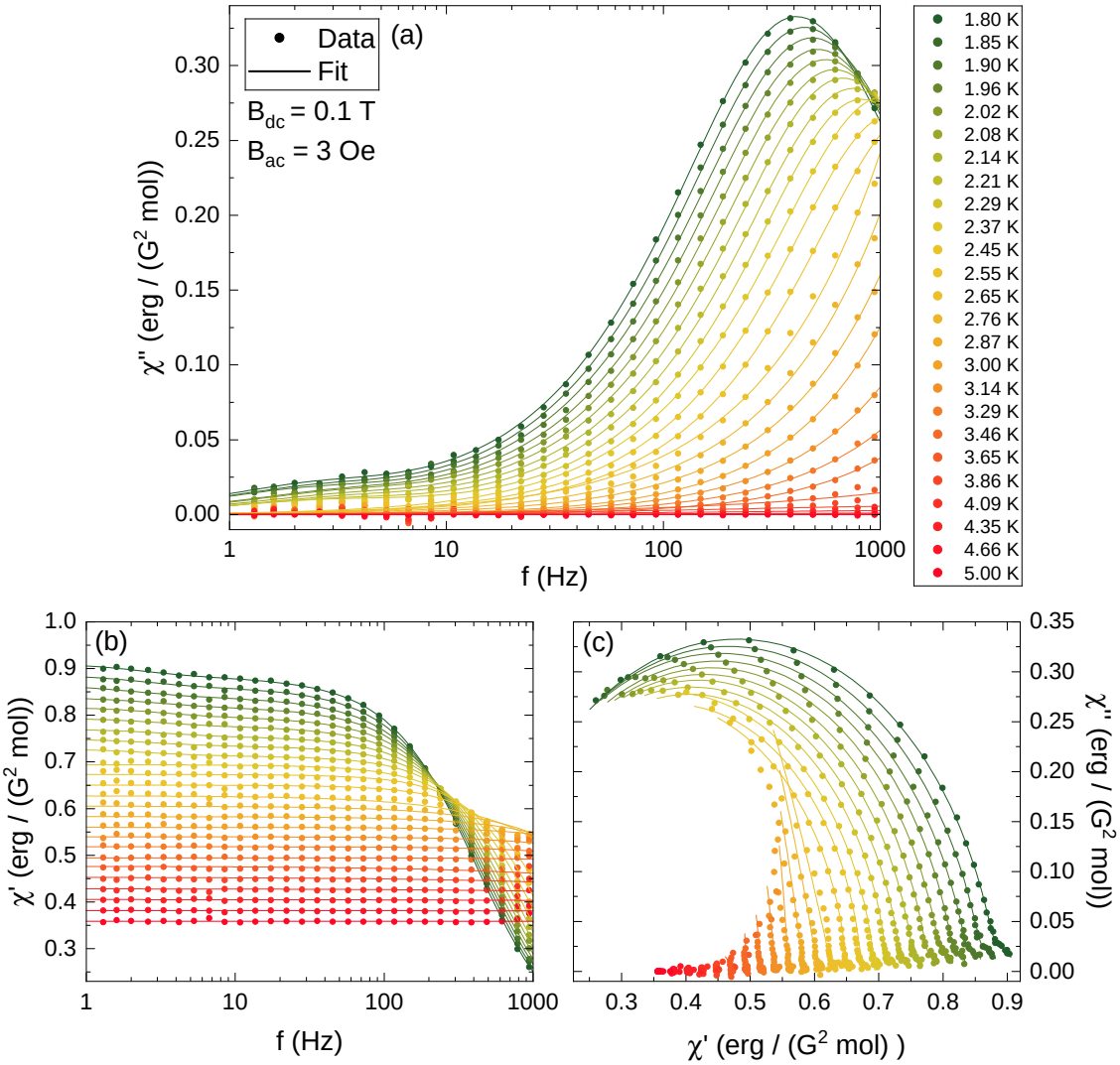


Figure 4.6: Frequency dependence of the out-of-phase (a) and in-phase (b) component of the AC susceptibility and Cole-Cole plot (c) of **(1)** measured by applying an AC magnetic field of 3 Oe and a static magnetic field of 0.1 T. The data was collected at various temperatures ranging from 1.8 K to 5. K. Solid lines depict fits to the data as described in the text.

uncertainties were estimated by varying the fit parameters until the experimental data were no longer adequately described by the fitting function. The data exhibit an approximately linear behaviour, indicating that the temperature dependence of τ can be well described by an exponential relation. Since only a limited temperature range was investigated, it is likely that the high-temperature Orbach dominated regime is not fully reached (see the comparison with complexes **(2)** - **(5)** in section 4.2). Measurements to higher frequencies would be required to confirm this behaviour. Using

$$\tau(T) = \tilde{\tau}_0 \, e^{(\Delta/k_B T)}, \tag{4.4}$$

as a fitting equation results in the fit parameters: $\Delta = 5.6(4)$ K and $\tilde{\tau}_0 = 1.1(2)\cdot 10^{-4}$ s. In principle, it is surprising, that complex **(1)** shows single-molecule magnet (SMM) behaviour. In case of easy-axis anisotropy, a transition between $M_S = +S$ and $M_S = -S$ requires excitation over an effective energy barrier. For easy-plane anisotropy ($D > 0$), the ground state doublet corresponds to $M_S = \pm 1/2$, resulting in a maximal spin projection onto the xy plane. In the case of purely axial symmetry, the spin has no preferred direction within this plane and does not experience an energy barrier. Introducing a transverse anisotropy term of the form $E(\hat{S}_x^2 - \hat{S}_y^2)$,

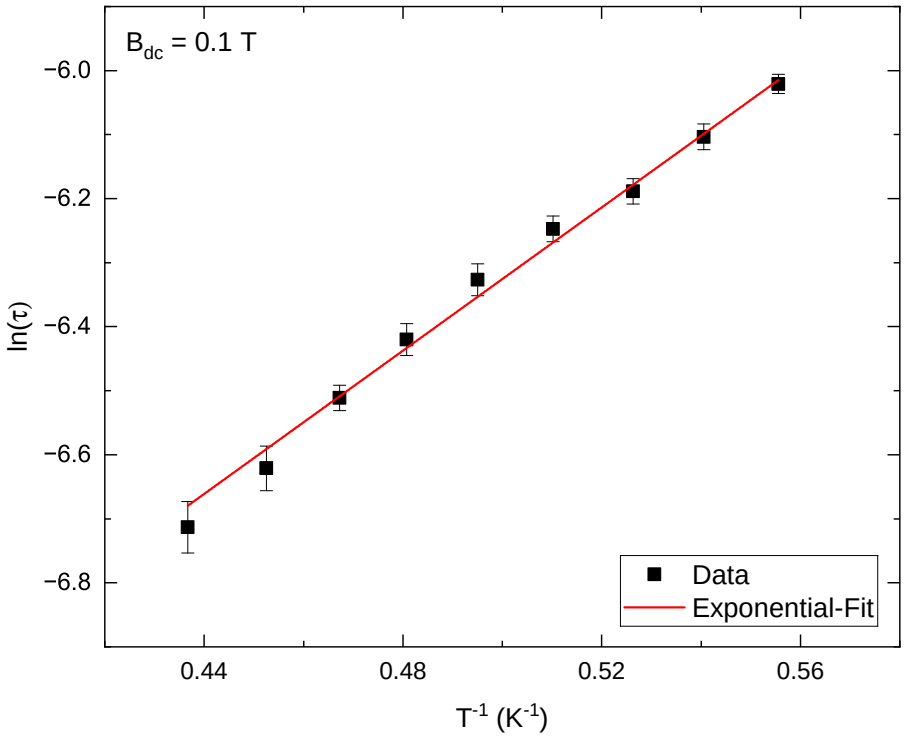


Figure 4.7: Arrhenius plot of the relaxation times associated with the main peak of χ'', extracted from fits to the out-of-phase component of the AC magnetic susceptibility measured under a static magnetic field of 0.1 T, as described in the text. The red solid line represents an exponential fit to the data, as discussed in the text.

however, creates a preferred axis along either the x or y direction, depending on the sign of E. This gives rise to an effective energy barrier within the xy plane that hinders transitions between $+x$ and $-x$ (or $+y$ and $-y$) [44, 45]. Unfortunately, the transverse anisotropy parameter E could not be determined from either the static magnetisation or the HF-EPR measurements.

4.2 Analysis of complexes (2) - (5)

The series of complexes **(1)** - **(5)** is designed based on varying the para-substituted benzoic acid ligands while maintaining an identical $Co^{II}Co^{III}_4$ core across all complexes [41]. The individual para-substituted benzoic acid ligands are shown in fig. 4.8.

The different ligands induce variations in the tetrahedral distortion across the series due to changes in bond lengths and bond angles. To quantify these distortions, we define the bond angle variance, σ^2_θ, and the quadratic elongation, $\langle\lambda\rangle$, [46] as

$$\sigma^2_\theta = \frac{1}{6}\sum_{i=1}^{6}(\theta_i - 109.5°)^2 \qquad \text{and} \qquad \langle\lambda\rangle = \frac{1}{6}\sum_{i=1}^{6}(\frac{l_i}{l_0})^2, \tag{4.5}$$

where θ_i and l_i are the bond angles and bond lengths within the distorted tetrahedron, as illustrated in fig. 4.1(d). Values of $\sigma^2_\theta = 0$ and $\langle\lambda\rangle = 1$ correspond to a perfect tetrahedron. Here, l_0 denotes the center-to-ligand distance of a regular tetrahedron whose volume equals that of the distorted tetrahedron with bond lengths l_i. The bond angle variance and quadratic elongation for the different complexes are summarized in tab 4.3.

It can be seen that the tetrahedral distortion slightly decreases from **(1)** to **(5)**. Considering the bond angles in detail, each complex exhibits two angles with $\theta > 120°$, which are larger than the ideal tetrahedral angle, and four angles below the ideal value.

To compare the series of Co complexes in terms of their magnetic properties and to assess the impact of the different bond angles and bond lengths, magnetisation measurements were performed on all samples. The corresponding sample masses and molar masses are summarised in tab 4.3.

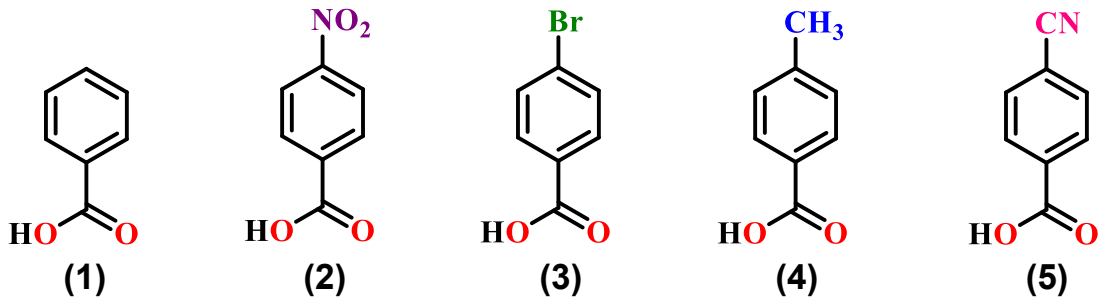


Figure 4.8: Para-substituted benzoic acid ligands of **(1)** - **(5)** [41].

	ligands	σ^2_θ	$\langle\lambda\rangle$	molar mass	sample mass
(1)	$(Bz)_2$	107.5	1.0363	$M = 1292.67$ g/mol	$m = 8.93(4)$ mg
(2)	$(No_2Bz)_2$	105.8	1.0357	$M = 1215$ g/mol	$m = 8.47(5)$ mg
(3)	$(BrBz)_2$	101.6	1.0343	$M = 1450.48$ g/mol	$m = 10.55(4)$ mg
(4)	$(p\text{-}mBz)_2$	98.7	1.0330	$M = 1320.72$ g/mol	$m = 11.67(5)$ mg
(5)	$(CNBz)_2$	93.7	1.0315	$M = 1342.68$ g/mol	$m = 11.75(6)$ mg

Table 4.3: Summary of the various structural parameters [41] and sample mass for complexes **(1)** - **(5)**.

4.2.1 Static Magnetisation and Susceptibility

Fig. 4.9 shows the magnetic field dependence of the DC magnetisation and the temperature dependence of the magnetic susceptibility, $\chi = M/B$, plotted as χT, for complexes **(2)** - **(4)**. All three complexes exhibit the same general magnetic behaviour as **(1)**. Notably, **(2)** shows a pronounced difference in the χT-product between measurements at different magnetic fields with respect to the linear increase at high temperatures. A Curie-like fit according to eq. (4.1) to the high-temperature data yields $\chi_0 = 1.41(2) \cdot 10^{-5}$ (erg/(G^{2}mol)) for $B = 0.1$ T and $\chi_0 = 3.42(3) \cdot 10^{-4}$ (erg/(G^2 mol)) for $B = 1$ T. The small jump in the χT-product for **(3)** at approximately 260 K (marked by the asterisk) is most likely due to an internal recalibration of the instrument during the measurement.

To better illustrate the differences in the magnetisation measurements, fig. 4.10(a) shows the DC magnetisation for **(1)** - **(4)** measured at $T = 1.8$ K in the same plot. It can be seen that **(3)** and **(4)** exhibit slightly higher magnetisation values over the whole field range (approximately 3% for **(3)** and 2% for **(4)** at $B = 7$ T) compared to **(1)** and **(2)**. This may be attributed to a slightly smaller magnetic anisotropy. In addition, the stronger curvature of **(1)** at intermediate fields compared to **(2)** may also be attributed to a slightly higher value of D.

Fig. 4.10(b) displays the temperature dependence of the susceptibility, plotted as $(\chi - \chi_0)\,T$, for **(1)** - **(4)** at $B = 1$ T. Except for the previously mentioned jump for **(3)**, the curves for all complexes show a very similar behaviour. Starting from low temperatures, **(4)** approaches the high-temperature plateau slightly faster than **(2)** and **(3)**, while **(1)** reaches the plateau at slightly higher temperatures. This suggests a slightly stronger magnetic anisotropy for **(1)**, which is in agreement with the trend observed in the isothermal magnetisation measurements.

To quantitatively compare the anisotropy of the different complexes, the magnetisation data of **(2)** - **(4)** were fit using only an isotropic g-factor and an easy-plane anisotropy ($D > 0$). However, this approach does not yield satisfactory results, indicating that either the g-tensor anisotropy or a transverse anisotropy term E cannot be fully neglected.

As for **(5)**, the DC magnetisation shown in fig. 4.10(c) exhibits a different behaviour. The isothermal magnetisation does not fully saturate up to $B = 7$ T. At $B = 7$ T, it reaches $M = 3.35\ \mu_B$/f.u. for 1.8 K, which is significantly larger than for the other complexes (see tab 4.4). At small fields ($B \simeq 0.3$ T, indicated by the black arrow), a slight change in curvature is visible in the differential magnetic susceptibility (orange open dots). A quasi-linear region is also observed between 3 T and 4.5 T visible, culminating in a small hump at $B_C \simeq 4.5$ T before further saturating. This behaviour could be indicative of antiferromagnetic intermolecular coupling. Additionally, the χT-product at high temperatures (see fig. 4.10(d)) is much higher than for the other complexes, which implies an isotropic g-factor of $g = 2.73(1)$.

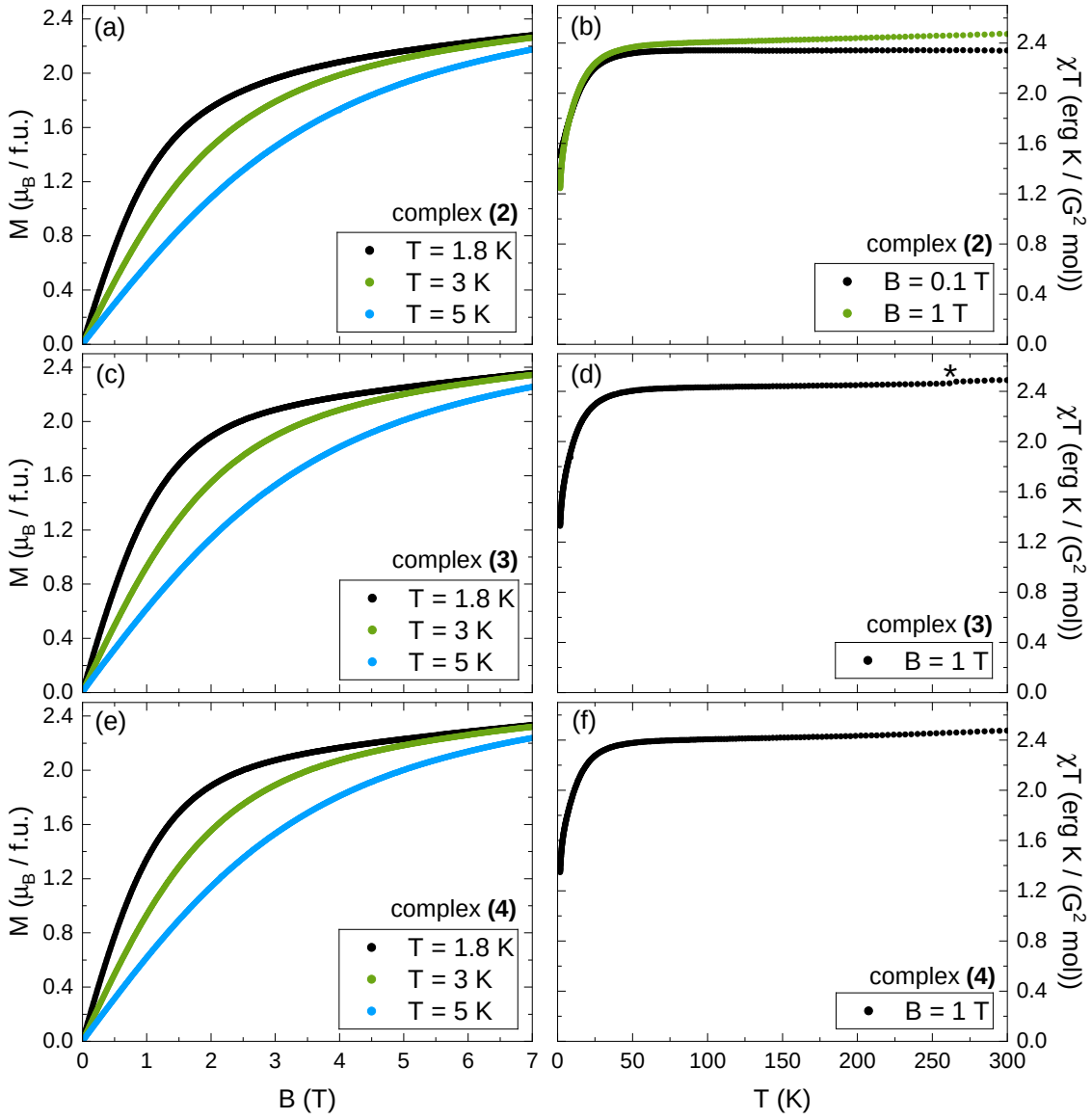


Figure 4.9: (a), (c) and (e) Magnetic field dependence of the DC magnetisation of **(2)**, **(3)** and **(4)** measured at three different temperatures. (b), (d) and (f) Temperature dependence of the DC magnetic susceptibility $\chi = M/B$ of **(2)**, **(3)** and **(4)** plotted as χT.

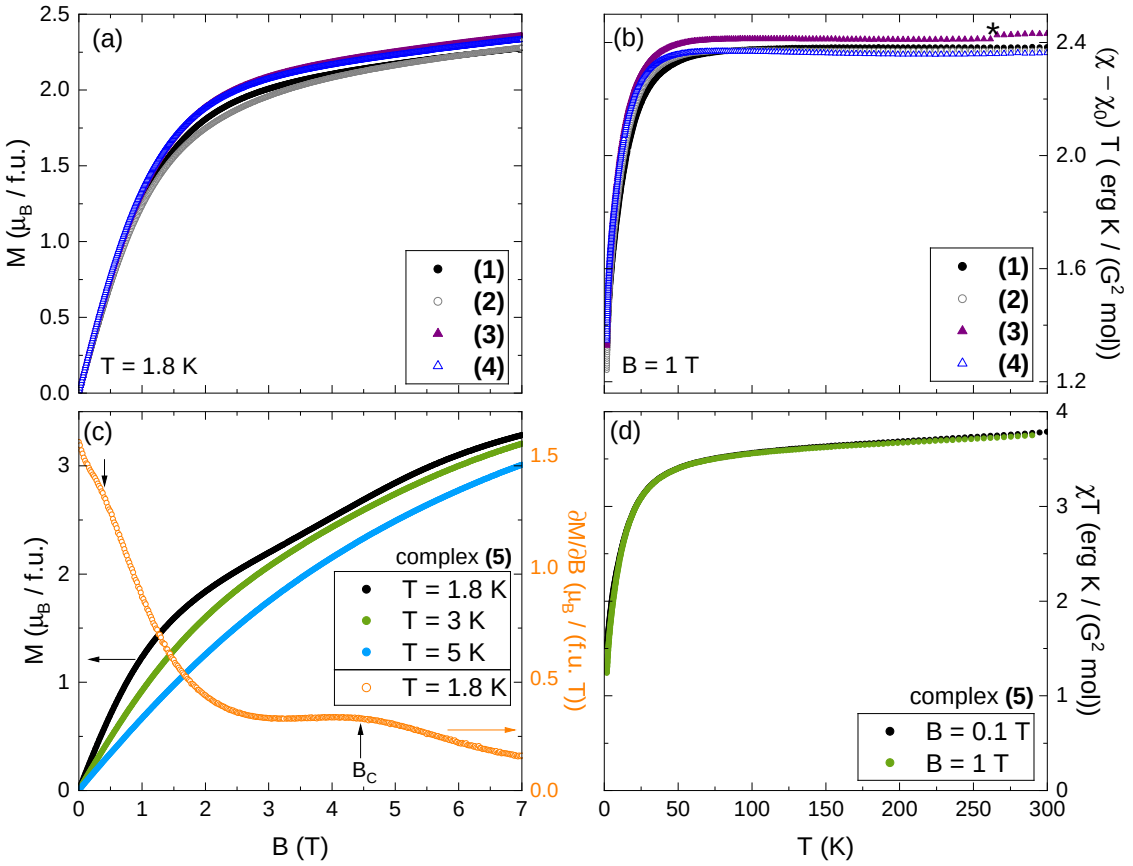


Figure 4.10: (a) Magnetic field dependence of the DC magnetisation of **(1)** - **(4)** measured at $T = 1.8$ K. (b) Temperature dependence of the DC magnetic susceptibility $\chi = M/B$ of **(1)** - **(4)** plotted as χT for $B = 1$ T. (c) Magnetic field dependence of the DC magnetisation of **(5)** measured at three different temperatures (left axis) and the derivative $\partial M/\partial B$ at $T = 1.8$ K (right axis). (b) Temperature dependence of the DC magnetic susceptibility $\chi = M/B$ of **(5)** plotted as χT measured at two different magnetic fields.

	g_{SQUID}[a]	$M(1.8\ K, 7\ T)$ (μ_B/f.u.)	Δ (K)	$\tilde{\tau}_0$ (10^{-4} s)	χ_0 (10^{-4} erg/(G^{2}mol)) $B_0 = 0.1$ T	$B_0 = 1$ T
(1)	2.25(2)	2.28(2)	5.6(4)	1.1(2)	4.19(4)	4.20(4)
(2)	2.24(2)	2.28(3)	4.6(8)	1.2(5)	0.141(2)	3.42(3)
(3)	2.26(2)	2.36(2)	4.8(19)	5.2(9)	-	1.95(8)
(4)	2.24(2)	2.33(2)	6.0(5)	2.2(7)	-	3.8(5)
(5)	2.73(1)[b]	3.28(4)[b]	4.9(8)	1.6(5)	9.78(9)	8.67(8)

[a] Derived from the Curie constant C by assuming $S = 3/2$.
[b] Note: the $M(B)$ curve for **(5)** deviates significantly from the others.

Table 4.4: Summary of the various magnetic parameters for complexes **(1)** - **(5)**.

4.2.2 Dynamic Susceptibility

The AC data show slight differences across the series of complexes. The frequency dependence of the out-of-phase component of the AC susceptibility is presented in fig. 4.11 for various temperatures. For **(3)** and **(5)**, the measured data could not be adequately described using neither a generalised Debye nor a generalised double-Debye function. To extract the characteristic relaxation times, a generalised Debye function was fitted to a small frequency interval around the maximum for temperatures up to 2.76 K for **(3)** and up to 2.14 K for **(5)**. In addition, the maximum of χ'' for **(3)** and **(4)** remains visible at higher temperatures within the investigated frequency range compared to the other complexes.

The relaxation times, τ, obtained from the fits of χ'' at different temperatures are presented in Arrhenius plots in fig. 4.12. All complexes exhibit a linear behaviour at low temperatures. Since the maximum of χ'' for **(3)** and **(4)** could be determined at higher temperatures, deviations from linearity become apparent at elevated temperatures. For **(3)** and **(4)**, eq. (2.31) was used to fit the data. The fit results

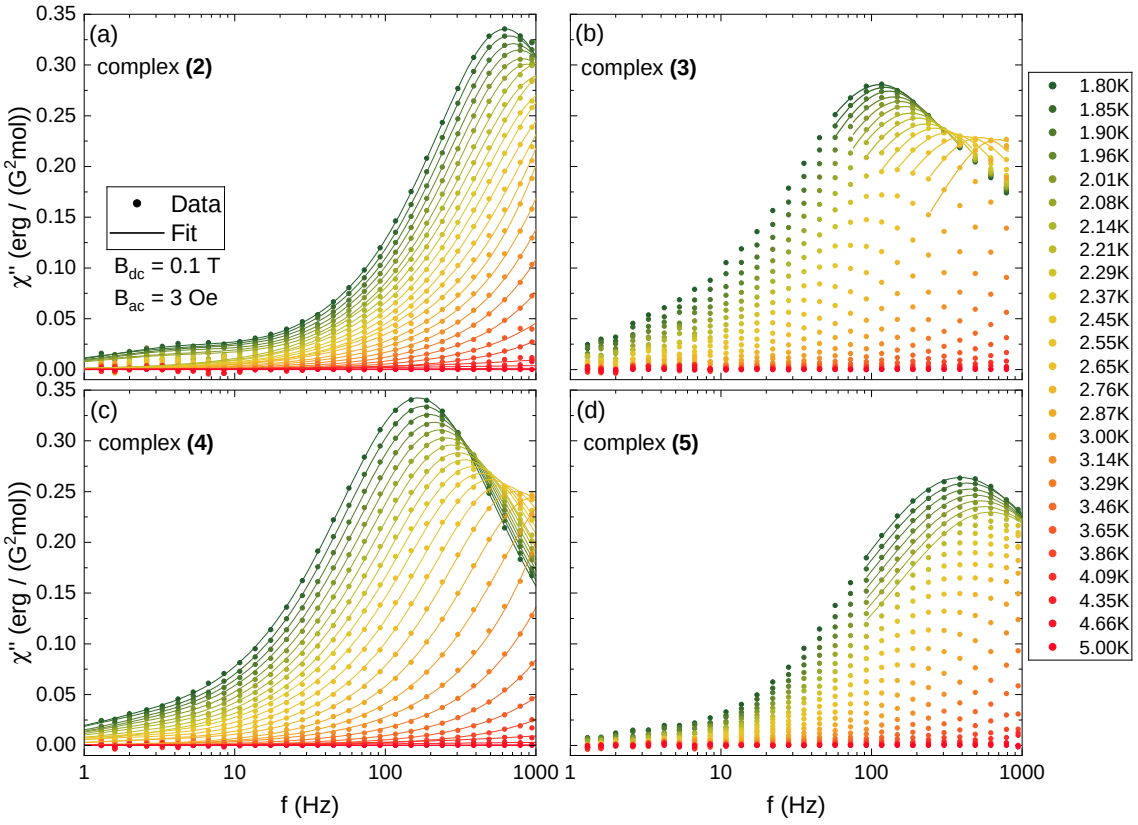


Figure 4.11: (a) - (d) Frequency dependence of the out-of-phase component of the AC susceptibility of **(2)** - **(5)**, measured by applying an AC magnetic field of 3 Oe and a static magnetic field of 0.1 T. The data was collected at various temperatures ranging from 1.80 K to 5.00 K. Solid lines (blue solid lines) depict fits to the data in (a) and (c) ((b) and (d)) as described in the text.

in both the QTM and the direct processes being set to zero. The data can be well described by a combination of Orbach and Raman relaxation. However, due to the limited temperature range and strong correlation between the fitting parameters, the extracted values are not uniquely determined. The corresponding curves are, therefore, shown only as guides to the eye and are not used for quantitative comparison. A Orbach-Fit (see eq. (2.29)) to the high-temperature regime of **(3)** and **(4)** yields effective energy barriers of $U_{\text{eff}} = 16(3)$ K and $U_{\text{eff}} = 13(2)$ K, respectively.

To allow for a comparison across all complexes, an exponential fit (see eq. (4.4)) was performed for each compound in the linear low-temperature regime. The resulting fit parameters are summarized in tab 4.4. All complexes exhibit similarly high effective energy barries Δ, ranging from 4.6 K to 6 K. The pre-exponential factor, $\tilde{\tau}_0$, is also of the same order of magnitude for all complexes.

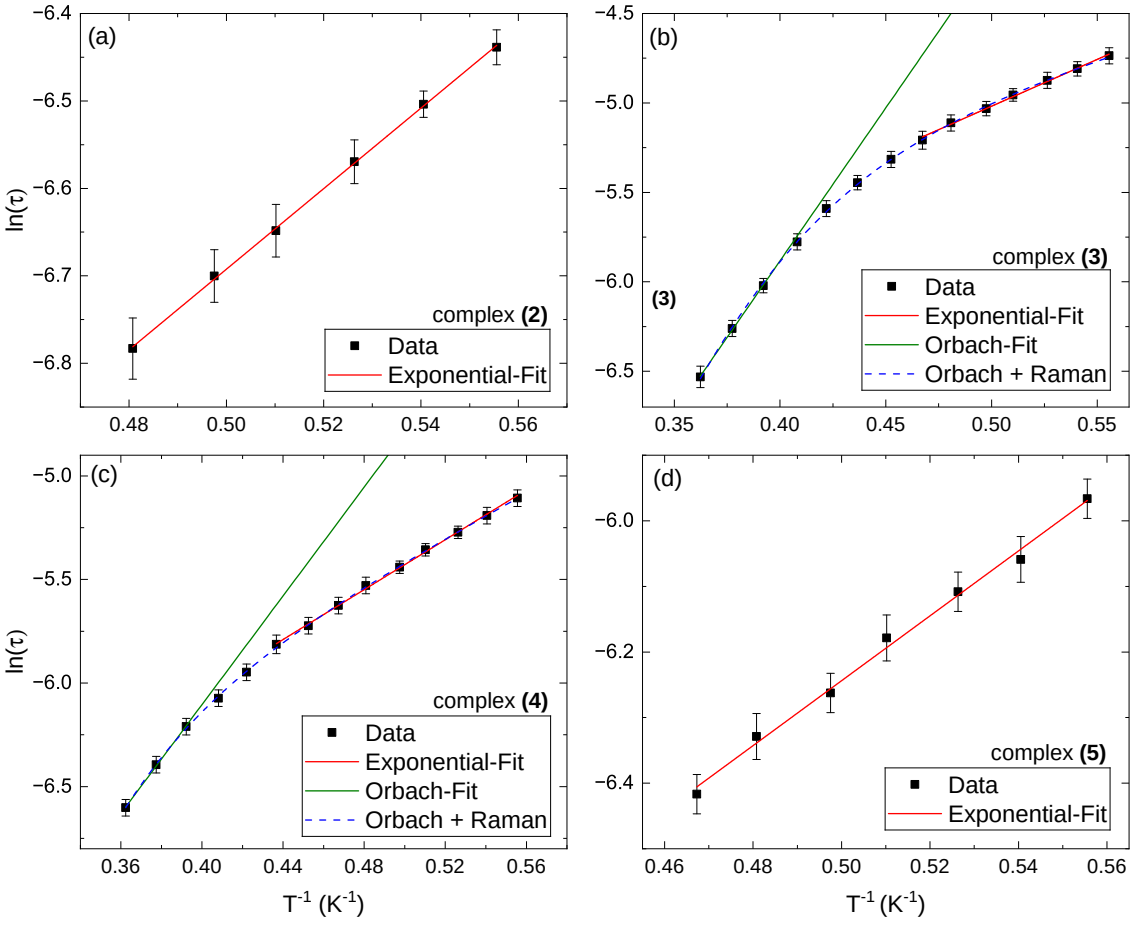


Figure 4.12: (a) - (d) Arrhenius plot of the relaxation time τ of **(2)** - **(5)** extracted from fits to the out-of-phase component of the AC magnetic susceptibility. The red solid lines represents exponential fits to the data at low temperatures. The green solid lines represents Orbach fits to the high-temperature data for **(3)** and **(4)**. Blue dashed lines represents a combined simulation of Orbach and Raman relaxation (non-unique parameters), as discussed in the text.

4.3 Comparison between (1) - (5) and Discussion

From the magnetisation measurements, only small deviations in the DC magnetisation and susceptibility are observed between **(1)** - **(5)**. A qualitative analysis of the magnetisation data suggests a gradual decrease of the magnetic anisotropy across the series from complex **(1)** to **(4)**, while **(3)** and **(4)** exhibit very similar magnetic anisotropy. This trend is in good agreement with the structural evolution of the distorted tetrahedral coordination environment of the Co^{II} ion, where the degree of distortion decreases from **(1)** to **(5)** (see tab 4.3). However, the differences observed in the magnetisation behaviour are quite small, and it remains difficult to identify a clear quantitative trend. In contrast, **(5)** exhibits a completely different magnetisation behaviour and is therefore not directly comparable within this series.

It should be noted, however, that focusing only on the first coordination sphere represents a simplification. Contributions from the extended coordination environment where shown to also have a significant impact on the magnetic anisotropy and overall magnetic behaviour [47, 48]. Therefore, while the observed trend correlates with changes in the first coordination sphere, additional structural factors are likely to play also a role.

A comparison with related Co^{II} systems reported in the literature provides valuable context for the present results. In particular, the magnetic anisotropy can be compared to values reported for tetrahedrally coordinated Co^{II} complexes with oxygen donor ligands. Notably, for these systems, no EPR studies have been reported so far, and the available anisotropy parameters are therefore derived exclusively from magnetisation measurements.

In Ref. [43], two Co^{II} complexes featuring an analogous $Co^{II}Co^{III}_4$ core structure, similar to **(1)** – **(5)**, were analysed, and the magnetisation data exhibit comparable behaviour. However, the anisotropy parameter D was only obtained from calculations. *Ab initio* CASSCF calculations indicate easy-axis anisotropy with values in the range $-1055\ \text{GHz} \leq D \leq -752\ \text{GHz}$.

Other reported systems with exclusively oxygen donor ligands also predominantly exhibit easy-axis anisotropy [39, 49]. In particular, Ref. [40] reports $D = -2227$ GHz, corresponding to the largest magnetic anisotropy reported so far for a $3d$-metal-based single-ion magnet with purely oxygen donors in the first coordination sphere. In contrast, Ref. [49] also describes complexes with comparatively small easy-plane anisotropy ($120\ \text{GHz} \leq D \leq 495\ \text{GHz}$).

With respect to the dynamic magnetic properties, AC susceptibility measurements reveal that slow magnetic relaxation is, in most cases, only observed under an applied static magnetic field for both easy-axis and easy-plane systems [39, 43, 49]. In contrast, Ref. [40] reports slow magnetic relaxation in zero field, with a comparatively large effective energy barrier of $U_{\text{eff}} = 125$ K.

5 $Cu_5^{II}Ln^{III}$ Metallacrowns

Since their discovery in 1989, metallacrowns have developed into a significant field of research. Their structure is based on the repetition of metal–nitrogen–oxygen ($[M–N–O]_n$) units, which form a ring [50]. This geometry gives rise to interesting magnetic properties, including the potential for single-molecule magnetism [51]. A subclass within this family is the 15-metallacrown-5 (15-MC-5) architecture, in which a pentagonal ring of five transition metal ions coordinates a single central ion [52].

In this chapter, three chiral $Cu_5^{II}Ln^{III}$ 15-MC-5 metallacrowns are investigated with respect to their magnetic properties using magnetisation measurements and HF-EPR spectroscopy. The three complexes differ with respect to the central Ln^{III} ion, with Ln = Y, Gd, or Dy, while the Cu^{II} pentameric ring and the ligand environment remain essentially unchanged.

5.1 Molecular Structure

The three investigated complexes, $[Ln[15\text{-}MC_{Cu(II)N(\text{-}THIQHA)}\text{-}5](NO_3)_3(H_2O]$ with Ln = Y, Gd, or Dy, were synthesised and structurally characterised in the group of Prof. Eva Rentschler at Mainz University. The first complex, $\mathbf{(1_Y)}$, contains a diamagnetic Y^{III} ion; the second, $\mathbf{(2_{Gd})}$, a paramagnetic Gd^{III} ion; and the third, $\mathbf{(3_{Dy})}$, a paramagnetic Dy^{III} ion.

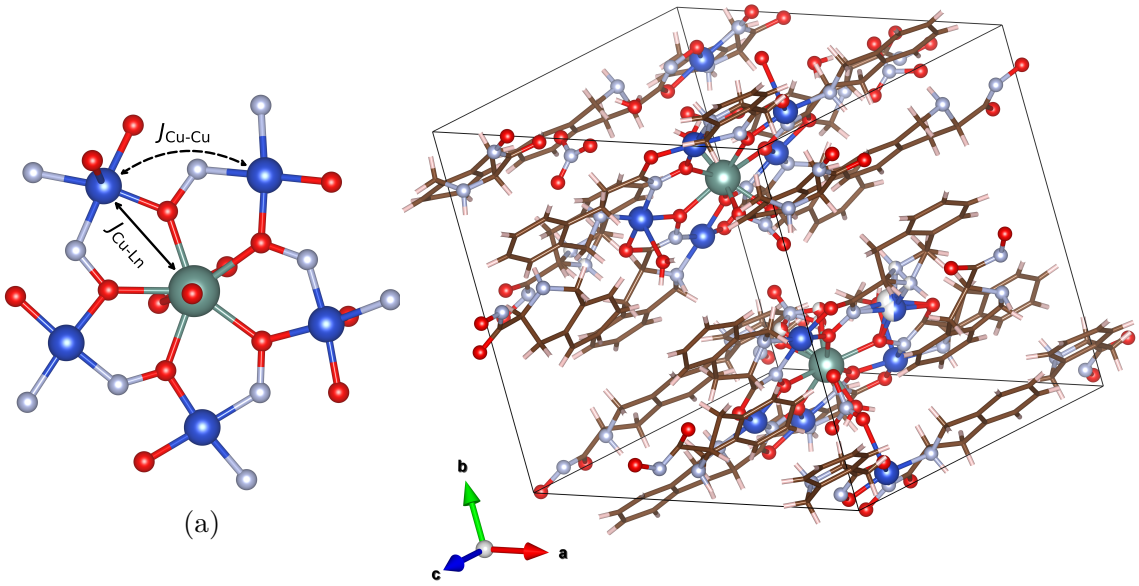
Fig. 5.1(a) shows the molecular structure of $\mathbf{(1_Y)}$. For clarity, only the first coordination spheres of the metal ions are shown. The Cu^{II} ions exhibit either four- or fivefold coordination. Due to their $3d^9$ electron configuration, the Cu^{II} ions have $S = 1/2$ ground state. The central Ln^{III} ion is coordinated by eight oxygen atoms. The five Cu^{II} ions are arranged in an almost perfectly planar geometry and bridged via (N-O) groups to each other, while being coordinated to the central Ln^{III} ion via a oxygen ion.

Fig. 5.1(b) shows the crystal packing of $\mathbf{(1_Y)}$. The crystallographic unit cell contains two inequivalent molecular sites related by inversion symmetry. In addition, the metallacrowns exhibit crystallographic disorder. This disorder typically differs between the molecules, which can lead to slightly different bonding environments.

5.2 Magnetisation Studies

The magnetisation data presented here were measured in the group of Prof. Eva Rentschler [53].

Fig. 5.2(a) shows the the temperature dependence of the static magnetic susceptibility $\chi = M/B$ of $\mathbf{(1_Y)}$, plotted as χT and measured at $B = 0.1$ T. Between 2 and 30 K, the χT-product exhibits an approximately constant value of $\chi T = 0.43(1)\ \mathrm{erg\,K/(G^2 mol)}$. This value is only slightly higher than than the



(a) (b)

Figure 5.1: (a) Molecular structure of $\mathbf{(1_Y)}$. For clarity, only the first coordination spheres of the metal ions are shown. $J_{\text{Cu-Ln}}$ denotes the exchange coupling between the Cu^{II} ions and the central Ln^{III} ion, while $J_{\text{Cu-Cu}}$ denotes the magnetic exchange coupling between the nearest-neighbour Cu^{II} ions within the ring. (b) Crystal packing of $\mathbf{(1_Y)}$. Colours: Cu (blue), Y (cyan), O (red), N (light blue), C (brown), H (pink). Black lines indicate the unit cell. Data from AG Rentschler [53]. The images were generated using VESTA [42].

value expected for a single electron (0.375 erg K/(G^{2}mol)), indicating a well-isolated $S = 1/2$ ground state for the complex, with an isotropic g-factor of $g = 2.14(2)$ derived from eq. (2.12). With increasing temperature, the χT-product increases, with the slope gradually decreasing above approximately 100 K. Even up to room temperature, no constant constant is observed. This indicates strong antiferromagnetic coupling between the Cu^{II} ions.

Fig. 5.2(b) shows the magnetic field dependence of the isothermal magnetisation of $\mathbf{(1_Y)}$ at temperatures between 2 and 10 K (in steps of 1 K). At $T = 2$ K, the magnetisation curve exhibits an approximately linear increase in the low-field region and approaches a plateau value of $M = 1.1\ \mu_B$/f.u. at 7 T. This behaviour is consistent with a $S = 1/2$ ground state, which also agrees with the susceptibility data at low temperatures.

A fit using

$$\hat{\mathcal{H}}_{(1)} = \sum_{i=1}^{5} \mu_B \boldsymbol{B} g \hat{\boldsymbol{S}}_i - \sum_{\langle i,j \rangle} J_{\text{Cu-Cu}} \hat{\boldsymbol{S}}_i \hat{\boldsymbol{S}}_j \tag{5.1}$$

was applied to the data and is shown as a solid lines in fig. 5.2. The first term of the Ham. (5.1) describes the Zeeman interaction of the spins with the external magnetic

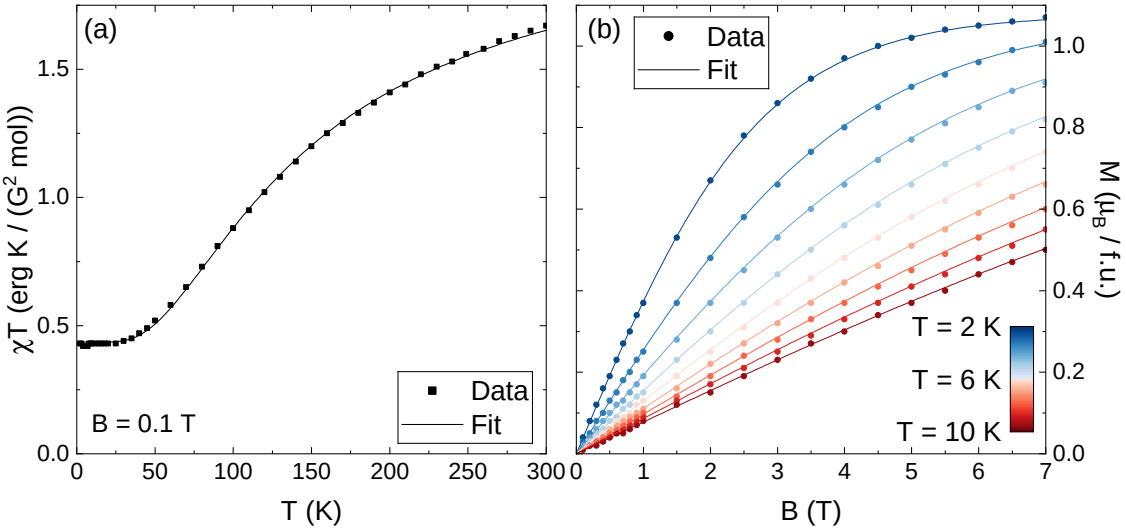


Figure 5.2: (a) Temperature dependence of the static magnetic susceptibility $\chi = M/B$ of $\mathbf{(1_Y)}$ plotted as χT and measured at $B = 0.1$ T. (b) Magnetic field dependence of the isothermal magnetisation of $\mathbf{(1_Y)}$ measured at different temperatures. Solid lines depict fits to the data as described in the text. Data from [53].

field, assuming an isotropic g-factor. The second term accounts for the magnetic coupling between the nearest-neighbours (nn) Cu^{II} ions. The corresponding magnetic exchange coupling, $J_{\text{Cu-Cu}}$, is indicated by a dashed arrow in fig. 5.1(a), respectively. Due to its closed-shell electronic configuration, the central Y^{III} ion has a ground state with $S = L = 0$ and therefore does not contribute to the magnetism of the complex. The fit to the data yields a g-factor of $g = 2.156(20)$ and an antiferromagnetic exchange coupling constant of $J_{\text{Cu-Cu}} = -148(10)$ K.

Fig. 5.3(a) shows the temperature dependence of the static magnetic susceptibility $\chi = M/B$ of $\mathbf{(2_{Gd})}$, plotted as χT and measured at $B = 0.1$ T. Starting from $\chi T = 9.65$ erg K/(G^{2}mol) at 2 K, the χT-product decreases significantly with increasing temperature and reaches a minimum of $\chi T = 8.32$ erg K/(G^{2}mol) at around 35 - 40 K. Towards higher temperatures, the χT-product increases again and, similar to $\mathbf{(1_Y)}$, no constant value is observed up to room temperature. The pronounced decrease at low temperatures can be attributed to weak ferromagnetic coupling between the Gd^{III} and Cu^{II} ions. The increase at higher temperatures can, as in $\mathbf{(1_Y)}$, be explained by strong antiferromagnetic coupling between the Cu^{II} ions.

Fig. 5.3(b) shows the magnetic field dependence of the isothermal magnetisation of $\mathbf{(2_{Gd})}$ at temperatures between 2 and 10 K (in steps of 1 K). At $T = 2$ K, the magnetisation curve exhibits an almost linear, steep increase in the low-field region and approaches a plateau value of $M \approx 8\ \mu_B$/f.u. at 7 T. This behaviour is consistent with a dominant contribution from the Gd^{III} ion ($S = 7/2$), which is weakly ferromagnetically coupled to the Cu^{II} ions forming a $S = 1/2$ ground state at low temperatures.

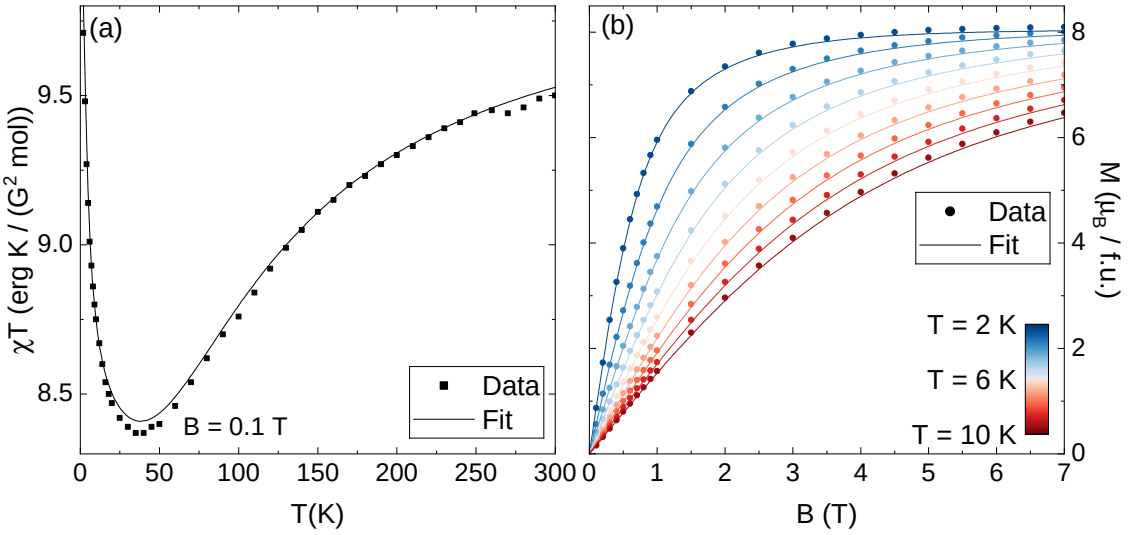


Figure 5.3: (a) Temperature dependence of the static magnetic susceptibility $\chi = M/B$ of $\mathbf{(2_{Gd})}$ plotted as χT and measured at $B = 0.1$ T. (b) Magnetic field dependence of the isothermal magnetisation of $\mathbf{(2_{Gd})}$ measured at different temperatures. Solid lines depict fits to the data as described in the text. Data from [53].

A fit using

$$\hat{\mathcal{H}}_{\mathbf{(2)}} = \hat{\mathcal{H}}_{\mathbf{(1)}} + \mu_B \boldsymbol{B} g_{Gd} \hat{\boldsymbol{S}}_{Gd} - \sum_{i=1}^{5} J_{Cu\text{-}Gd} \hat{\boldsymbol{S}}_i \hat{\boldsymbol{S}}_{Gd} \tag{5.2}$$

with $\hat{\mathcal{H}}_{\mathbf{(1)}}$ being the Hamiltonian of $\mathbf{(1_Y)}$, was applied to the data and is shown as a solid lines in fig. 5.3. The additional terms describe the Zeeman interaction of the Gd^{III} ion and the magnetic coupling to the Cu^{II} ions. Due to its half-filled $4f$ shell, the central Gd^{III} ion has a ground state with $L = 0$ and $S = 7/2$ according to Hund's rules.

Assuming the transferability of the spin Hamiltonian parameters of the Cu_5-subsystem, the isotropic g-factor of $g = 2.156$ for the Cu^{II} ions and the antiferromagnetic coupling constant between the nn Cu^{II} ions of $J_{Cu\text{-}Cu} = -148$ K were fixed during the fit. The fit yields a g-factor of $g_{Gd} = 1.99(2)$ for the Gd^{III} ion and a ferromagnetic coupling constant of $J_{Cu\text{-}Gd} = 1.3(3)$ K between the Gd^{III} ion and the Cu^{II} ions. The g-factor of the Gd^{III} ion is in good agreement with the expected spin only value.

Fig. 5.4(a) shows the temperature dependence of the static magnetic susceptibility $\chi = M/B$ of $\mathbf{(3_{Dy})}$, plotted as χT and measured at $B = 0.1$ T. The qualitative behaviour is very similar to that observed for $\mathbf{(2_{Gd})}$. Starting from $\chi T = 14.7$ erg K/(G^{2}mol) at 2 K, the χT-product decreases with increasing temperature, reaching a minimum around 16 K. At higher temperatures, χT increases again and does not reach a constant value up to room temperature. As observed for $\mathbf{(2_{Gd})}$, the low-temperature decrease can be attributed to weak ferromagnetic

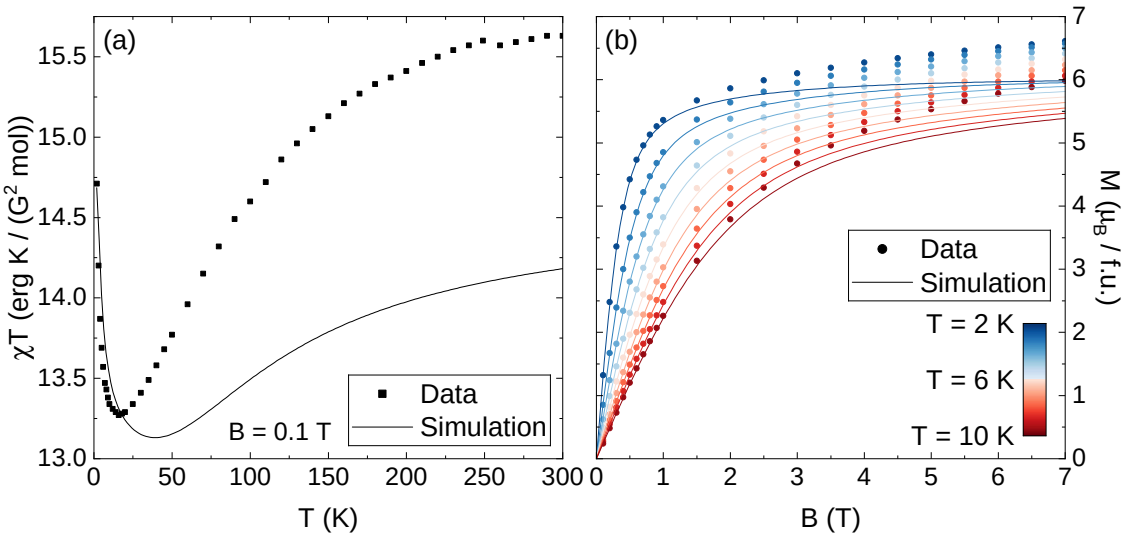


Figure 5.4: (a) Temperature dependence of the static magnetic susceptibility $\chi = M/B$ of $\mathbf{(3_{Dy})}$ plotted as χT and measured at $B = 0.1$ T. (b) Magnetic field dependence of the isothermal magnetisation of $\mathbf{(3_{Dy})}$ measured at different temperatures. Solid lines represents simulations to the data, as discussed later in the text. Data from [53].

coupling between the Dy^{III} and Cu^{II} ions, while the increase at higher temperatures reflects the strong antiferromagnetic interactions within the nn Cu^{II} ions.

Fig. 5.4(b) shows the magnetic field dependence of the isothermal magnetisation of $\mathbf{(3_{Dy})}$ at temperatures between 2 and 10 K (in steps of 1 K). At $T = 2$ K, the magnetisation curve exhibits an almost linear, steep increase in the low-field region. Above approximately 2 T, a weak linear increase continues up to high fields, and saturation is not reached even at 7 T.

5.3 HF-EPR Studies

HF-EPR spectra of complex $\mathbf{(1_Y)}$ were measured on a randomly oriented, fixed powder sample prepared as described in section 3.2.2. Fig. 5.5(a) shows the transmission spectra at $T = 2$ K for different frequencies up to $f = 378.8$ GHz. A single resonance feature is observed at all frequencies, consisting of a transmission minimum that exhibits a shoulder at lower magnetic fields. This feature broadens with increasing frequency. The overall shape indicates an easy-axis-type g-tensor anisotropy. At certain frequencies (e.g., 348.53 GHz), a secondary minimum can be observed within the shoulder, marked with a green triangle. The reason for its absence at other frequencies remains unclear.

The resonance positions of the main minima and the shoulder (steepest slope) in the HF-EPR spectra are shown in a frequency–field diagram in fig. 5.5(b). The resonance fields exhibit a linear dependence on the microwave frequency and were fit using the empiric relation:

$$hf_{\mathrm{res}} = \Delta_{\mathrm{ZFS}} + g_{\mathrm{eff}} \cdot \mu_{\mathrm{B}} B_{\mathrm{res}}. \tag{5.3}$$

The slopes of the fits are determined by effective g-factors of $g_{\mathrm{eff}} = 2.06(1)$ for the main minima and $g_{\mathrm{eff}} = 2.19(2)$ for the shoulder. The corresponding zero-field splittings, $\Delta_{\mathrm{ZFS}} = 0(3)$ GHz and $\Delta_{\mathrm{ZFS}} = 1(3)$ GHz, are negligibly small.

Fig. 5.6 shows the transmission spectra of complex $\mathbf{(1_Y)}$ at $f = 197.46$ GHz for temperatures from 2 K to 180 K. The resonance feature decrease in intensity with increasing temperature, indicating that it originates from a transition from (at least close to) the magnetic ground state.

All spectra were simulated using the Hamiltonian

$$\hat{\mathcal{H}}_{\mathrm{Cu_5Y}} = \sum_{i=1}^{5} \mu_{\mathrm{B}} \boldsymbol{B} \left(\overleftrightarrow{R}_z^T(\theta, \varphi_i) \overleftrightarrow{g} \overleftrightarrow{R}_z(\theta, \varphi_i) \right) \hat{\boldsymbol{S}}_i - \sum_{\langle i,j \rangle} J_{\mathrm{Cu\text{-}Cu}} \hat{\boldsymbol{S}}_i \hat{\boldsymbol{S}}_j \tag{5.4}$$

$$\text{with} \qquad \overleftrightarrow{g} = \begin{pmatrix} g_\perp & 0 & 0 \\ 0 & g_\perp & 0 \\ 0 & 0 & g_\parallel \end{pmatrix}.$$

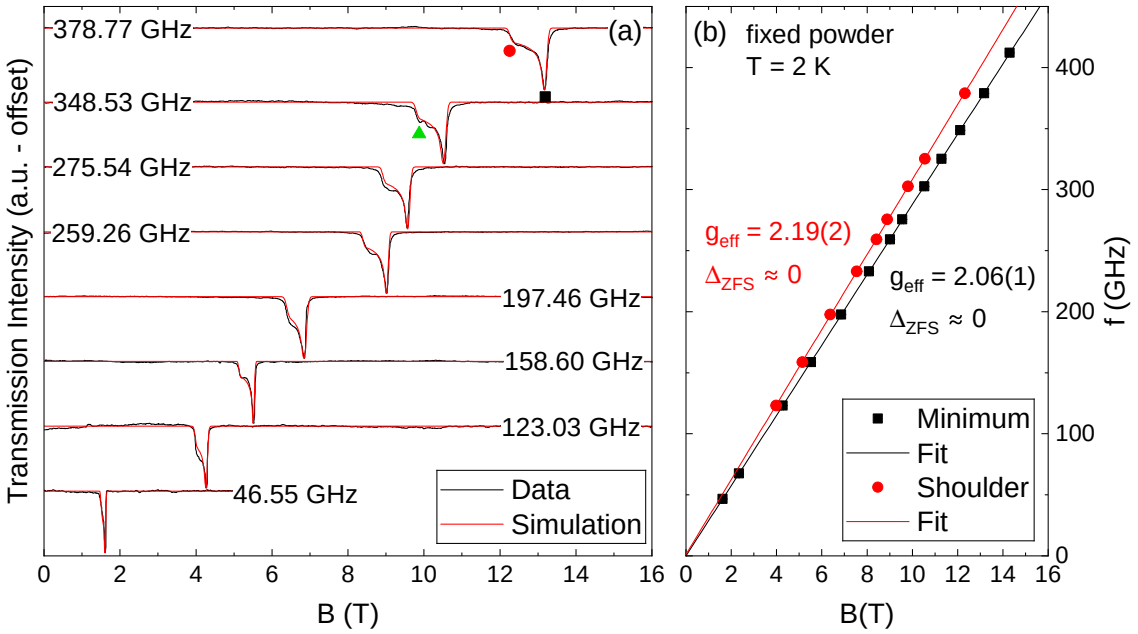


Figure 5.5: (a) HF-EPR spectra of a fixed powder sample of $\mathbf{(1_Y)}$ measured at 2 K and varying frequencies from 46.6 to 378.8 GHz. Red curves show simulations of the spectra as described in the text. All spectra are phase-mixing-corrected, background-corrected, normalised to the absolute of the lowest value and shifted along the ordinate. (b) Frequency-field diagram of $\mathbf{(1_Y)}$ at 2 K. The black squares corresponds to the minima and the red dots to the shoulder in the HF-EPR spectra. The resonances are fit using $hf_{\mathrm{res}} = \Delta_{\mathrm{ZFS}} + g_{\mathrm{eff}} \cdot \mu_{\mathrm{B}} B_{\mathrm{res}}$ (solid lines).

As in Ham. (5.1), the spin model includes the Zeeman interaction of the spins with the external magnetic field and and magnetic coupling between the nn Cu^{II} ions. In this case, however, an anisotropic g-tensor is considered. The molecular coordinate frame is defined such that the z-axis is oriented perpendicular to the plane of the pentagon formed by the five Cu^{II} ions. $\overleftrightarrow{R}_z(\theta, \varphi_i)$ denotes a tilting of the g-tensor frame by θ relative to the global z-axis and a rotation by φ_i around this axis, where φ_i is given by the C_5-symmetry.

The best simulations was obtained using an anisotropic g-factor with $g_\perp = 2.048(4)$ and $g_\parallel = 2.206(8)$, corresponding to an averaged isotropic g-factor of $g^{\text{iso}} = 2.101(6)$, which is slightly lower than the value obtained from the fit to the magnetic susceptibility. The HF-EPR spectra are relatively insensitive to the exact value of the magnetic coupling between the nn Cu^{II} ions for $|J_{\text{Cu-Cu}}| \geq 100$ K. Therefore, in the simulations, the antiferromagnetic coupling between the nn Cu^{II} ions was fixed to the value obtained from the magnetic susceptibility fit, i.e., $J_{\text{Cu-Cu}} = -148$ K. The simulations are also largely insensitive to angles in the range $0° \leq \theta \leq 10°$, with equally good agreement with the experimental data obtained for all values within this interval. Therefore, the simulations were performed using $\theta = 0$.

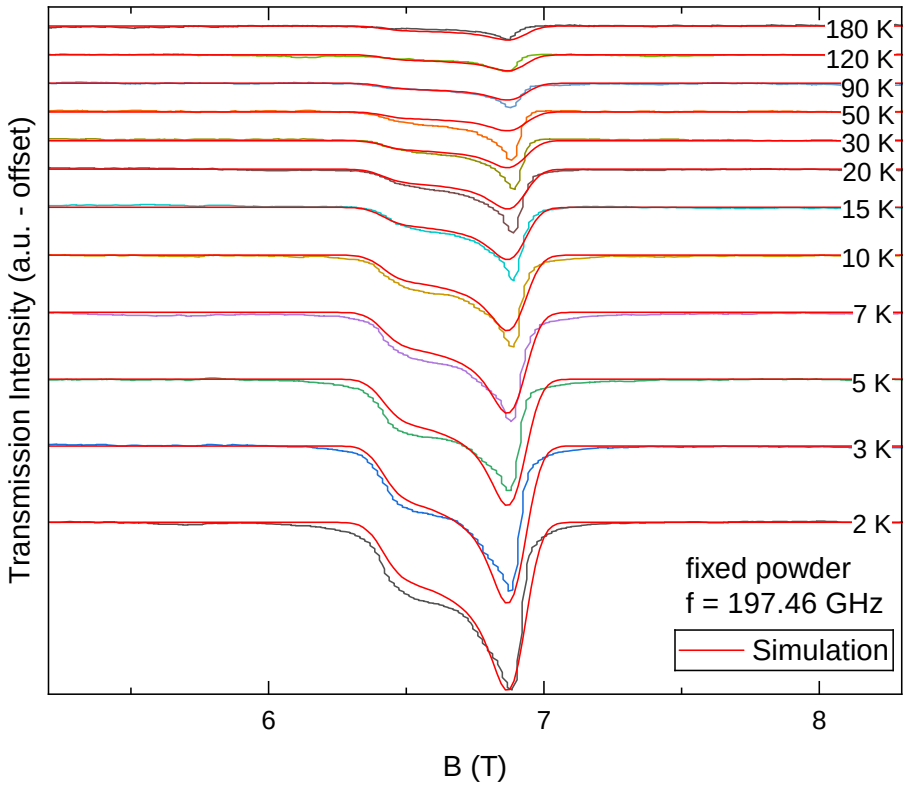


Figure 5.6: HF-EPR spectra of a fixed powder sample of $(\mathbf{1_Y})$ measured at $f = 197.46$ GHz for temperatures from 2 to 180 K. Red curves show simulations as described in the text. All spectra are phase-mixing-corrected, background-corrected, and shifted along the ordinate.

HF-EPR spectra of complex $\mathbf{(2_{Gd})}$ were also measured on a randomly oriented, fixed powder sample. Fig. 5.7 shows the resonance positions extracted from the transmission spectra at $T = 2$ K in a frequency-field diagram. Grey lines show the measured HF-EPR spectra (right y-axis) for different frequencies up to $f = 410.7$ GHz. A broad main absorption feature is observed at all frequencies. This feature broadens with increasing frequency and develops a weak shoulder at higher magnetic fields. In the spectra recorded at low frequencies ($f < 70$ GHz), a second, very weak feature is also visible.

The dependence of the resonance frequency f_{res} on the magnetic field is fit using eq. (5.3). From the fit to the resonance positions of the main feature (black solid line), an effective g-factor of $g_{\mathrm{eff}} = 2.02(1)$ is obtained with no significant ZFS. Fitting the resonance positions of the weak feature (red solid line) yields an effective g-factor of $g_{\mathrm{eff}} = 4.6(9)$. The large uncertainty arises from the fact that this resonance feature is only observed at a few low frequencies. The g-factor suggests that the weak feature may correspond to a nominally symmetry forbidden transition. Both the forbidden transition and the high-frequency shoulder likely arise from a weak magnetic anisotropy of the system. Due to the large number of possible simulation parameters, including additional pseudo-dipolar coupling between the Cu^{II} ions and the Gd^{III} ion, or the introduction of an additional single-ion anisotropy for the Gd^{III}

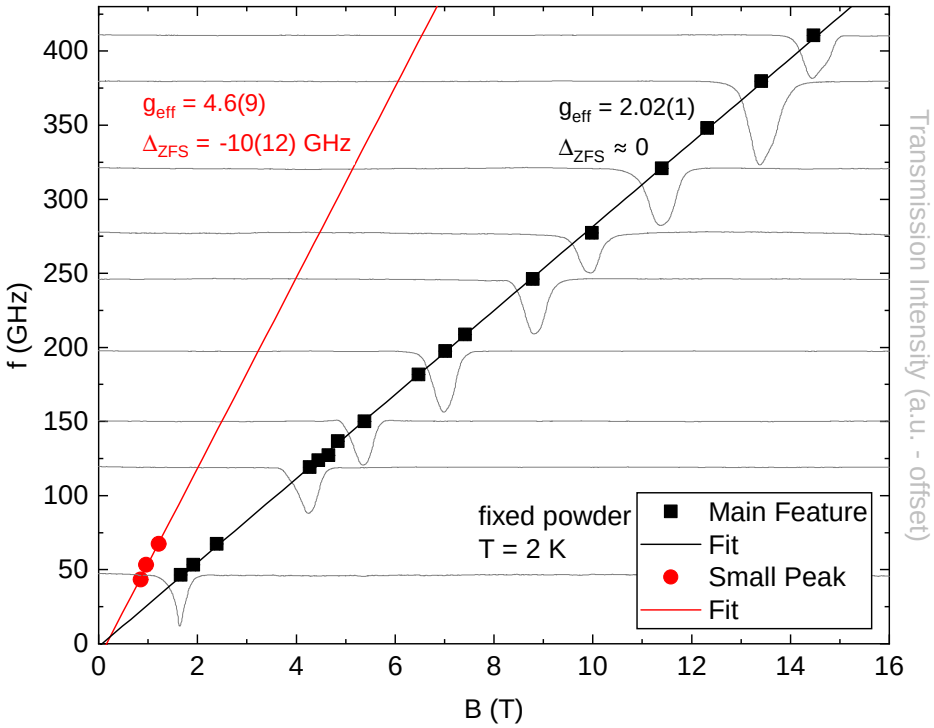


Figure 5.7: Frequency-field diagram for a fixed powder sample of $\mathbf{(2_{Gd})}$ obtained at $T = 2$ K. The resonance positions are fit using $hf_{\mathrm{res}} = \Delta_{\mathrm{ZFS}} + g_{\mathrm{eff}} \cdot \mu_{\mathrm{B}} B_{\mathrm{res}}$ (solid lines). Grey lines show the measured HF-EPR spectra, which are shifted along the ordinate to match with the corresponding resonance feature. All spectra are phase-mixing-corrected and background-corrected.

ion, it was not possible to simultaneously simulate all spectra using a single set of parameter.

Fig. 5.8 shows the transmission spectra of complex $\mathbf{(2_{Gd})}$ at $f = 197.46$ GHz for temperatures ranging from 2 K to 180 K. As the temperature increases, the resonance feature initially becomes narrower and simultaneously more intense, reaching a maximum peak amplitude at 12 K, after which the spectral weight decreases with further temperature increase.

HF-EPR spectra of complex $\mathbf{(3_{Dy})}$ were measured on an oriented, loose powder sample. Fig. 5.9 shows the resonance positions extracted from the transmission spectra at $T = 2$ K in a frequency-field diagram. Grey lines show the measured HF-EPR spectra (right y-axis) for different frequencies up to $f = 545.5$ GHz. One very broad main absorbtion feature is observed at all frequencies. Due to the low signal-to-noise ratio, the uncertainties in determining the resonance positions are relatively large. The resonance magnetic field increases linearly with increasing frequency. A fit using eq. (5.3) yields a zero-field splitting of $\Delta_{ZFS} = 88(15)$ GHz and an effective g-factor of $g_{eff} = 2.21(15)$.

Fig. 5.10 shows the transmission spectra of complex $\mathbf{(3_{Dy})}$ at $f = 197.63$ GHz for temperatures from 2 K to 25 K. The intensity of the main resonance feature decreases with increasing temperature, indicating that it originates from a transition from (at

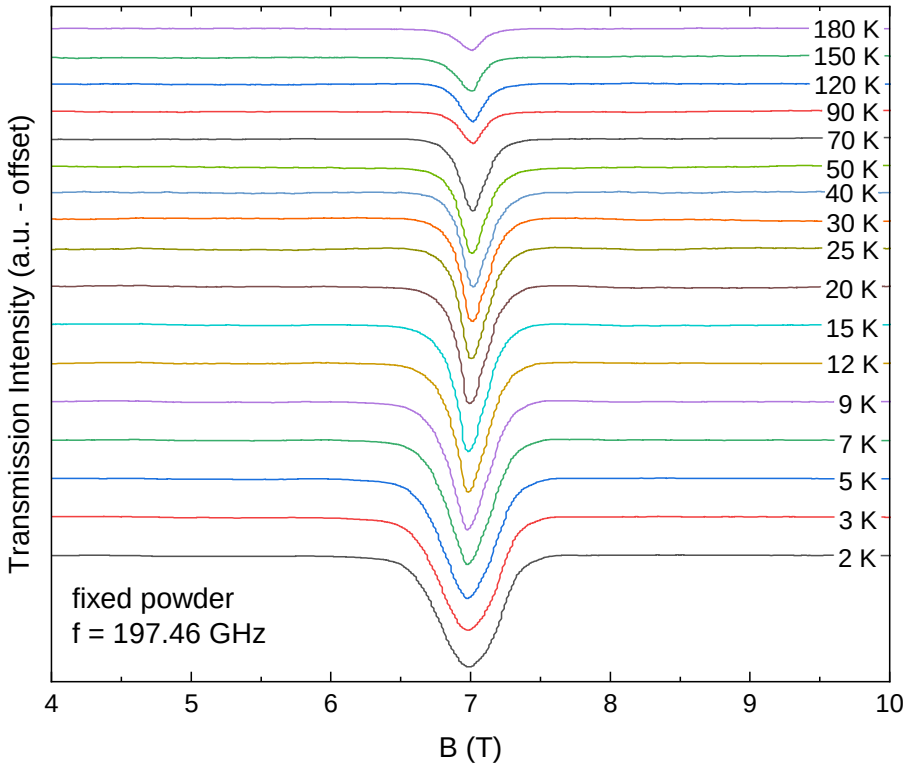


Figure 5.8: HF-EPR spectra of a fixed powder sample of $\mathbf{(2_{Gd})}$ measured at $f = 197.46$ GHz for temperatures from 2 to 180 K. All spectra are phase-mixing-corrected, background-corrected, and shifted along the ordinate.

least close to) the ground state. Above approximately 15 K, no resonance feature can be discerned.

Due to the strong magnetic anisotropy of lanthanides, particularly dysprosium, the Dy^{III} ion exhibits well-isolated ground-state doublets and can therefore be treated as an Ising-spin [54, 55]. Within this model, the Hamiltonian can be written as

$$\hat{\mathcal{H}}_{\mathrm{Cu_5Dy}} = \hat{\mathcal{H}}_{\mathrm{Cu_5Y}} + \mu_{\mathrm{B}} 2|m_J| \boldsymbol{B} \overleftrightarrow{g}_{\mathrm{Dy}} \hat{\boldsymbol{S}}_{\mathrm{Dy}}^{\mathrm{Ising}} - \sum_{i=1}^{5} 2|m_J| J_{\text{Dy-Cu}} \hat{S}_{i,\mathrm{z}} \hat{S}_{\mathrm{Dy,z}}^{\mathrm{Ising}}, \qquad (5.5)$$

with $S_{\mathrm{Dy}}^{\mathrm{Ising}} = 1/2$, $\overleftrightarrow{g}_{\mathrm{Dy}} = (0, 0, 4/3)$, and $\hat{\mathcal{H}}_{\mathrm{Cu_5Y}}$ being the Hamiltonian of $\mathbf{(1_Y)}$ (see eq. (5.4)). The factor $2|m_J|$ accounts for the renormalisation of the pseudospin transformation, which results from the projection onto the effective doublet. Since the Cu_5-subsystem of the Dy^{III} ion in $\mathbf{(3_{Dy})}$ is essentially identical to that of the Y^{III} ion in $\mathbf{(1_Y)}$, it is reasonable to fix the parameters obtained from the HF-EPR studies of $\mathbf{(1_Y)}$.

In this model, the Dy^{III} ion exhibits strong magnetic anisotropy with a well-defined easy axis. Owing to its pronounced Ising-like character, the magnetic moments align along the easy axis of the Dy^{III} ion in an applied magnetic field. From the

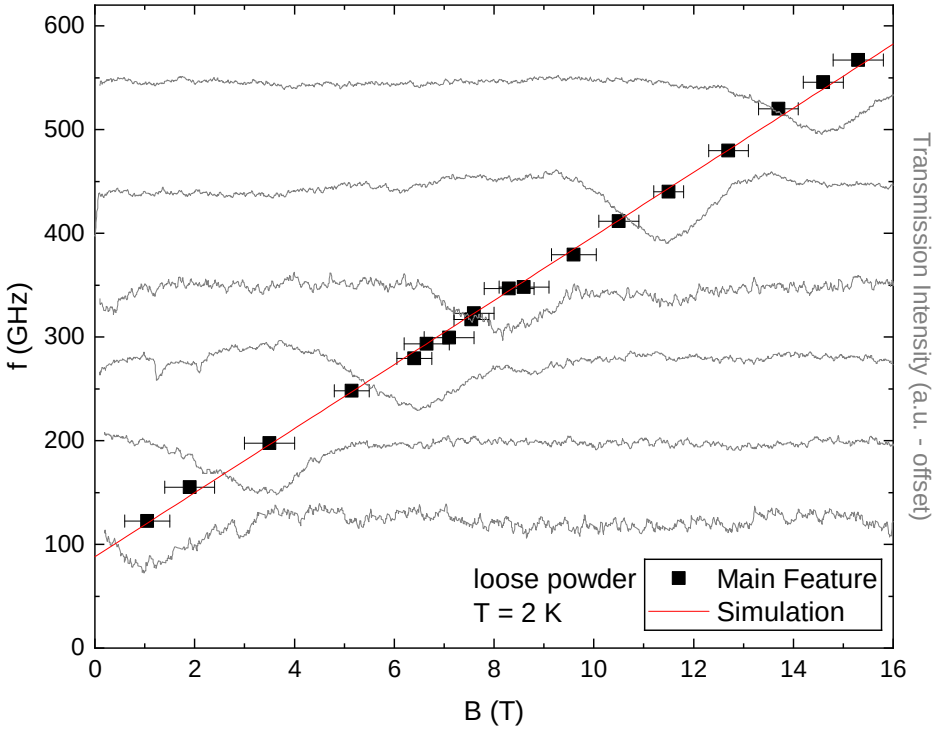


Figure 5.9: Frequency-field diagram for a loose powder sample of $\mathbf{(3_{Dy})}$ obtained at $T = 2$ K. The red solid line shows a simulation as described in the text. Grey lines show the measured HF-EPR spectra, which are shifted along the ordinate to match with the corresponding resonance feature. All spectra are background-corrected. The spectra could not be phase-mixing-corrected.

analysis of $(\mathbf{1_Y})$, it is known that the principal axis of the local g-tensor at each Cu center is essentially aligned with the z-axis of the molecular coordinate system, i.e., perpendicular to the Cu−5-plane. In principle, the easy axis of the Dy^{III} ion may be tilted with respect to this axis, but based on the effective g-factor of the observed resonance branch, it can be concluded that both axis are almost completely aligned. A significant tilt of the Dy^{III} easy axis relative to the Cu^{II} axes would result in a smaller effective g-factor.

The best agreement between simulation and experimental data is achieved with a ferromagnetic coupling of $2|m_J|J_{\text{Dy-Cu}} = 8.5(8)$ K. Fig. 5.4(b) shows the simulations of the isothermal magnetisation with $|m_J| = 15/2$ and $J_{\text{Dy-Cu}} = 0.57(5)$ K as solid lines. The model describes the data very well up to approximately 1.5 T. The deviations at higher fields are likely associated with finite contributions from the transverse components of the Dy^{III} moment, in particular deviations from pure Ising-spin character. Introducing transverse components of the effective dysprosium g-tensor does not improve the agreement; while it allows the simulations to better reproduce the high-field data, it leads to significant deviations at lower fields. The simulation of the χT data using the same parameters (see fig. 5.4(a)) can only reproduce the low-temperature χT regime. The Hamiltonian in eq. (5.5) is not sufficient to describe the χT-product at higher temperatures. This is not surprising,

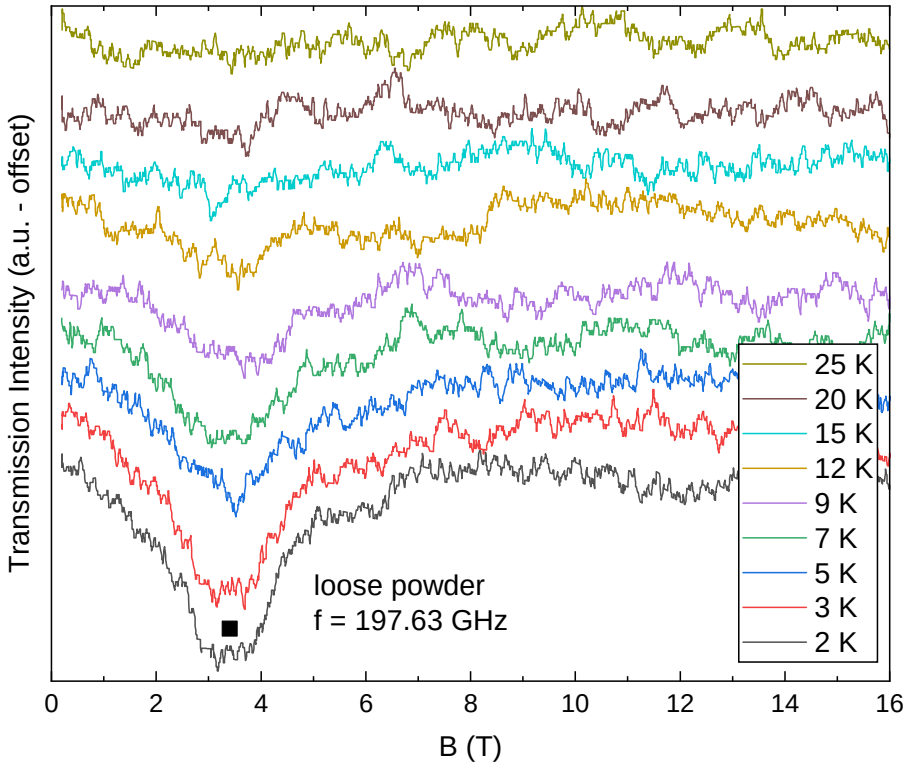


Figure 5.10: HF-EPR spectra of a loose powder sample of $(\mathbf{3_{Dy}})$ measured at $f = 197.63$ GHz for temperatures from 2 to 25 K. All spectra are background-corrected and shifted along the ordinate. The spectra could not be phase-mixing-corrected.

since at elevated temperatures higher-lying m_J sublevels become thermally populated and the magnetic moment of the Dy^{III} ion can no longer be described by an effective Ising-spin model.

5.4 Discussion

From the simulations of the HF-EPR spectra for **($\mathbf{1_Y}$)** an anisotropic g-tensor for the Cu^{II} ions is derived, which arises from the non-negligible spin–orbit coupling. The g-values $g_\perp = 2.048(4)$ and $g_\parallel = 2.206(8)$ are in good agreement with previously reported values. For example, Ref. [56] reports a $Cu_5^{II}Y^{III}$ 15-MC-5 metallacrown with $g_\perp = 2.03(2)$ and $g_\parallel = 2.25(2)$. In Ref. [57], a Cu_4Cu complex from the 12-MC-4 metallacrown family was investigated, yielding anisotropic g-factor components of $g_x = 2.03(1)$, $g_y = 2.04(1)$, and $g_z = 2.23(1)$. In both studies, the g-factors were obtained from EPR measurements.

The exchange coupling between the nn Cu^{II} ions arises from a superexchange via the N–O bridging unit. With average Cu-N-O and N-O-Cu bond angles of 120° and 105°, respectively, antiferromagnetic coupling is observed. The antiferromagnetic coupling, $J_{\text{Cu-Cu}} = -148(10)$ K, is obtained from fits to the magnetisation data of **($\mathbf{1_Y}$)** and lies within the range reported for other $Cu_5^{II}Ln^{III}$ 15-MC-5 metallacrowns. Based on susceptibility measurements, Ref. [56] reports a coupling of $J_{\text{Cu-Cu}} = -157$ K for Ln = Y. For Ln = Pr, Nd, Sm, and Eu, Ref. [58] reports values in the range $-181(3)$ K $\leq J_{\text{Cu-Cu}} \leq -135(2)$ K. For Ln = Gd, coupling constants of $J_{\text{Cu-Cu}} = -176(2)$ K and $J_{\text{Cu-Cu}} = -157(2)$ K were reported in Refs. [59, 60].

For **($\mathbf{2_{Gd}}$)**, the resonance positions of the minima in the HF-EPR spectra exhibit an effective g-factor of $g_{\text{eff}} = 2.02(1)$. Since the absorbed microwave power in the HF-EPR experiment scales with $S(S+1)$ [8], the signal is dominated by the Gd^{III} ion. Consequently, the effective g-factor is mainly determined by the g-factor of the Gd^{III} ion, i.e., $g_{\text{eff}} \approx g_{\text{Gd}}$. Its value is therefore only slightly higher than the g-factor obtained from fits to the magnetisation data and consistent with previously reported values for $Cu_5^{II}Gd^{III}$ 15-MC-5 metallacrowns [59, 60], where $g_{\text{Gd}} = 2.033(1)$ and $g_{\text{Gd}} = 2.032(1)$ were found, respectively.

The coupling between the Gd^{III} and the Cu^{II} ion in **($\mathbf{2_{Gd}}$)** is also based on superexchange. Electron transfer from the singly occupied $3d$ orbital of copper into an empty $5d$ orbital of the Gd^{III} ion leads to a preferred ferromagnetic alignment in the virtual excited states due to Hund's coupling [61]. With $J_{\text{Cu-Gd}} = 1.3(3)$ K, the value obtained here is only slightly lower than those reported in Refs. [59, 60], where $J_{\text{Cu-Gd}} = 1.73(6)$ K and $J_{\text{Cu-Gd}} = 2.45(3)$ K were obtained.

Replacing Gd^{III} with Dy^{III} in **($\mathbf{3_{Dy}}$)** results in a reduced ferromagnetic coupling between the Ln^{III} and Cu^{II} ions, with $J_{\text{Cu-Dy}} = 0.57(5)$ K. This decrease can be attributed to the decreasing number of unpaired $4f$ electrons on the Ln^{III} ion and the resulting weakening of Hund's coupling [55].

6 All-Metal-Aromaticity: Bi_4 Ring

Benzene, discovered by Michael Faraday in 1825, played a central role in the development of the concept of aromaticity. Its unusual stability, high degree of chemical unsaturation and high structural symmetry, was eventually explained by the presence of cyclically delocalized electrons [62]. When such a delocalized electronic system is placed in an external magnetic field, a ring current can be induced. This results in a diamagnetic exaltation in an external magnetic field [63], i.e., enhanced diamagnetic susceptibilities compared to those predicted by Pascal's constants [64].

Aromaticity is well defined in organic molecules; however, its role in purely metallic rings remains controversial. Recently, the group of Prof. Lutz Greb (Heidelberg University) reported the synthesis and stabilisation of an all-metal Bi_4 ring [65]. Their combined crystallographic, spectroscopic, and theoretical investigations provided strong evidence for σ-aromaticity. In this context, the Bi_4 system was investigated with respect to its diamagnetic response. For comparison, the same measurements were performed on an isostructural compound containing a Li_4Br unit.

6.1 Molecular Structure

Both samples were synthesised by Avijit Maiti (group of Prof. Lutz Greb, Heidelberg University) and structurally characterised via single crystal X-ray diffraction within the same group. The molecular structures of both compounds are shown in fig. 6.1. The two systems differ only in their central structural unit, consisting of either a Bi_4 ring or a Li_4Br unit. The surrounding metal–organic ligand framework is identical in both cases.

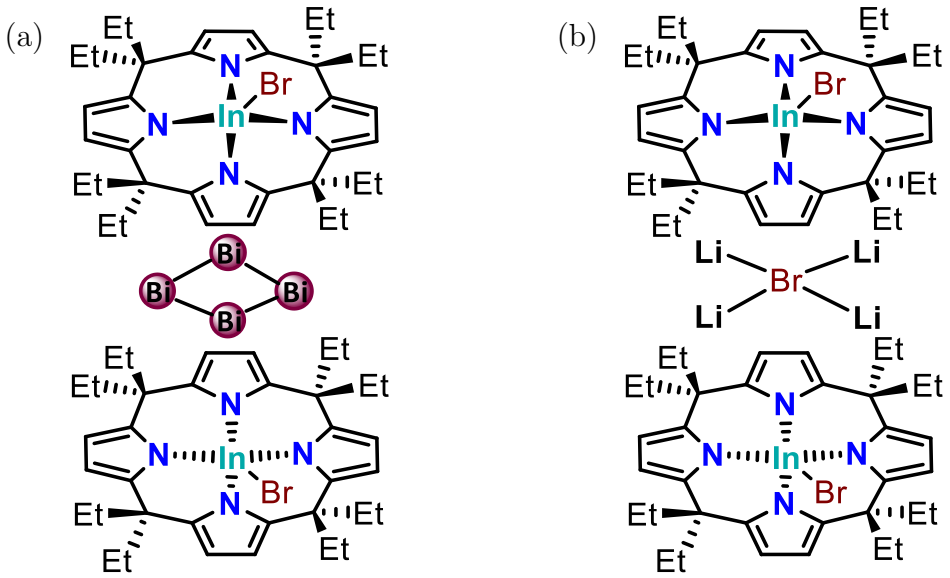


Figure 6.1: (a) Molecular structure of all-metal-σ-aromatic Bi_4 ring; (b) Molecular structure of isostructural compound containing a Li_4Br unit. Structures from [66].

6.2 Magnetisation Studies

Both samples were provided as polycrystalline powder samples sealed in capsules (see section 3.1.2). In order to measure the small diamagnetic response of the samples, the measurements were performed as follows. The capsule containing the sample was first measured in a brass sample holder. Afterwards, the sample was removed from the capsule, which was then cleaned and reinstalled empty on the brass sample holder at exactly the same position (see section 3.1.2). Since the capsule had been filled with the sample prior to the measurements, an accurate determination of the sample mass was possible by comparing the mass of the filled and the empty cleaned capsule after the first measurement. This yielded $m^{Bi_4} = 14.10(10)$ mg and $m^{Li_4} = 20.23(10)$ mg ($M^{Bi_4} = 2298.98$ g/mol and $M^{Li_4} = 1721.87$ g/mol [66]).

Fig. 6.2(a) shows the magnetic field dependence of the isothermal magnetisation of the Bi_4 and Li_4 samples at three different temperatures. In both samples, the isothermal magnetisation changes only slightly over the temperature range 100–300 K. At low fields, both samples exhibit an initial positive increase, which is much more pronounced for the Bi_4 sample. At higher fields, the magnetisation of both samples decreases linearly with increasing field up to 7 T. The jump in the magnetisation at $M \approx 0$ arises from the fact that the background signal of the capsule cannot be perfectly subtracted and has a strong influence when the magnetic signal of the sample is very small. Therefore the background subtraction breaks down at vanishing momenta. The initial positive slope indicates impurities in the sample that superimpose the

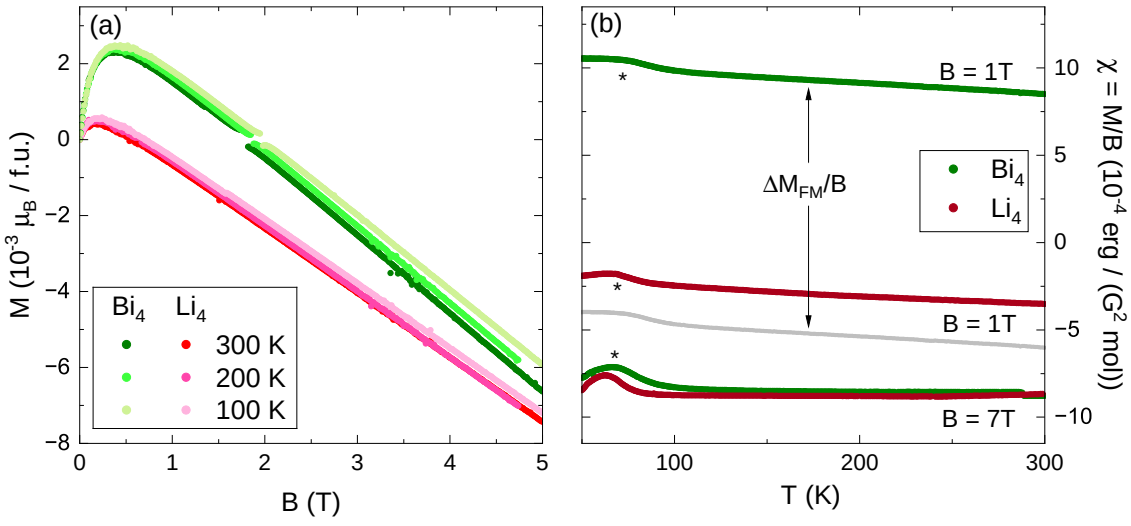


Figure 6.2: (a) Magnetic field dependence of the isothermal magnetisation of the Bi_4 and Li_4 samples at 100 K, 200 K, and 300 K. (b) Static magnetic susceptibility of the Bi_4 and Li_4 samples measured at $B = 1$ T and $B = 7$ T. Grey data points show the data of Bi_4, at 1 T, after subtracting an offset as described in the text. The anomaly marked by the asterisk originates from the sample holder and is assumed to result from absorbed oxygen in the capsules.

diamagnetic response of the main compounds. Due to the temperature-independence of this contribution, these impurities are likely ferromagnetic.

A restricted linear fit to the high field region of the isothermal magnetisation yields saturation magnetisations of $M_{\mathrm{FM}}^{\mathrm{Bi_4}} = 3.8(1) \cdot 10^{-3}$ μ_{B}/f.u. and $M_{\mathrm{FM}}^{\mathrm{Li_4}} = 1.2(1) \cdot 10^{-3}$ μ_{B}/f.u.. The ferromagnetic impurity may originate from small amounts of iron (Fe) or magnetite (Fe_3O_4) that were introduced during sample synthesis. Using $\mu_{\mathrm{sat,Fe}} = 2.219$ μB/f.u. and $\mu_{\mathrm{sat,Fe_3O_4}} = 4.07$ μ_{B}/f.u. [67], the corresponding relative amounts of ferromagnetic iron (n_{Fe}) or magnetite ($n_{\mathrm{Fe_3O_4}}$) impurities can be estimated and are listed in tab 6.1. Although the estimated mass fractions of these impurities are small, their contribution becomes noticeable because the diamagnetic signal of the main phase is very weak.

Fig. 6.2(b) shows the temperature dependence of the static susceptibility, $\chi = M/B$, at applied magnetic fields of $B = 1$ T and $B = 7$ T. Between 100 and 300 K, the measurements at $B = 7$ T remain essentially constant, while those at $B = 1$ T show a slight decrease over the same temperature range. The anomaly marked by the asterisk around 70 K originates from the sample holder and is assumed to result from absorbed oxygen in the capsules. The large difference between the susceptibilities measured at 1 T compared to 7 T is caused by the small amounts of ferromagnetic impurities. Because the Bi_4 and Li_4 samples contain different amounts of these impurities, χ at $B = 1$ T deviates significantly between the two samples. The grey data points represent the data of the Bi_4-sample at 1 T after subtracting an offset M_{FM}/B (with $M_{\mathrm{FM}} = M_{\mathrm{FM}}^{\mathrm{Bi_4}} - M_{\mathrm{FM}}^{\mathrm{Li_4}}$) to account for the different amounts of ferromagnetic impurities and thereby reveal the similar temperature dependence of χ for the main phase in both compounds. At $B = 7$ T, the susceptibilities of both samples lie much closer to each other due to the saturation of the ferromagnetic impurity contribution and the relatively larger influence of the diamagnetic response compared to the measurements at 1 T.

Fig. 6.3(a) shows the non-linear contribution to the isothermal magnetisation associated with the ferromagnetic impurity (left axis), while the original data are shown in grey (right axis). Unfortunately, the measurement data below 50 K could not be used, as the background subtraction procedure with the signal of the empty capsule was unreliable in this temperature range. Further details regarding tests at $T \leq 50$ K are shown in the appendix. Since the diamagnetic response of the

	n_{Fe} (10^{-3} wt%)	$n_{\mathrm{Fe_3O_4}}$ (10^{-3} wt%)
Bi_4	4.18(11)	9.45(25)
Li_4	1.75(20)	3.96(46)

Table 6.1: Relative amounts of ferromagnetic iron or magnetite corresponding to the FM moment measured in the Bi_4 and Li_4 samples, reported as mass fraction (wt %), i.e., the fraction of the total sample mass attributed to the ferromagnetic impurity.

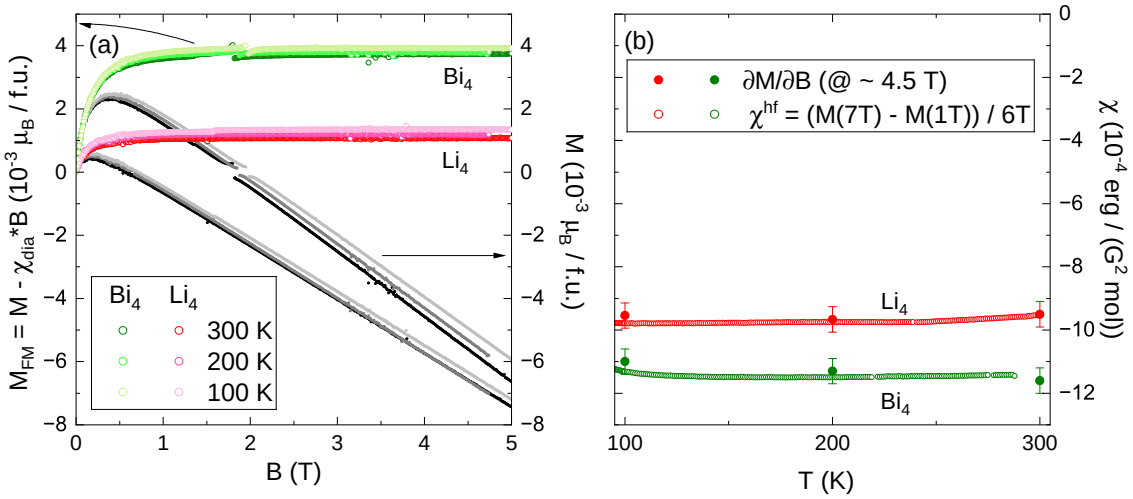


Figure 6.3: (a) Temperature-independent non-linear part of the isothermal magnetisation associated with a ferromagnetic impurity (left axis) and original data in grey (right axis). (b) Differential magnetic susceptibility $\partial M/\partial B$ at ~ 4.5 T and high-field static magnetic susceptibility χ^{hf} as described in the text.

samples is expected to be temperature-independent, it is sufficient to restrict the measurements and analysis to the investigated temperature range.

In order to determine the diamagnetic response of the main phase, three approaches were used. First, the high-field differential magnetic susceptibility $\partial M/\partial B$ was calculated from the measured isothermal magnetisation $M(B)$ at ~ 4.5 T. Second, the $M(B)$ data were linearly fit at high fields ($B \geq 2$ T). Third, the high-field static susceptibility, χ^{hf}, was determined from the difference between the measured magnetisation at external magnetic fields $B_2 = 7$ T and $B_1 = 1$ T and divided by the field difference:

$$\chi^{\mathrm{hf}} = \frac{M(7\ \mathrm{T}) - M(1\ \mathrm{T})}{6\ \mathrm{T}}. \tag{6.1}$$

The quantity χ^{hf} represents an experimental approach to suppress the influence of small ferromagnetic impurity phases. The different susceptibilities obtained from these methods are shown in fig. 6.3(b). All three procedures consistently yield $\chi^{\mathrm{Bi_4}} = -11.3(7) \cdot 10^{-4}$ erg/(G^2 mol) and $\chi^{\mathrm{Li_4}} = -9.6(5) \cdot 10^{-4}$ erg/(G^2 mol).

6.3 Comparison and Conclusion

To place the experimentally determined susceptibilities into context, the obtained values were compared with diamagnetic reference values calculated from Pascal's constants [64]. These represent an additive estimate of the molecular diamagnetic contributions of individual atoms or structural fragments. The value calculated from Pascal's constants for the Li_4 sample is $\chi^{\mathrm{Li_4}}_{\mathrm{Pascal}} = -12.4 \cdot 10^{-4}$ erg/(G^2 mol), which is

in good agreement with the experimental result. The relatively small deviation can be attributed to experimental uncertainties as well as to the limited accuracy of the additive Pascal approximation.

In contrast, estimating the expected diamagnetism of the Bi_4 ring from Pascal's constants involves a larger uncertainty, since the effective oxidation state of the bismuth atoms cannot be uniquely determined in this case. This leads to a calculated reference range of approximately $-17.25 \cdot 10^{-4}$ erg/(G^2 mol) $\leq \chi_{\text{Pascal}}^{\text{Bi}_4} \leq -10.5 \cdot 10^{-4}$ erg/(G^2 mol). The experimental value lies within this theoretical range. Therefore, a significantly enhanced diamagnetism that could serve as a clear indication of a ring current cannot be clearly deduced from the present data. The results are therefore compatible with a possible aromatic contribution, but they do not provide a clear quantitative confirmation. Due to the larger uncertainty in the Pascal's constants for the Bi_4 sample, a direct quantitative comparison with the Li_4 sample is not meaningful.

7 Summary and Conclusion

In this thesis, high-frequency/high-field electron paramagnetic resonance spectroscopy (HF-EPR) as well as static and dynamic magnetisation measurements were performed to investigate the magnetic anisotropy, exchange interactions, and other magnetic properties in different metal-organic molecular complexes.

HF-EPR and magnetisation measurements were carried out on a series of five $Co^{II}Co^{III}_4$ complexes. The central paramagnetic Co^{II} ion is coordinated in a distorted tetrahedral coordination environment. Studies on a representative complex reveal easy-plane anisotropy of $D = 580(150)$ GHz and a pronounced anisotropic g-tensor with $g_\perp = 2.27(5)$ and $g_\parallel = 2.07(5)$. All complexes show slow field-induced magnetic relaxation at $B_{dc} = 0.1$ T in dynamic susceptibility measurements. While the $Co^{II}Co^{III}_4$ core remains identical across the series, variations in the para-substituted benzoic acid ligands induce changes in the degree of tetrahedral distortion at the Co^{II} ion. Qualitative analysis revealed that an increasing deviation from ideal tetrahedral geometry results in enhanced magnetic anisotropy. Complex **(5)** of the series exhibits a completely different static magnetisation behaviour than the others, which may be attributable to antiferromagnetic intermolecular coupling.

$Cu^{II}_5Ln^{III}$ 15-MC-5 metallacrowns $[Ln[15\text{-}MC_{Cu(II)N(\text{-}THIQHA)}\text{-}5](NO_3)_3(H_2O]$(Ln = Y, Gd, Dy) were studied by HF-EPR measurements. Additional static magnetisation measurements were performed in the group of Prof. Eva Rentschler [53]. In all complexes, strong antiferromagnetic exchange coupling between the magnetic moments of nearest-neighbour Cu^{II} ions within the pentagonal ring structure is observed. The coupling $J_{Cu\text{-}Cu} = -148(10)$ K, along with an anisotropic g-tensor with $g_\perp = 2.048(4)$ and $g_\parallel = 2.206(8)$ for the Cu^{II} ions, was obtained from studies on the Y^{III} containing complex. The complexes containing Gd^{III} or Dy^{III} as the central ions exhibit weak ferromagnetic coupling between the magnetic moments of the Cu^{II} ions and the Ln^{III} ion, arising from a $3d \rightarrow 5d$ charge-transfer process. For the Gd^{III} complex, a ferromagnetic coupling of $J_{Cu\text{-}Gd} = 1.3(3)$ K was evidenced by static magnetisation measurements; however, this simple isotropic model is not able to reproduce the spectroscopic results. By modelling the magnetic moment of the Dy^{III} ion as an Ising-spin, the ferromagnetic Cu-Dy coupling was determined to be $J_{Cu\text{-}Dy} = 0.57(5)$ K. The easy axis of the Dy^{III} ion is essentially aligned with the principal axis of the local g-tensor at each Cu center. Both being oriented perpendicular to the plane of the pentagon formed by the five Cu^{II} ions.

An all-metal-σ-aromatic Bi_4 ring was examined by static magnetisation measurements to probe possible diamagnetic exaltation arising from induced ring currents. For comparison, the same measurements were performed on an isostructural compound containing a Li_4Br unit. In both samples, the magnetic response of the system is superimposed by a possible small ferromagnetic impurity. After subtracting this contribution, a diamagnetic behaviour is observed. However, due to the unresolved oxidation states of the bismuth atoms, the atomic diamagnetic response is not well

known, and a definitive conclusion regarding the presence of diamagnetic exaltation could not be drawn.

In conclusion, this thesis presents a systematic investigation of the magnetic properties of $3d$-, $3d$–$4f$-, and Bi-based metal–organic molecular complexes using HF-EPR spectroscopy and magnetisation measurements. The results provide detailed insight into magnetic anisotropy and exchange interactions. In particular, the study highlights how structural variations and the choice of the magnetic ion influence the resulting magnetic behaviour in the molecular systems. This could be used to further improve the magnetic properties of molecular systems by tuning the magnetic anisotropy through appropriate molecular design.

Appendix

A.1 Additional measurements and molecular structures of $Co^{II}Co^{III}_4$ complexes

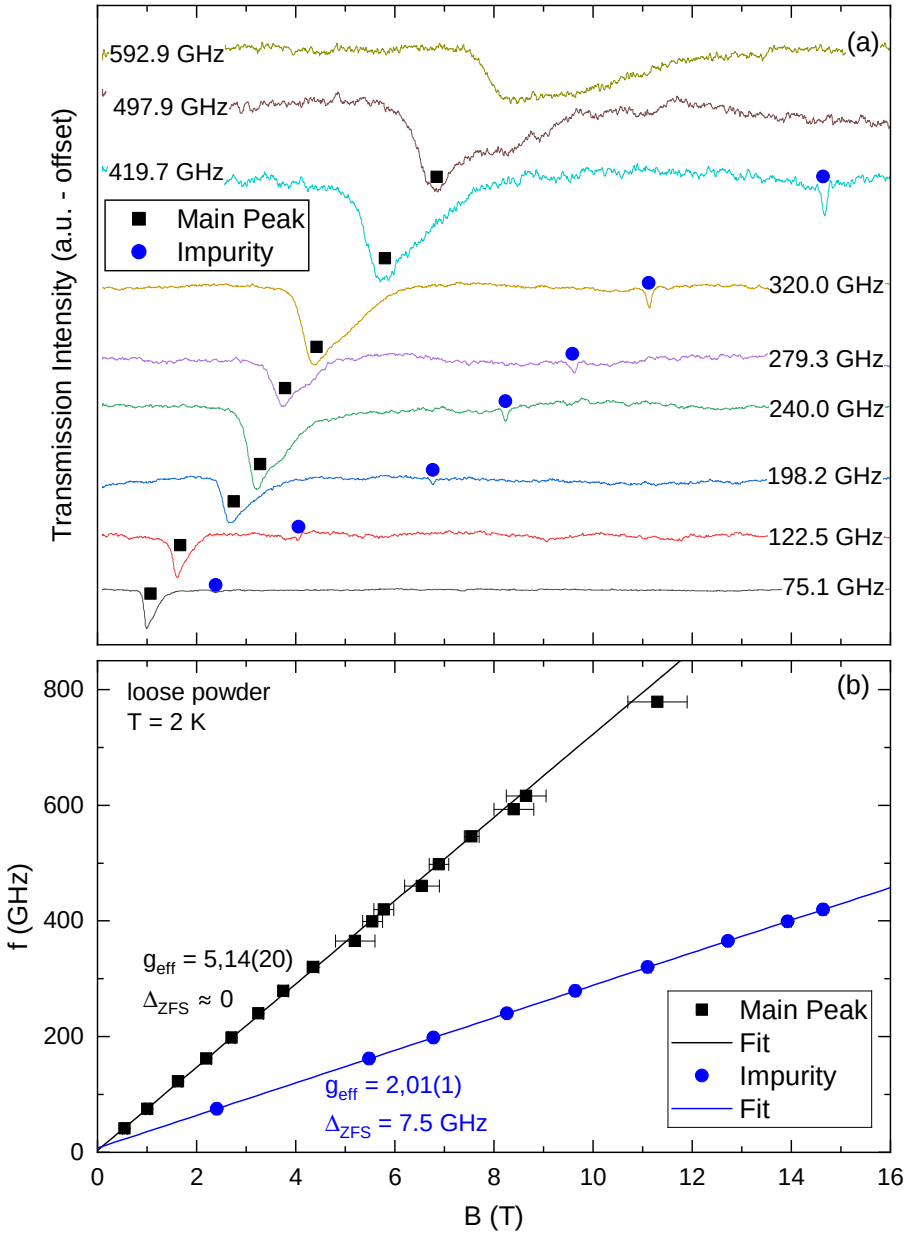


Figure A.1.1: (a) HF-EPR spectra of a loose powder sample of **(1)** measured at 2 K and varying frequencies from 75.1 to 592.9 GHz. All spectra are background- and phase-mixing-corrected, and shifted along the ordinate. (b) Frequency-field diagram of **(1)** at 2 K. The resonance positions (black squares) correspond to the minima in the HF-EPR spectra, while the blue dots indicate an impurity-related feature. The resonances are fit using $hf_{\mathrm{res}} = \Delta_{\mathrm{ZFS}} + g_{\mathrm{eff}} \cdot \mu_{\mathrm{B}} B_{\mathrm{res}}$ (solid lines).

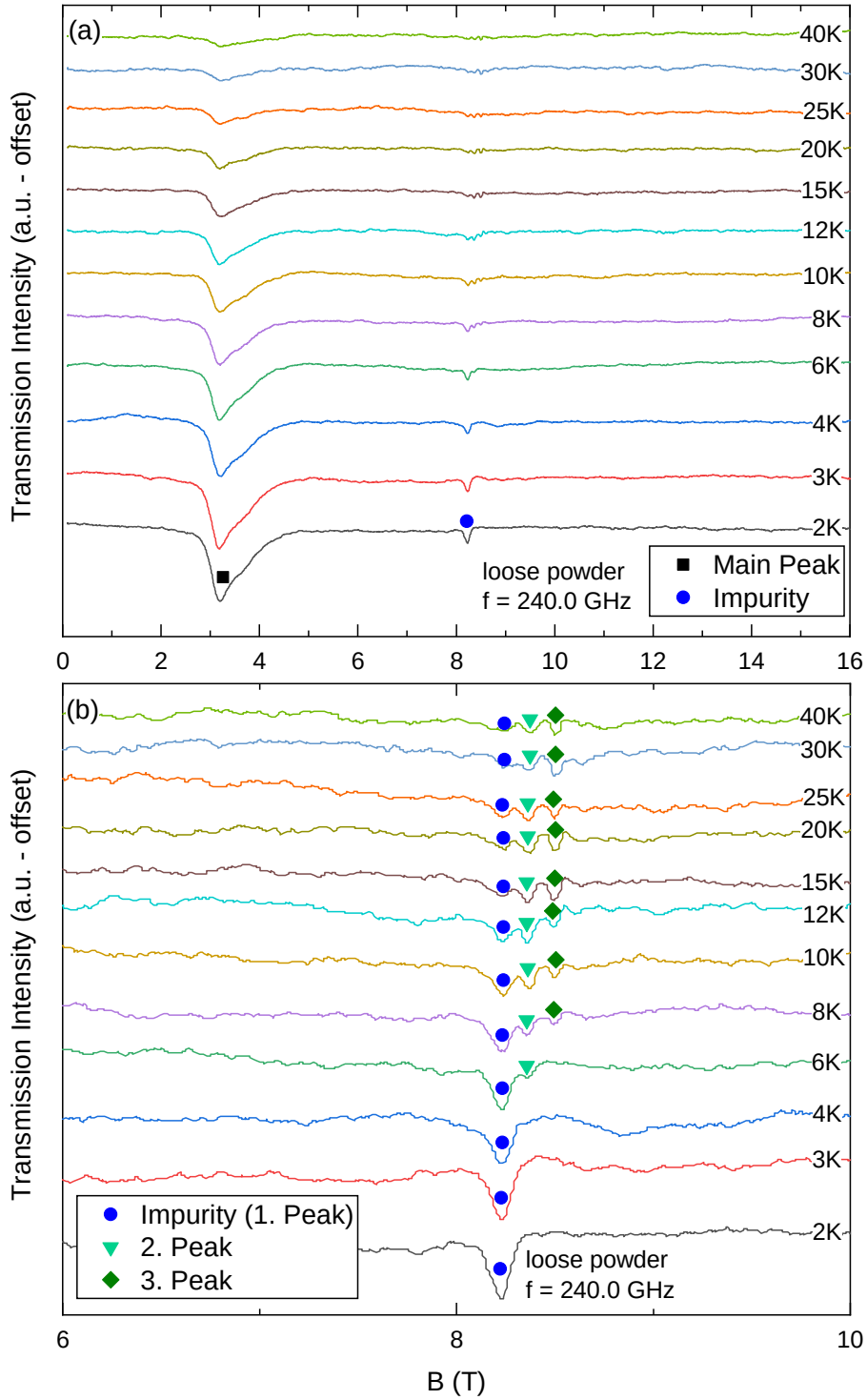


Figure A.1.2: (a) HF-EPR spectra of a loose powder sample of **(1)** measured at 240.0 GHz for temperatures from 2 to 40 K. All spectra are background-corrected and shifted along the ordinate. (b) Zoom of the magnetic field range between 6 and 10 T. With increasing temperature, the intensity of the impurity-related resonance feature decreases. Above 6 K, a second peak appears at slightly higher magnetic fields, and above 8 K, a third peak becomes visible at even higher fields.

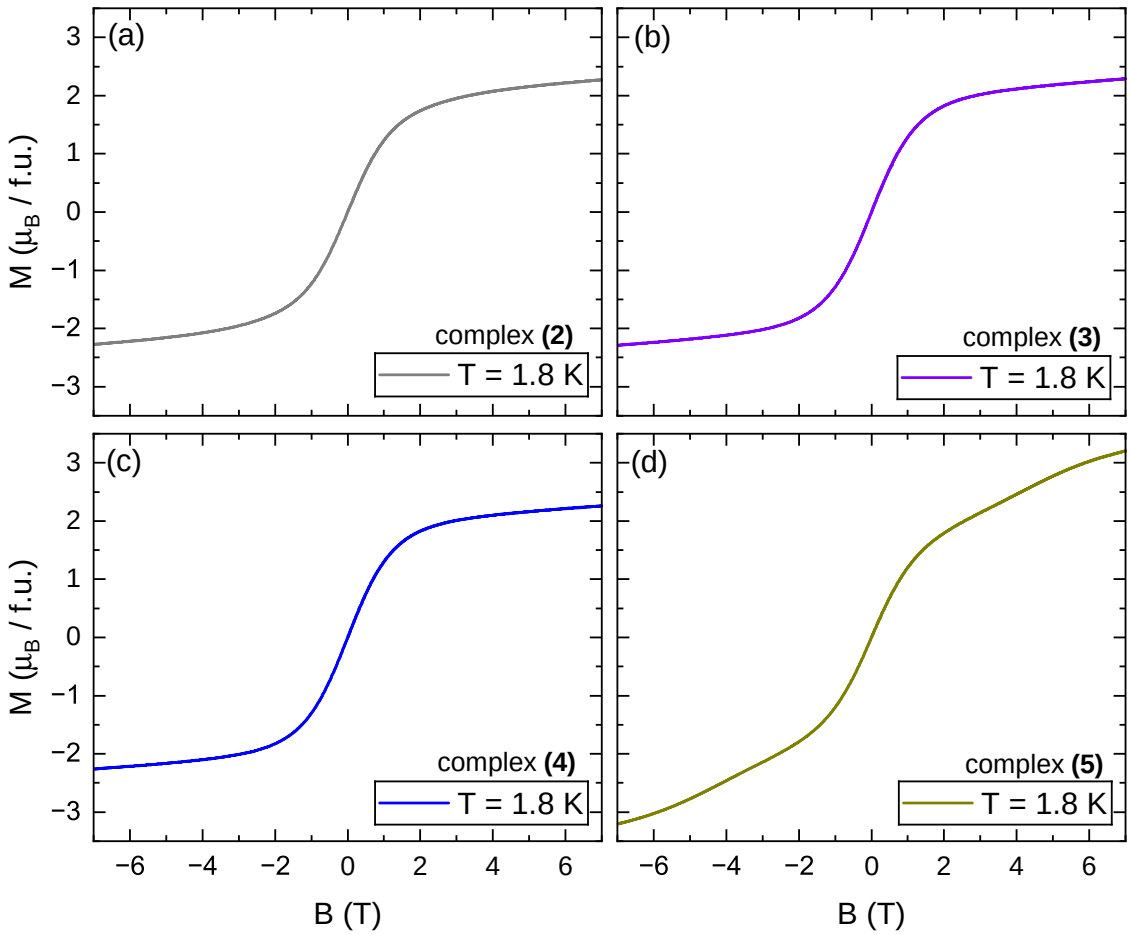


Figure A.1.3: (a) - (d) Full magnetisation loop of **(2)** - **(5)** measured at $T = 1.8$ K. No hysteresis are visible for all complexes.

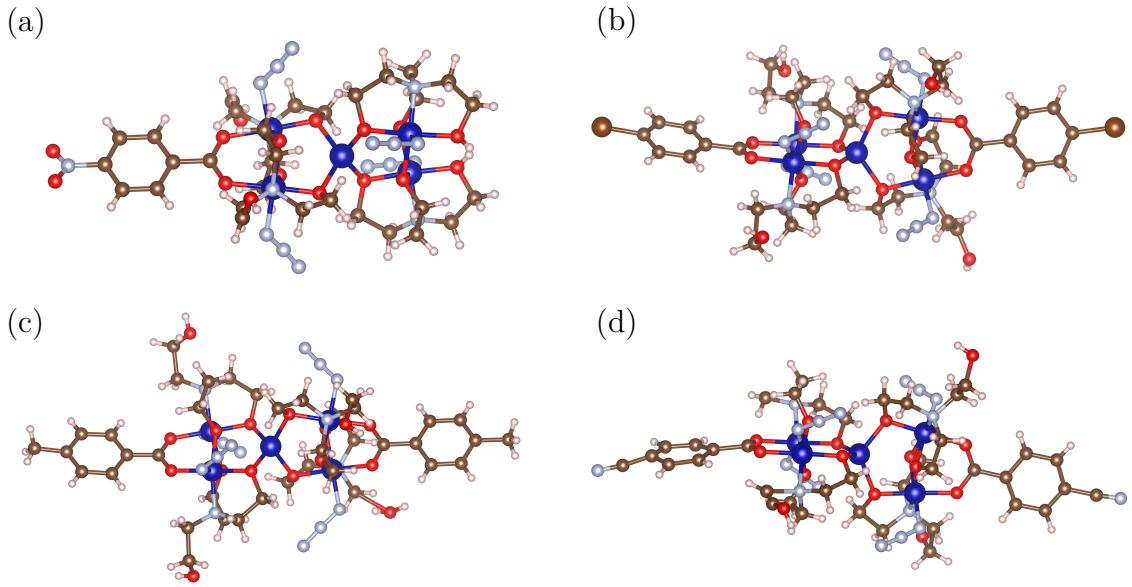


Figure A.1.4: (a) - (d) Molecular Structure of **(2)** - **(5)**. Colours: Co (blue), O (red), N (light blue), C (small brown), H (rosa), Br (large brown) [41]. Images were generated by VESTA [42].

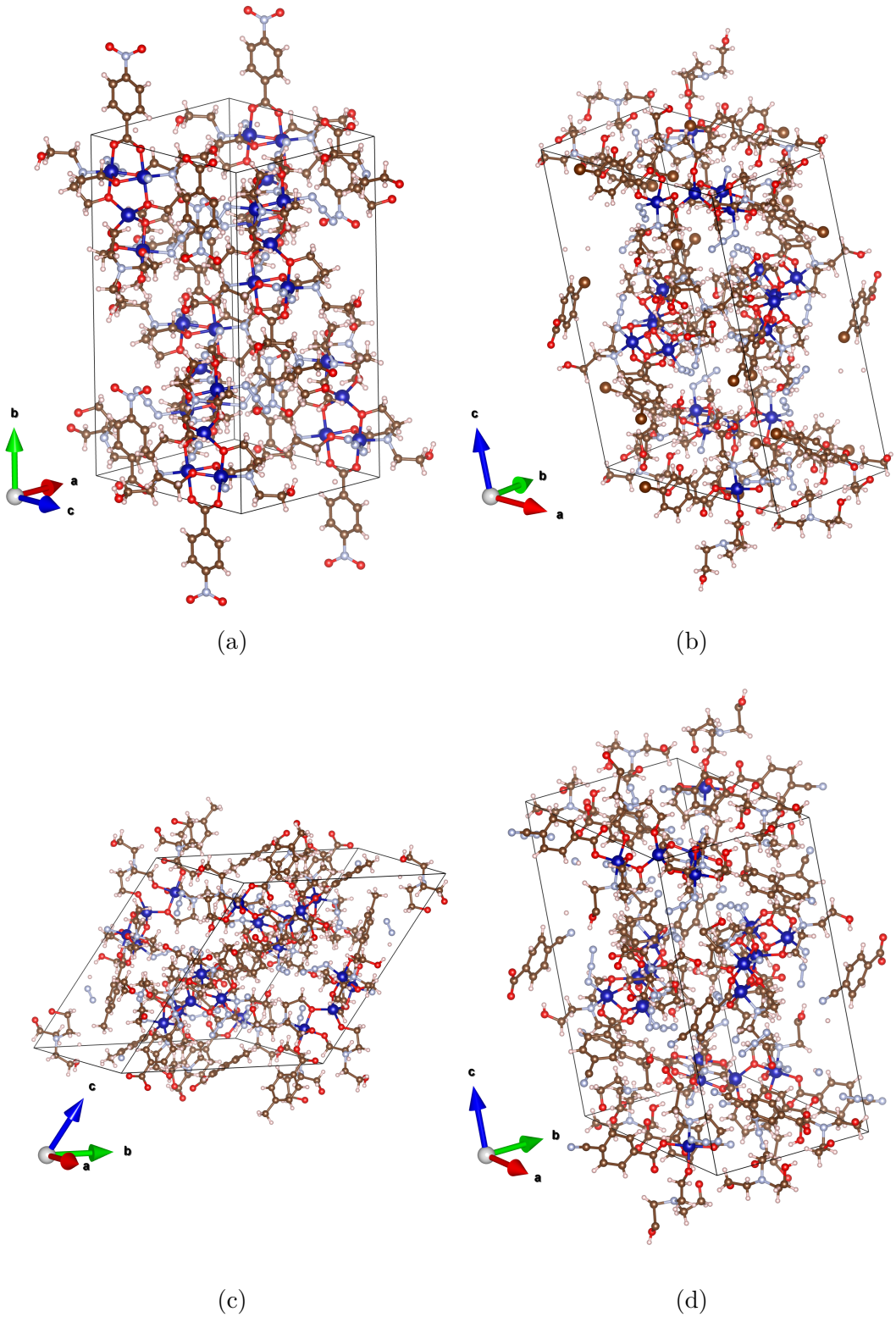


Figure A.1.5: (a) - (d) Crystal packing of **(2)** - **(5)**. Colours: Co (blue), O (red), N (light blue), C (small brown), H (rosa), Br (large brown). Black lines indicate the unit cell [41]. Images were generated by VESTA [42].

A.2 Additional: All-Metal-Aromaticity: Bi_4 Ring

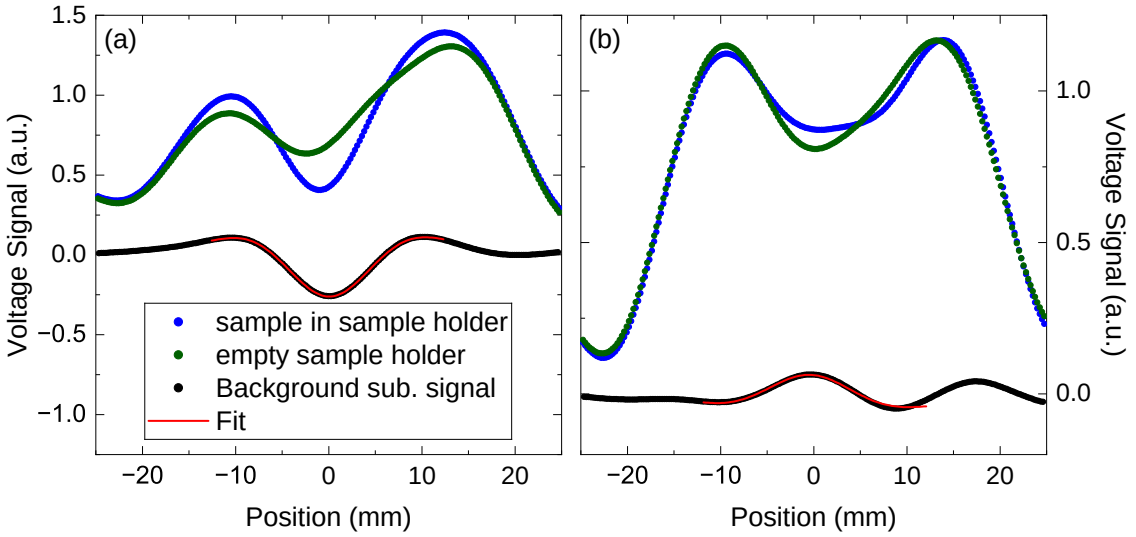


Figure A.2.1: (a) Voltage-position curve of the Bi_4 sample at $B = 1$ T and $T = 300$ K as an example for a good scan. (b) Voltage-position curve of the Li_4 sample at $B = 1$ T and $T = 100$ K as an example for the worst background/sample signal ratio in the temperature range 100 - 300 K. The background-corrected signals in (a) and (b) show a different sign signalling positive magnetisation for Bi_4 and negative magnetisation for Li_4 sample, at the respective temperatures.

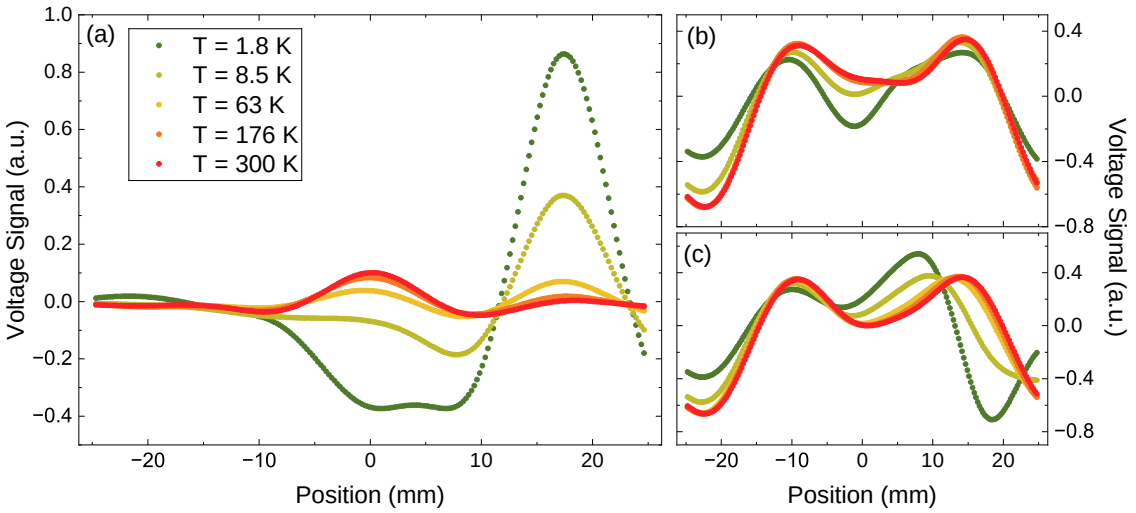
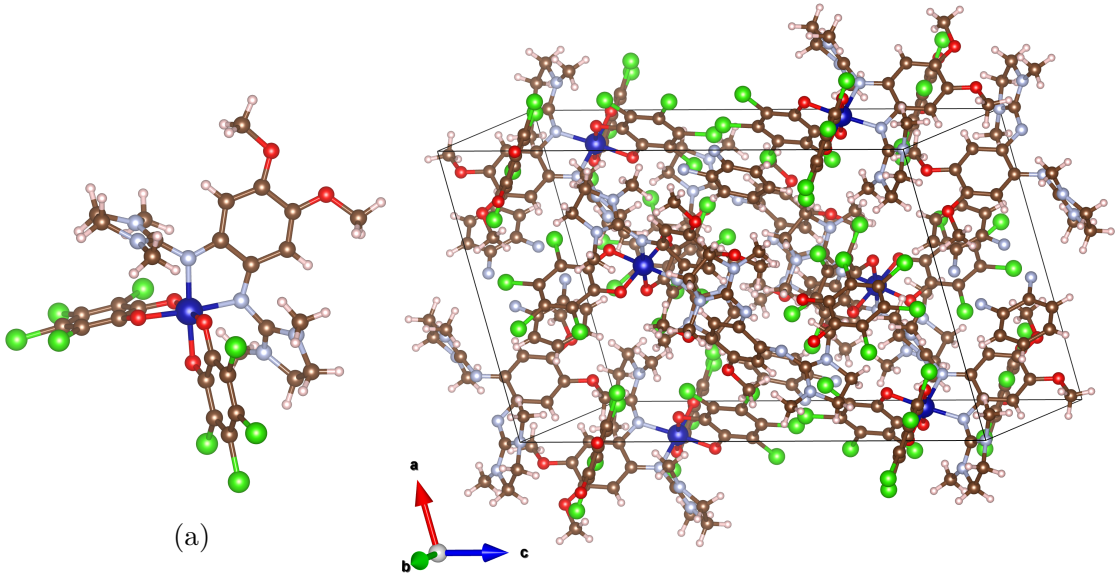


Figure A.2.2: (a) Voltage-position curves of the Li_4 sample at $B = 1$ T for different temperatures. (a) Background subtracted; (b) (raw) sample signal; (c) background scan.

A.3 Investigations of an octahedral Co^{x+} complex

The Co^{x+} complex was synthesised by Hanna Pfisterer (group of Prof. Hans-Jörg Himmel at Heidelberg University). The oxidation state remains ambiguous, as both Co^{3+} with a radical ligand and Co^{2+} are possible. The HF-EPR spectra exhibit a single absorption feature with an effective g-factor of $g_{\text{eff}} \approx 2$ and no observable ZFS (see fig. A.3.2). Additional features are observed within a narrow frequency interval around 67 GHz; the origin of that is discussed in more detail in section 3.2.4. The magnetisation measurements do not follow a purely Brillouin-like behaviour.



(a) (b)

Figure A.3.1: (a) Molecular structure of the Co^{x+} complex. (b) Crystal packing of Co complex. Colours: Co (blue), O (red), N (light blue), C (brown), H (pink), Cl (green). Black lines indicate the unit cell. Data from AG Himmel [68]. The images were generated using VESTA [42].

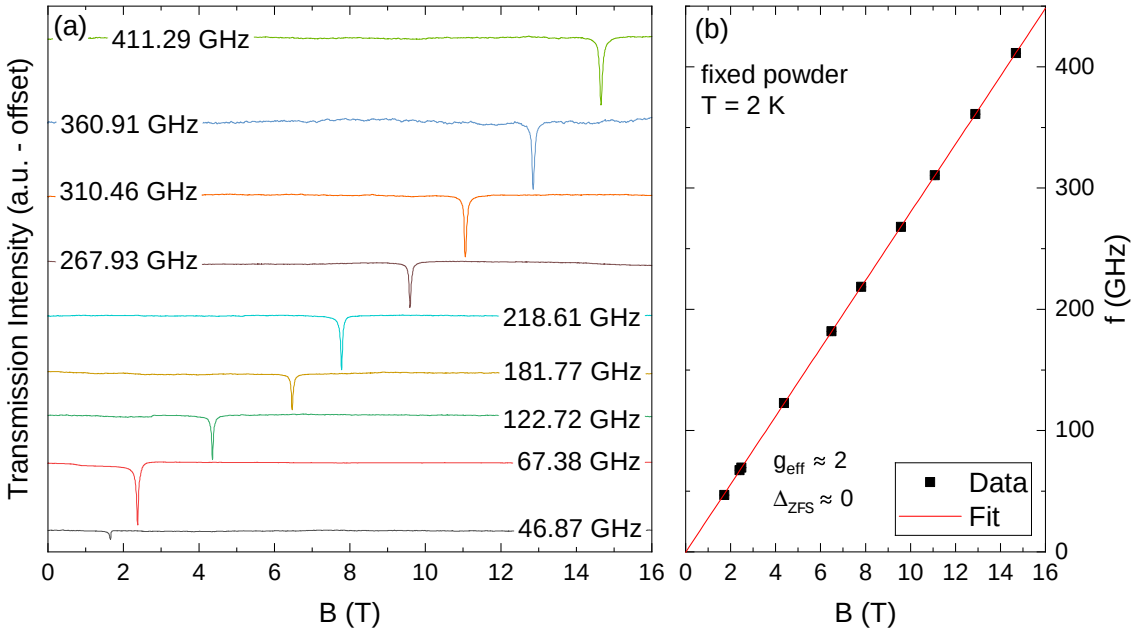


Figure A.3.2: (a) HF-EPR spectra of a fixed powder sample of the Co^{x+} complex measured at 2 K and varying frequencies from 46.9 to 411.3 GHz. All spectra are phase-mixing-corrected, background-corrected and shifted along the ordinate. (b) Frequency-field diagram of the Co complex at 2 K. The resonance positions (black squares) corresponds to the minima in the HF-EPR spectra. The resonances are fit using $hf_{\mathrm{res}} = \Delta_{\mathrm{ZFS}} + g_{\mathrm{eff}} \cdot \mu_{\mathrm{B}} B_{\mathrm{res}}$ (solid line).

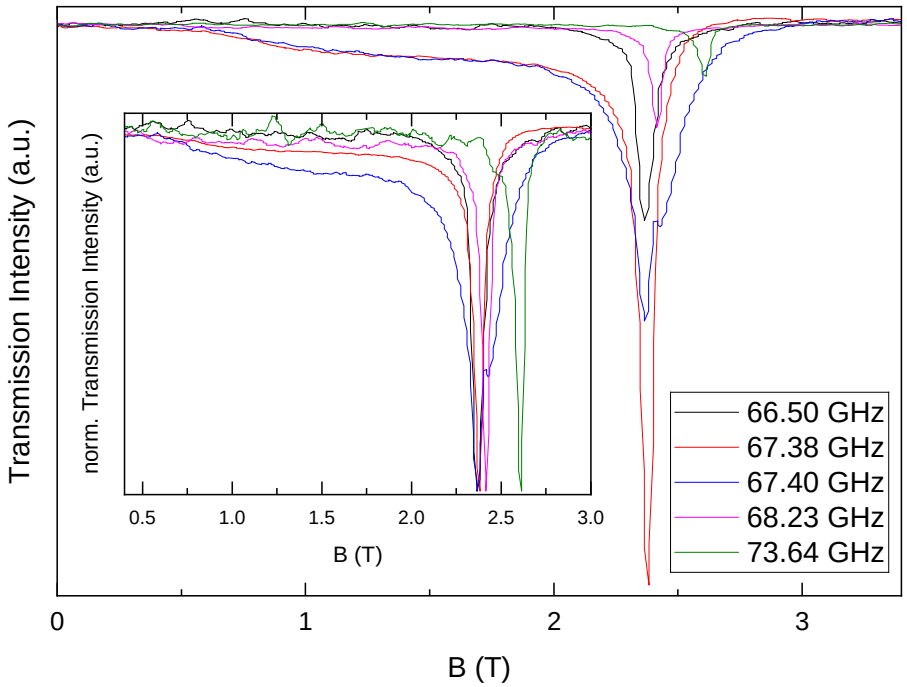


Figure A.3.3: HF-EPR spectra of a fixed powder sample of the Co^{x+} complex measured at 2 K and varying frequencies in a small interval from 66.50 to 73.64 GHz. All spectra are phase-mixing- and background-corrected. Inset: normalised spectra to better resolve the shoulder feature.

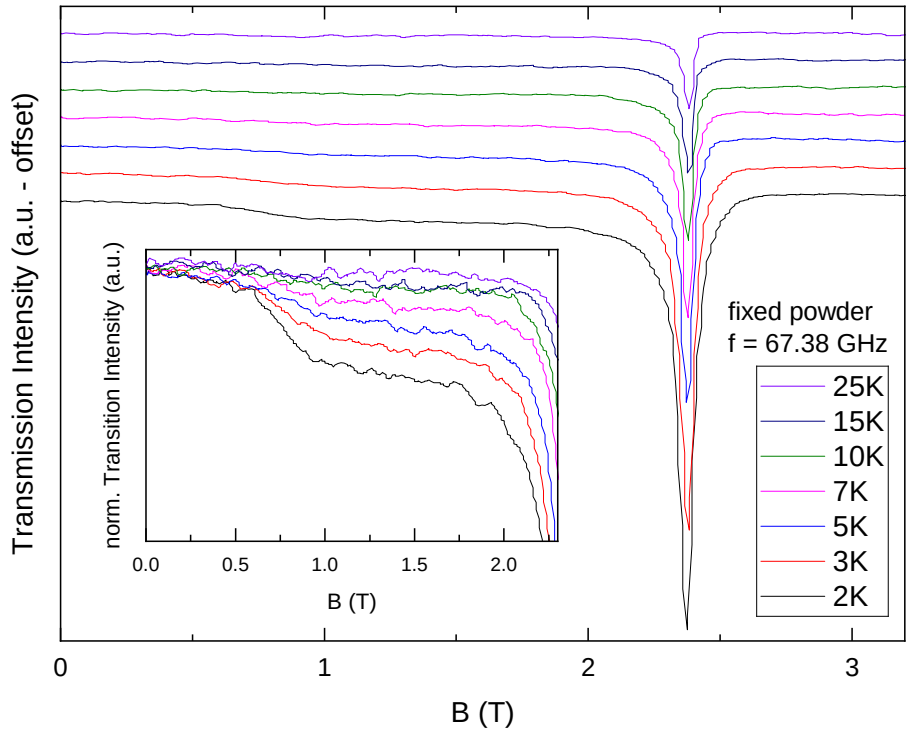


Figure A.3.4: HF-EPR spectra of a fixed powder sample of the Co^{x+} complex measured at $f = 67.38$ GHz for temperatures from 2 to 25 K. All spectra are phase-mixing-corrected, background-corrected, and shifted along the ordinate. Inset: normalised spectra to better resolve the shoulder feature.

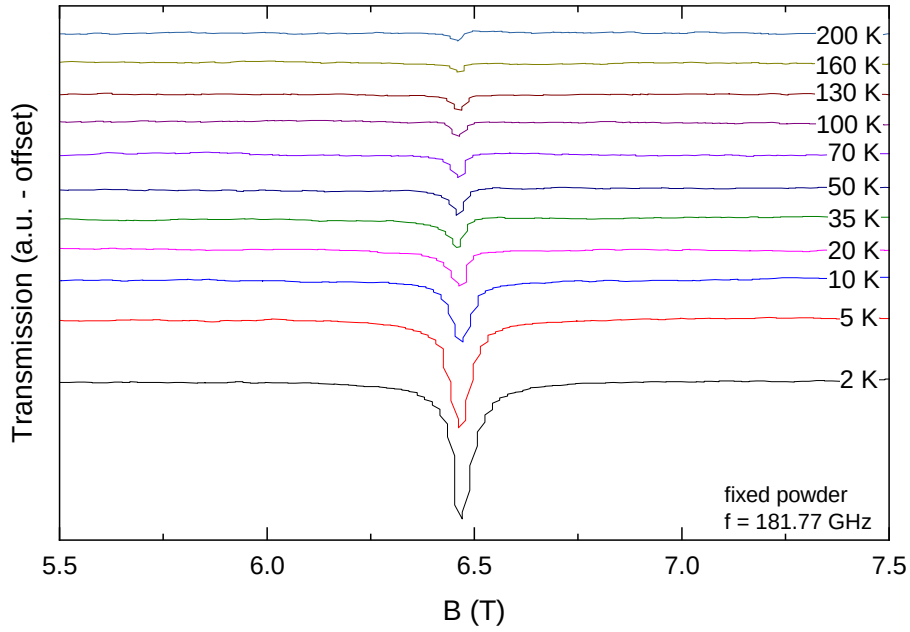


Figure A.3.5: HF-EPR spectra of a fixed powder sample of the Co^{x+} complex measured at $f = 181.77$ GHz for temperatures from 2 to 200 K. All spectra are phase-mixing-corrected, background-corrected, and shifted along the ordinate.

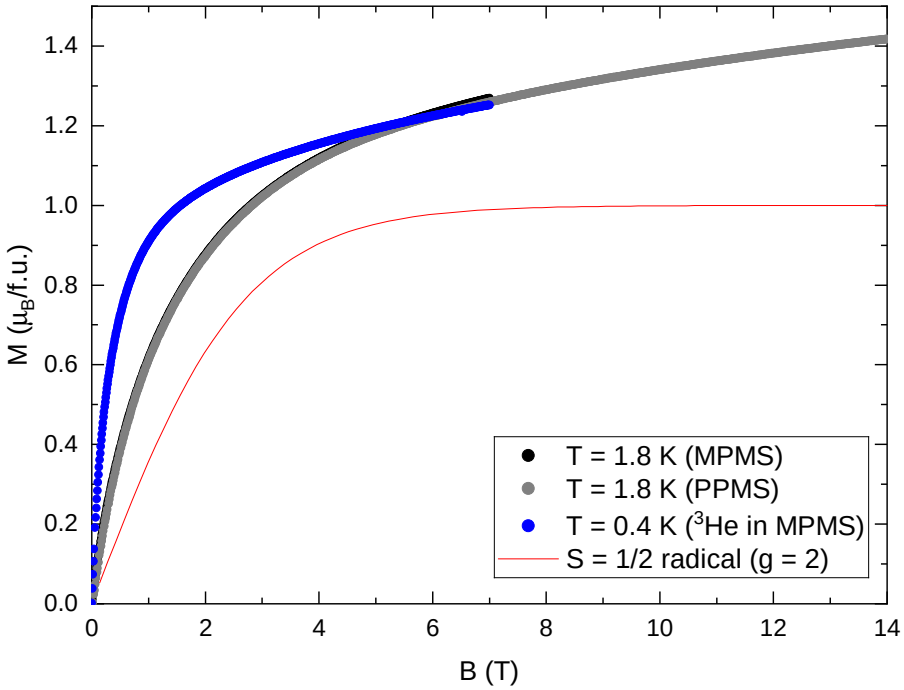


Figure A.3.6: Magnetic field dependence of the DC magnetisation of the Co^{x+} complex measured at two different temperatures. Black dots: at 1.8 K in the MPMS up to 7 T; grey dots: at 1.8 K in the PPMS up to 14 T; blue dots: at 0.4 K in the MPMS up to 7 T using the ^{3}He option (note that this curve is not correctly scaled). The red solid lines represents the magnetisation of an $S = 1/2$ radical with $g = 2$.

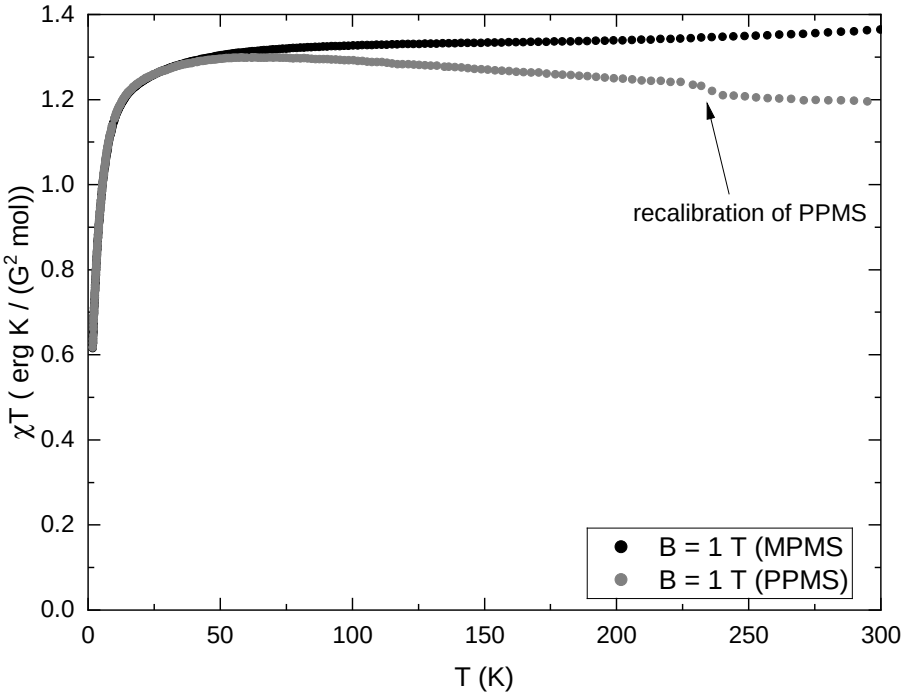


Figure A.3.7: Temperature dependence of the static magnetic susceptibility $\chi = M/B$ of the Co^{x+} complex plotted as χT measured in the MPMS and PPMS.

A.4 Investigations of a Diradical Dimer

In this section, a diradical dimeric is investigated. The compound was synthesised by Pascal Merten (group of Prof. Uwe Bunz at Heidelberg University). Fig. A.4.1 shows the molecular structure of the diradical dimer. The two unpaired electrons (depicted as black dots) interact via the planar anthracene unit [69].

The diradical dimer ($m = 9.22(3)$ mg, $M = 1446.18$ g/mol) was prepared in a capsule and mounted onto a brass sample holder. For background subtraction, the signal of a different capsule was used. Due to the small magnetic moment of the sample and the varying magnetic behaviour of different capsules at low temperatures (see section 3.1.3), the static magnetisation measurement at 1.8 K was useless for the analysis.

Fig. A.4.2 shows the temperature dependence of the static magnetic susceptibility $\chi = M/B$ of the diradical dimer at $B = 1$ T. It exhibits a Curie-like behaviour at low temperatures. Upon heating above approximately 150 K, it slightly increases up to 400 K. This behaviour can be associate with quasi-free magnetic moments $S = 1/2$ accounting for the low-temperature tail and a gapped subsystem, most likely antiferromagnetically coupled $S = 1/2$ dimers.

By assuming isotropic interaction between two radicals, the resulting Hamiltonian for the spin dimer can be written as

$$\hat{\mathcal{H}} = -J\hat{\boldsymbol{S}}_1\hat{\boldsymbol{S}}_2, \tag{A.1}$$

with the coupling constant J. The magnetic susceptibility of such an interacting

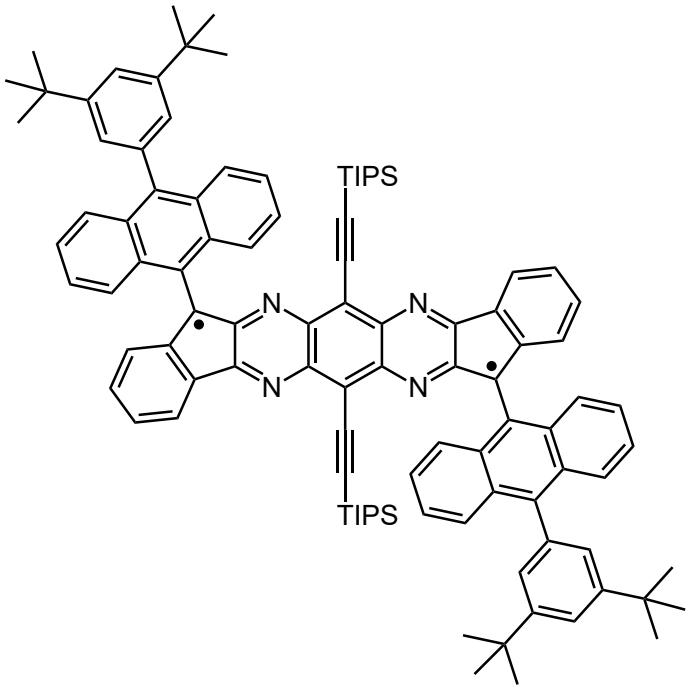


Figure A.4.1: Molecular structure of the diradical dimer. Structure from [69].

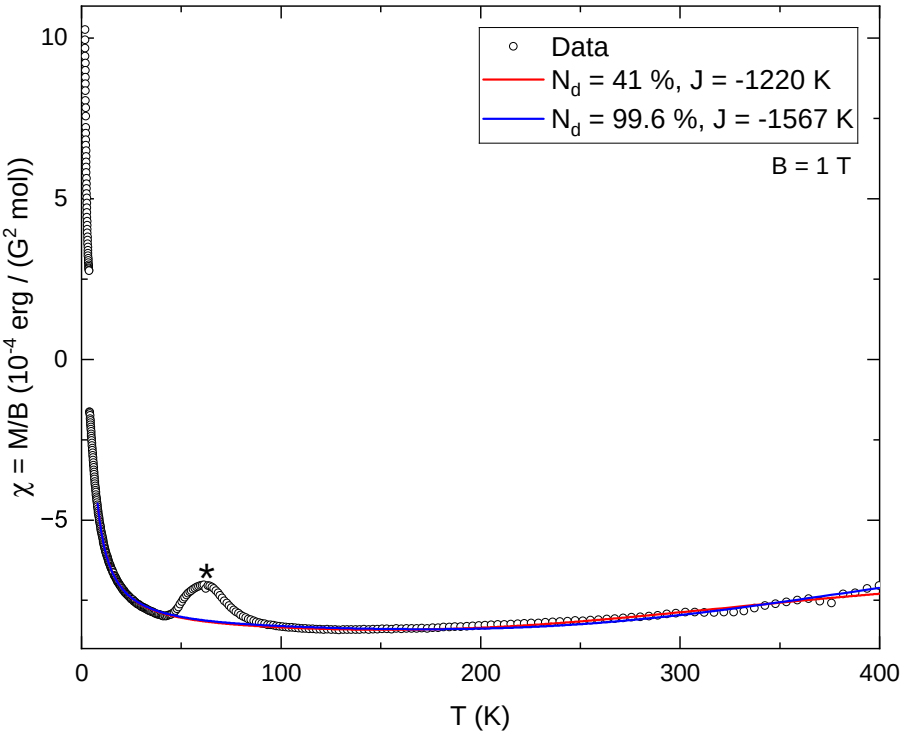


Figure A.4.2: Static magnetic susceptibility of the diradical dimer measured at $B = 1$ T. The anomaly marked by the asterisk originates from the sample holder and is assumed to result from absorbed oxygen in the capsules. The solid lines represent fits to the data using eq. (A.3), as described in the text.

spin dimer ($S_1 = S_2 = 1/2$) is given by the Bleaney-Bowers equation [70]

$$\chi_{\mathrm{dim}} = \frac{n\mu_{\mathrm{B}}^2 g^2}{k_{\mathrm{B}}T} \frac{2}{3 + e^{-\frac{J}{k_{\mathrm{B}}T}}}. \tag{A.2}$$

To account for the quasi-free magnetic moments and the coupled dimers, we hence fit the data using

$$\chi = \chi_0 + N_{\mathrm{m}} \cdot 0.375 \cdot \frac{g^2}{4(T+\theta)} + N_{\mathrm{d}} \cdot \chi_{\mathrm{dim}}, \tag{A.3}$$

with N_{m} being the number of quasi-free moments, N_{d} the number of antiferromagnetic dimers, θ the Weiss temperature, and χ_0 a temperature-independent contribution. The fit was done using $g = 2$, for $T > 8$ K and excluding the region of the oxygen impurity. The fit parameters are presented in tab A.4.1. The best fit to the data yields $N_{\mathrm{d}} = 41$ %, $J = -1220$ K, and $N_{\mathrm{d}} < 1$ %. Due to the limited temperature regime, the number and magnetic coupling of such strongly interacting dimers can only be roughly estimated from the experimental data. More reliable values are hence obtained by assuming that all molecules under study either exhibit a monoradical or a diradical [69], i.e., setting $N_{\mathrm{m}}/2 + N_{\mathrm{d}} = 1$. This addition constraint to the fits

	N_d (%)	N_m (%)	g	J (K)	θ (K)	χ_0 (10^{-4} erg/(G^{2}mol))
Fit 1	41(3)	0.775(11)	2	-1220(25)	-1.05(11)	-8.634(11)
Fit 2	99.635(6)	0.730(11)	2	-1566(7)	-1.40(12)	-8.576(10)

Table A.4.1: Fit parameters obtained from fitting eq. (A.3) to the data $\chi = M/B$. Fit 1 was performed with N_d and N_m as free parameters, while Fit 2 was carried out under the restriction $N_\mathrm{m}/2 + N_\mathrm{d} = 1$. The reported uncertainties correspond to the statistical errors from the fitting procedure and should not be interpreted as the full experimental uncertainties.

yields $N_\mathrm{d} = 99.6$ %, $J = -1566$ K, and $N_\mathrm{d} < 1$ % (see tab A.4.1).

The antiferromagnetic coupling is in agreement with low-temperature NMR studies by Pascal Merten [69].The obtained temperature-independent susceptibility is diamagnetic and agrees to the value expected by estimating χ_0 by means of Pascal's constants [64], i.e., $\chi_0^\mathrm{Pascal} \approx -10 \cdot 10^{-4}$ erg/(G^{2}mol).

Bibliography

[1] J. M. D. Coey. *Magnetism and Magnetic Materials*. Cambridge University Press, 2001.

[2] D. Gatteschi, R. Sessoli, and J. Villain. *Molecular Nanomagnets*. Oxford University Press, Oxford, 2006.

[3] R. Sessoli, D. Gatteschi, A. Caneschi, and M. A. Novak. "Magnetic bistability in a metal-ion cluster". *Nature*, 365(6442): 141–143, 1993.

[4] D. Gatteschi and R. Sessoli. "Quantum Tunneling of Magnetization and Related Phenomena in Molecular Materials". *Angewandte Chemie International Edition*, 42(3): 268–297, 2003.

[5] M. N. Leuenberger and D. Loss. "Quantum computing in molecular magnets". *Nature*, 410(6830): 789–793, 2001.

[6] Y. Wang, W. Li, S. Zhou, D. Kong, H. Yang, and L. Wu. "Mn12 single-molecule magnet aggregates as magnetic resonance imaging contrast agents". *Chemical Communications*, 47(12): 3541, 2011.

[7] B. Cage, S. E. Russek, R. Shoemaker, A. J. Barker, C. Stoldt, V. Ramachandaran, and N. S. Dalal. "The utility of the single-molecule magnet Fe_8 as a magnetic resonance imaging contrast agent over a broad range of concentration". *Polyhedron*, 26(12): 2413–2419, 2007.

[8] A. Abragam and B. Bleaney. *Electron paramagnetic resonance of transition ions*. Oxford University Press, Oxford, 2013.

[9] M. Murugesu, M. Habrych, W. Wernsdorfer, K. A. Abboud, and G. Christou. "Single-Molecule Magnets: A Mn_{25} Complex with a Record S = 51/2 Spin for a Molecular Species". *Journal of the American Chemical Society*, 126(15): 4766–4767, 2004.

[10] T. C. Stamatatos, K. A. Abboud, W. Wernsdorfer, and G. Christou. "'Spin Tweaking' of a High-Spin Molecule: An Mn_{25} Single-Molecule Magnet with an S=61/2 Ground State". *Angewandte Chemie International Edition*, 46(6): 884–888, 2007.

[11] E. Ruiz, J. Cirera, J. Cano, S. Alvarez, C. Loose, and J. Kortus. "Can large magnetic anisotropy and high spin really coexist?" *Chem. Commun.*, (1): 52–54, 2008.

[12] D. N. Woodruff, R. E. P. Winpenny, and R. A. Layfield. "Lanthanide Single-Molecule Magnets". *Chemical Reviews*, 113(7): 5110–5148, 2013.

[13] K. Liu, W. Shi, and P. Cheng. "Toward heterometallic single-molecule magnets: Synthetic strategy, structures and properties of 3d–4f discrete complexes". *Coordination Chemistry Reviews*, 289–290: 74–122, 2015.

[14] D. Maniaki, E. Pilichos, and S. P. Perlepes. “Coordination Clusters of 3d-Metals That Behave as Single-Molecule Magnets (SMMs): Synthetic Routes and Strategies”. *Frontiers in Chemistry*, 6, 2018.

[15] W. Wernsdorfer, N. Aliaga-Alcalde, D. N. Hendrickson, and G. Christou. “Exchange-biased quantum tunnelling in a supramolecular dimer of single-molecule magnets”. *Nature*, 416(6879): 406–409, 2002.

[16] J. D. Rinehart, M. Fang, W. J. Evans, and J. R. Long. “Strong exchange and magnetic blocking in N_2^{3-}-radical-bridged lanthanide complexes”. *Nature Chemistry*, 3(7): 538–542, 2011.

[17] S. Blundell. *Magnetism in Condensed Matter*. Oxford University Press, London, England, 2001.

[18] P. Bertrand. *Electron Paramagnetic Resonance Spectroscopy: Fundamentals*. Springer International Publishing, 2020.

[19] I. V. Hertel and C.-P. Schulz. *Atome, Moleküle und optische Physik 1*. Springer Berlin Heidelberg, 2017.

[20] K. W. H. Stevens. “Matrix Elements and Operator Equivalents Connected with the Magnetic Properties of Rare Earth Ions”. *Proceedings of the Physical Society. Section A*, 65(3): 209–215, 1952.

[21] D. Khomskii. *Transition metal compounds*. Cambridge University Press, Cambridge, 2014.

[22] C. V. Topping and S. J. Blundell. “A.C. susceptibility as a probe of low-frequency magnetic dynamics”. *Journal of Physics: Condensed Matter*, 31(1): 013001, 2018.

[23] H. Casimir and F. du Pré. “Note on the thermodynamic interpretation of paramagnetic relaxation phenomena”. *Physica*, 5(6): 507–511, 1938.

[24] M. Briganti, F. Santanni, L. Tesi, F. Totti, R. Sessoli, and A. Lunghi. “A Complete Ab Initio View of Orbach and Raman Spin–Lattice Relaxation in a Dysprosium Coordination Compound”. *Journal of the American Chemical Society*, 143(34): 13633–13645, 2021.

[25] D. I. Quantum Design. *Magnetic Property Measurement System MPMS3 User’s Manual*. Manual. 2016.

[26] D. I. Quantum Design. *User guide iHelium3 for the MPMS3*. User guide. 2022.

[27] D. I. Quantum Design. *Magnetic Property Measurement System AC Option User’s Manual,* Manual. 1999.

[28] J. Arneth. “Experimental Studies on the Ligand Field Effects and Magnetic Interactions in 3d, 4f and 5d Mono- and Heterometallic Molecular Compounds”. PhD thesis. Heidelberg University, 2025.

[29] M. J. Coak, C. Liu, D. M. Jarvis, S. Park, M. J. Cliffe, and P. A. Goddard. "SquidLab—A user-friendly program for background subtraction and fitting of magnetization data". *Review of Scientific Instruments*, 91(2), 2020.

[30] Jan Arneth, private correspondence.

[31] J. S. McCloy and B. Walsh. "Sublattice Magnetic Relaxation in Rare Earth Iron Garnets". *IEEE Transactions on Magnetics*, 49(7): 4253–4256, 2013.

[32] J. Park. "High-field Electron Spin Resonance study on Correlated Transition Metal Compounds and Metal-Organic Compounds". PhD thesis. Heidelberg University, 2016.

[33] M. Jonák. "Low-Energy Magnetic Excitations and Magnetisation in Magnetoelectric Antiferromagnets MnTiO3 and LiMnPO4 and in van-der-Waals Ferromagnet CrI3". PhD thesis. Heidelberg University, 2022.

[34] G. Feher and A. F. Kip. "Electron Spin Resonance Absorption in Metals. I. Experimental". *Physical Review*, 98(2): 337–348, 1955.

[35] M. Linzer. "Line Parameters of Lorentzian Curves Containing Arbitrary Mixtures of Absorption and Dispersion". *Journal of Applied Physics*, 40(1): 372–376, 1969.

[36] S. Stoll and A. Schweiger. "EasySpin, a comprehensive software package for spectral simulation and analysis in EPR". *Journal of Magnetic Resonance*, 178(1): 42–55, 2006.

[37] E.-C. Yang, D. N. Hendrickson, W. Wernsdorfer, M. Nakano, L. N. Zakharov, R. D. Sommer, A. L. Rheingold, M. Ledezma-Gairaud, and G. Christou. "Cobalt single-molecule magnet". *Journal of Applied Physics*, 91(10): 7382–7384, 2002.

[38] M. Murrie. "Cobalt(ii) single-molecule magnets". *Chemical Society Reviews*, 39(6): 1986, 2010.

[39] J. M. Zadrozny, J. Telser, and J. R. Long. "Slow magnetic relaxation in the tetrahedral cobalt(II) complexes $[Co(EPh)_4]^{2-}$ (EO, S, Se)". *Polyhedron*, 64: 209–217, 2013.

[40] G. Lococciolo, S. K. Gupta, S. Dechert, S. Demeshko, C. Duboc, M. Atanasov, F. Neese, and F. Meyer. "Oxygen-Donor Metalloligands Induce Slow Magnetization Relaxation in Zero Field for a Cobalt(II) Complex with CoO_4 Motif". *Inorganic Chemistry*, 63(12): 5652–5663, 2024.

[41] Amit Gharu, private correspondence.

[42] K. Momma and F. Izumi. "VESTA 3 for three-dimensional visualization of crystal, volumetric and morphology data". *Journal of Applied Crystallography*, 44(6): 1272–1276, 2011.

[43] K. Chattopadhyay, M. J. Heras Ojea, A. Sarkar, M. Murrie, G. Rajaraman, and D. Ray. "Trapping of a Pseudotetrahedral $Co^{II}O_4$ Core in Mixed-Valence Mixed-Geometry [Co_5] Coordination Aggregates: Synthetic Marvel, Structures, and Magnetism". *Inorganic Chemistry*, 57(21): 13176–13187, 2018.

[44] X. Feng, J. Liu, T. D. Harris, S. Hill, and J. R. Long. "Slow Magnetic Relaxation Induced by a Large Transverse Zero-Field Splitting in a $Mn^{II}Re^{IV}(CN)_2$ Single-Chain Magnet". *Journal of the American Chemical Society*, 134(17): 7521–7529, 2012.

[45] J. Vallejo, I. Castro, R. Ruiz-García, J. Cano, M. Julve, F. Lloret, G. De Munno, W. Wernsdorfer, and E. Pardo. "Field-Induced Slow Magnetic Relaxation in a Six-Coordinate Mononuclear Cobalt(II) Complex with a Positive Anisotropy". *Journal of the American Chemical Society*, 134(38): 15704–15707, 2012.

[46] K. Robinson, G. V. Gibbs, and P. H. Ribbe. "Quadratic Elongation: A Quantitative Measure of Distortion in Coordination Polyhedra". *Science*, 172(3983): 567–570, 1971.

[47] S. Vaidya, S. Tewary, S. K. Singh, S. K. Langley, K. S. Murray, Y. Lan, W. Wernsdorfer, G. Rajaraman, and M. Shanmugam. "What Controls the Sign and Magnitude of Magnetic Anisotropy in Tetrahedral Cobalt(II) Single-Ion Magnets?" *Inorganic Chemistry*, 55(19): 9564–9578, 2016.

[48] J. Arneth, C. Pachl, G. Greif, B. G. Beier, P. W. Roesky, K. Fink, and R. Klingeler. "Toward Understanding Prolate 4f Monomers: Numerical Predictions and Experimental Validation of Electronic Properties and Slow Relaxation in a Muffin-Shaped Er^{III} Complex". *Inorganic Chemistry*, 65(7): 3929–3939, 2026.

[49] A. K. Matiukhina, E. N. Zorina-Tikhonova, D. O. Blinou, R. D. Svetogorov, P. N. Vasilyev, N. N. Efimov, M. A. Kiskin, and I. L. Eremenko. "The influence of pseudo-tetrahedral coordination environment of Co^{2+} ion in polymeric dimethylmalonates on the magnetic anisotropy and slow magnetic relaxation". *Journal of Magnetism and Magnetic Materials*, 614: 172650, 2025.

[50] P. Happ, C. Plenk, and E. Rentschler. "12-MC-4 metallacrowns as versatile tools for SMM research". *Coordination Chemistry Reviews*, 289–290: 238–260, 2015.

[51] C. M. Zaleski, E. C. Depperman, J. W. Kampf, M. L. Kirk, and V. L. Pecoraro. "Using Ln^{III}[15-$MC_{Cu^{II}(N)(S)\text{-pheHA}}$-5]$^{3+}$ Complexes To Construct Chiral Single-Molecule Magnets and Chains of Single-Molecule Magnets". *Inorganic Chemistry*, 45(25): 10022–10024, 2006.

[52] A. J. Stemmler, J. W. Kampf, M. L. Kirk, B. H. Atasi, and V. L. Pecoraro. "The Preparation, Characterization, and Magnetism of Copper 15-Metallacrown-5 Lanthanide Complexes". *Inorganic Chemistry*, 38(12): 2807–2817, 1999.

[53] Alexander Hagenow, private correspondence.

[54] N. Ahmed, T. Sharma, L. Spillecke, C. Koo, K. U. Ansari, S. Tripathi, A. Caneschi, R. Klingeler, G. Rajaraman, and M. Shanmugam. “Probing the Origin of Ferro-/Antiferromagnetic Exchange Interactions in Cu(II)–4f Complexes”. *Inorganic Chemistry*, 61(14): 5572–5587, 2022.

[55] J. Arneth, X.-F. Li, J. Braun, S. Paul, M. Schulze, C. E. Anson, W. Wernsdorfer, A. K. Powell, and R. Klingeler. “The Interplay of Single Ion Anisotropy and Magnetic 3d-4f Interactions in $V_2^{III}Ln_2^{III}$ Butterfly Complexes”. *ChemistryEurope*, 3(3), 2025.

[56] J. Wang, Q.-W. Li, S.-G. Wu, Y.-C. Chen, R.-C. Wan, G.-Z. Huang, Y. Liu, J.-L. Liu, D. Reta, M. J. Giansiracusa, Z.-X. Wang, N. F. Chilton, and M.-L. Tong. “Opening Magnetic Hysteresis by Axial Ferromagnetic Coupling: From Mono-Decker to Double-Decker Metallacrown”. *Angewandte Chemie*, 133(10): 5359–5366, 2021.

[57] C. Koo, J. Park, J. Butscher, E. Rentschler, and R. Klingeler. “High-frequency EPR study on Cu_4Cu- and Co_4Co-metallacrown complexes”. *Journal of Magnetism and Magnetic Materials*, 477: 340–343, 2019.

[58] A. V. Pavlishchuk, S. V. Kolotilov, M. Zeller, S. E. Lofland, L. K. Thompson, A. W. Addison, and A. D. Hunter. “High Nuclearity Assemblies and One-Dimensional (1D) Coordination Polymers Based on Lanthanide–Copper 15-Metallacrown-5 Complexes (Ln^{III} = Pr, Nd, Sm, Eu)”. *Inorganic Chemistry*, 56(21): 13152–13165, 2017.

[59] A. V. Pavlishchuk, S. V. Kolotilov, M. Zeller, L. K. Thompson, and A. W. Addison. “Formation of Coordination Polymers or Discrete Adducts via Reactions of Gadolinium(III)–Copper(II) 15-Metallacrown-5 Complexes with Polycarboxylates: Synthesis, Structures and Magnetic Properties”. *Inorganic Chemistry*, 53(3): 1320–1330, 2014.

[60] A. V. Pavlishchuk, M. Zeller, L. M. Carrella, E. Rentschler, J. K. Bindra, N. Dalal, J. Kinyon, K. Perera, V. V. Pavlishchuk, and A. W. Addison. “Structural and Magnetic Properties of a $(GdCu_5)_2$ Metallacrown Dimer with a Disulfonate Linker”. *European Journal of Inorganic Chemistry*, 27(5), 2024.

[61] M. Andruh, I. Ramade, E. Codjovi, O. Guillou, O. Kahn, and J. C. Trombe. “Crystal structure and magnetic properties of [Ln2Cu4] hexanuclear clusters (where Ln = trivalent lanthanide). Mechanism of the gadolinium(III)-copper(II) magnetic interaction”. *Journal of the American Chemical Society*, 115(5): 1822–1829, 1993.

[62] R. Gershoni-Poranne and A. Stanger. “Magnetic criteria of aromaticity”. *Chem. Soc. Rev.*, 44(18): 6597–6615, 2015.

[63] H. J. Dauben, J. D. Wilson, and J. L. Laity. “Diamagnetic susceptibility exaltation as a criterion of aromaticity”. *Journal of the American Chemical Society*, 90(3): 811–813, 1968.

[64] G. A. Bain and J. F. Berry. “Diamagnetic Corrections and Pascal’s Constants”. *Journal of Chemical Education*, 85(4): 532, 2008.

[65] R. Yadav, A. Maiti, M. Schorpp, J. Graf, F. Weigend, and L. Greb. “Supramolecular trapping of a cationic all-metal σ-aromatic Bi_4 ring”. *Nature Chemistry*, 16(9): 1523–1530, 2024.

[66] Avijit Maiti, private correspondence.

[67] R. M. Bozorth. *Ferromagnetism*. IEEE Press, John Wiley& Sons, Inc., Piscataway, New Jersey, 2015.

[68] Hanna Pfisterer, private correspondence.

[69] Pascal Merten, private correspondence.

[70] B. Bleaney and K. D. Bowers. “Anomalous paramagnetism of copper acetate”. *Proceedings of the Royal Society of London. Series A. Mathematical and Physical Sciences*, 214(1119): 451–465, 1952.

Acknowledgements

I would like to thank Prof. Dr. Rüdiger Klingeler for his supervision and continuous support throughout this work. I am grateful that he created an environment where I could work independently while always having access to support when needed.

I am grateful to Prof. Dr. Maurits Haverkort for serving as the second examiner of this thesis.

A special thanks goes to Jan Arneth for his close supervision. I am very grateful for our many discussions, your helpful suggestions, and for answering my countless questions. I appreciate your support and your constant availability.

I would like to thank all members of the group of Prof. Dr. Rüdiger Klingeler for the friendly and motivating working atmosphere. The daily interactions, as well as the many enjoyable cake breaks, made the time in the group especially enjoyable.

In particular, I would like to thank Luca Bischof and Birte Beier for their support during the experiments. I really appreciate your help and advice, and I am grateful that you are always listen to me.

I am also very grateful to my office mates. I wish Leon all the best for his PhD in Dresden, and I thank Rui for the great company and support during this time, which I hope will continue in the future.

Finally, I would like to thank my friends and family: Thank you for always supporting me and believing in me.

Erklärung

Ich versichere, dass ich diese Arbeit selbstständig verfasst und keine anderen als die angegebenen Quellen und Hilfsmittel benutzt habe.

Heidelberg, den 16.04.2026

Matthias Heinrich